Search for Charged Higgs Bosons in the Topology $\mathrm{t\bar{t}} \rightarrow \mathrm{bH^{+}bW^{-}} \rightarrow \mathrm{b}\tau\nu\mathrm{bqq}$ based on Data taken by the ATLAS Detector in 2010

Diplomarbeit
Physikalisches Institut
Fakultät für Mathematik und Physik
Albert-Ludwigs-Universität Freiburg

vorgelegt von
Anna Kopp

August 2011

Contents

1 Introduction

Within the Standard Model of particle physics, developed in the second half of the 20^{th} century, interactions between elementary particles are described well, using the concept of local gauge theories. However, intrinsically these gauge theories do not yield any particles with masses and can thus not explain massive elementary particles observed in nature. This problem can be solved with the Higgs mechanism, explaining the origin of the masses of particles, but also predicting one more particle belonging to the elementary particles of the Standard Model, a Higgs boson. Although searches have been conducted for some decades now at several particle accelerators, neither any experimental evidence for the existence of the Higgs boson has been found, nor could any other theory explaining the masses of elementary particles be established.

But besides the missing Higgs boson, several other problems remain that the Standard Model cannot solve, such as the hierarchy problem, the existence of Dark Matter or the unification of forces. To find explanations for these, numerous theories evolved in the last decades, building on and extending the Standard Model.

With the Large Hadron Collider at CERN, the highest energetic particle accelerator has taken up work in 2009 and the search for a Higgs boson has been taken to a new step. But besides the Standard Model Higgs boson, lots of other new particles are looked for as well. If any particle not fitting into the framework of the Standard Model will be detected at the LHC, it is clearly a sign for New Physics beyond the Standard Model.

Supersymmetric theories can solve some of the problems the Standard Model cannot. The number of elementary particles in supersymmetric theories is extended to about twice as much as those known. They also bring along at least five Higgs bosons, two of which are charged. Thus if a charged Higgs boson is discovered, this is a definite proof for as of yet unknown physics.

To find evidence for New Physics or to exclude it, it is important to understand the Standard Model background processes very well. In this thesis, background studies and searches for charged Higgs bosons are performed, using $35.5\,\text{pb}^{-1}$ of data taken by ATLAS in 2010.

Light charged Higgs bosons, i.e. with masses less than that of the top quark, are investigated. They are expected to decay to a τ lepton and a neutrino for large fractions of the parameter space, hence here it is assumed that they decay in this channel only. With the charged Higgs boson coming from a top quark pair decay, the signature of the signal process includes a τ lepton, missing transverse energy because of the neutrino which passes the detector without leaving a trace, and at least four jets, accounting for a W boson decaying hadronically and two b quarks resulting from the top quark decays. The signal selection for this channel has been optimized and is presented in detail. Estimating the Standard Model background in a data-driven way, it can be split up into different contributions: electrons, muons or jets faking τ leptons, QCD multi-jet events and events containing true τ leptons.

Processes including true τ leptons are investigated using a so-called embedding technique. The selection for events entering the embedding is optimized and results are compared to simulation and collision data. Systematic uncertainties due to the embedding are studied. Other background contributions have been investigated by other ATLAS members and are quoted here for completeness. Results from these data-driven estimates are compared to collision data. Subsequently, a limit on the production of charged Higgs bosons in top quark decays is derived.

This thesis is structured as follows:
First, an overview on the Standard Model is given, including the Higgs mechanism. Problems of the Standard Model are addressed and the minimal supersymmetric extension is discussed briefly. In the following chapter, the ATLAS detector at LHC is described. The signal process and important backgrounds are presented in chapter 4. The object reconstruction algorithms and identification criteria used are summarized in chapter 5. The following chapters present the main analysis: In chapter 6, the signal selection is described. The optimization of the signal selection in the channel investigated is shown. Background processes including true τ leptons have been studied thoroughly. The method employed for this, comparisons of simulation and collision data and final results are presented in chapter 7. Finally, an upper limit on the branching ratio $t \rightarrow H^+b$ for the signal channel is extracted in chapter 8. A summary of the results obtained is given in chapter 9.

2 Theory

2.1 Introduction

Over the last fifty years quantum field theories evolved, describing all interactions but gravity. The combined theories describing electromagnetic, weak and strong interactions are called the Standard Model of particle physics. The electroweak theory developed by Glashow, Salam and Weinberg [4] describes electromagnetic and weak interactions while quantum chromodynamics (QCD) [5] describes strong interactions. In the Standard Model, all matter consists of quarks and leptons, which are fermions with spin $s = 1/2$. Forces between them are mediated by gauge bosons with spin $s = 1$. Quarks and leptons appear in three generations, summarized in Table 2.1. While leptons carry integer electric charge, ± 1 in the case of electrons, muons and τ leptons and 0 in the case of neutrinos, quarks carry fractions of electric charge. Up-type quarks carry $q = 2/3$ and down-type quarks $q = -1/3$. For every particle shown in Table 2.1 an antiparticle exists with exactly opposite quantum numbers.

Ordinary matter consists of u- and d-quarks and electrons only. Quarks and leptons are assumed to be truly elementary particles, since so far no constituents have been found. Electromagnetic processes are mediated by photons. There are three bosons for weak interactions, Z bosons if the process is electrically neutral and W^+ and W^- bosons for electrically charged processes. Photons, W and Z bosons result from a combined $U(1)_Y \times SU(2)_{I_W}$[1] symmetry, that is broken to $U(1)_q$[2]. Finally, eight gluons are the carriers of the strong force, emerging from the requirement of a local $SU(3)_C$[3] symmetry.

	1st generation	2nd generation	3rd generation
Quarks	**u**p **d**own	**c**harm **s**trange	**t**op **b**ottom
Leptons	electron (**e**) e neutrino $\nu_{\mathbf{e}}$	muon (μ) μ neutrino ν_μ	tau lepton (τ) τ neutrino ν_τ

Table 2.1: Overview of the three generations of matter.

The following introduction can only give a brief overview and is based on [1, 2, 3].

---

[1] Y is for hypercharge and I_W represents the weak isospin, the conserved charge of weak interactions

[2] q represents the electric charge

[3] C is for color, the conserved charge of strong interactions

2.2 Interactions in the Standard Model

Weak interactions can be split into neutral and charged current processes. The gauge bosons $W^{\pm}$ and Z are massive, with $m_{W^{\pm}} = 80.4\,\mathrm{GeV}$ and $m_Z = 90.2\,\mathrm{GeV}$[4].

For leptons, the W bosons only couple to fermions of the same generation. In the case of quarks, intergenerational mixing occurs.

Charged weak interactions can be described by a (V-A) theory, meaning that the coupling of the W bosons to quarks and leptons involves a term combining axial and vector type coupling. This leads to parity violation and because vector and axial vector components of the coupling are of equal strength, the violation is maximal.

In contrast to charged weak currents, no flavor changing neutral currents at tree level have ever been observed. That is, the Z boson couples only to leptons and quarks of the same kind and generation. Unlike the coupling in charged weak interactions, axial and vector components are not of the same strength for the coupling of Z bosons. They depend on the electric charge and hypercharge or weak isospin of the particles.

Electromagnetic and weak interactions can be combined and described by one theory, usually referred to as ’electroweak unification’. Since two gauge groups with two coupling strengths remain, however, it would be more appropriate and less misleading to call it ’electroweak combination.’

Charged weak currents only couple to left chiral fermions, but left and right chiral fermions participate equally in electromagnetic interactions. Thus fermions of different chirality are arranged in singulets and doublets, shown in Table 2.2. Also shown in this table are charge q, weak hypercharge Y and the third component of the weak isospin I_W^3. The following relation holds for charge, hypercharge and weak isospin:

$$q = \frac{Y}{2} + I_W^3 \tag{2.1}$$

Quantum chromodynamics (QCD) describes interactions between quarks mediated by massless gluons. Quarks appear in three different color states: red, green and blue, or the corresponding anticolor for antiquarks. Gluons carry combinations of color and anticolor. The strong force becomes weak at very short distances, leading to so-called asymptotic freedom. In the opposite direction, this implies that the force becomes stronger as distances increase, which causes confinement. Quarks never occur as free particles. They appear in colorless combinations only: in mesons, quark-antiquark-combinations carrying color and anticolor and baryons, three-(anti)quark and (anti)color combinations.

The color/anticolor combinations of gluons can be written as a color octet. Due to confinement, free particles have to be color neutral and thus gluons of the octet do not occur as free particles.

---

[4] Here and whenever else units appear, $c = \hbar = 1$ such that all units can be expressed in eV or eV^{-1}

Quarks						
	generations			q	Y	I_W^3
singulets	$\mathrm{u_r}$	$\mathrm{c_r}$	$\mathrm{t_r}$	2/3	4/3	0
	$\mathrm{d_r}$	$\mathrm{s_r}$	$\mathrm{b_r}$	-1/3	-2/3	0
doublets	$\begin{pmatrix} \mathrm{u} \\ \mathrm{d} \end{pmatrix}_\mathrm{l}$	$\begin{pmatrix} \mathrm{c} \\ \mathrm{s} \end{pmatrix}_\mathrm{l}$	$\begin{pmatrix} \mathrm{t} \\ \mathrm{b} \end{pmatrix}_\mathrm{l}$	2/3 -1/3	1/3 1/3	1/2 -1/2

Leptons						
	generations			q	Y	I_W^3
singulets	-	-	-	-	-	-
	$\mathrm{e_r}$	μ_r	τ_r	-1	-2	0
doublets	$\begin{pmatrix} \nu_e \\ \mathrm{e} \end{pmatrix}_\mathrm{l}$	$\begin{pmatrix} \nu_\mu \\ \mu \end{pmatrix}_\mathrm{l}$	$\begin{pmatrix} \nu_\tau \\ \tau \end{pmatrix}_\mathrm{l}$	0 -1	-1 -1	1/2 -1/2

Table 2.2: Arrangement of fermions into doublets and singulets. Electroweak quantum numbers are shown as well.

2.3 Gauge invariance

All elementary particle interactions in the Standard Model can be described by local gauge theories. That is, the Lagrangian density $\mathscr{L}$ is invariant under global and local gauge transformations, implying conservation of physical quantities. As an example for a fermion field one can use the Dirac Lagrangian for a free particle.

$$\mathscr{L} = i\bar{\psi}\gamma_\mu\partial^\mu\psi - m\bar{\psi}\psi \tag{2.2}$$

It is invariant under global $U(1)$ gauge transformations

$$\psi \rightarrow e^{-i\alpha}\psi \tag{2.3}$$

but not under local ones

$$\psi \rightarrow e^{-i\alpha(x)}\psi \tag{2.4}$$

From the derivative $\partial_\mu\psi$, a new term enters the Lagrangian, breaking the gauge invariance.

$$\partial_\mu\psi \rightarrow e^{i\alpha(x)}\partial_\mu\psi + ie^{i\alpha(x)}\psi\partial_\mu\alpha \tag{2.5}$$

To keep local gauge invariance, the derivatives have to be replaced by covariant derivatives $\partial_\mu \rightarrow D_\mu = \partial_\mu + ieA_\mu$, making it necessary to introduce a new vector field A_μ that couples to the Dirac particle (charge -e) and transforms like

$$A_\mu \rightarrow A_\mu + 1/e \cdot \partial_\mu\alpha \tag{2.6}$$

The vector field A_μ can be regarded as the photon field if a term corresponding to the kinetic energy is added to the Lagrangian.

$$\mathscr{L} = \bar{\psi}(i\gamma^\mu\partial_\mu - m)\psi + e\bar{\psi}\gamma^\mu A_\mu\psi - 1/4F_{\mu\nu}F^{\mu\nu} \tag{2.7}$$

where $F_{\mu\nu} = \partial_\mu A_\nu - \partial_\nu A_\mu$.

In electroweak interactions, the Lagrangian is given by

$$\begin{aligned}\mathscr{L}_{EW} = \quad & \underbrace{-\frac{1}{4}W_{\mu\nu}\cdot W^{\mu\nu} - \frac{1}{4}B_{\mu\nu}B^{\mu\nu}}_{\gamma\text{ ,W}^{\pm}\text{, Z kinetic energies and self interactions}} \\ & \underbrace{+\bar{L}\gamma^\mu\left(i\partial_\mu - g\frac{1}{2}\tau W_\mu - g'\frac{Y}{2}B_\mu\right)L + \bar{R}\gamma^\mu\left(i\partial_\mu - g'\frac{Y}{2}B_\mu\right)R}_{\text{quark and lepton kinetic energies and their interactions with }\gamma\text{, W}^{\pm}\text{, Z}}\end{aligned} \tag{2.8}$$

where τ stands for isospin and Y for hypercharge. Applied to electroweak interactions, the gauge transformations for left- (right)-chiral components are

$$\begin{aligned}\chi_l &\rightarrow \chi_l' = e^{i\alpha(x)\cdot T + i\beta(x)Y}\chi_l \\ \psi_r &\rightarrow \psi_r' = e^{i\beta(x)Y}\psi_r\end{aligned} \tag{2.9}$$

Here, T and Y are the generators of the $SU(2)$ and $U(1)$ groups, the χ_l are the lepton doublets and ψ_r the lepton singulets.

In this Lagrangian 2.7, adding a mass term $1/2\cdot m^2A_\mu A^\mu$ for the photon is prohibited due to the local gauge invariance. This works well for QED, as the photos is massless.

However, for weak interactions this principle seems to be violated. Since the W and Z bosons are clearly massive, an additional field in the Lagrangian has to be assumed giving masses to the W and Z bosons, the electron, muon, τ and quarks while rendering the photon massless. Introducing an ad hoc mass term into the Lagrangian density of weak interactions destroys the gauge invariance and hence renormalizability. Without renormalizability, no precision prediction of e.g. cross sections is possible. In order to incorporate masses of the W and Z bosons into the Standard Model while retaining the gauge symmetry, the Higgs mechanism[5][6] was developed. The $SU(2)_{I_W}\times U(1)_Y$ of electroweak interactions will consequently be broken to $U(1)_Q$.

2.4 Mass generation and Higgs mechanism

If one starts with the Lagrangian

$$\mathscr{L} = \frac{1}{2}(\partial_\mu\phi)(\partial^\mu\phi) + \frac{1}{2}\mu^2\phi^2 - \frac{1}{4}\lambda^2\phi^4 \tag{2.10}$$

---

[5] or Englert-Brout-Higgs-Guralnik-Hagen-Kibble mechanism

where ϕ is a scalar field and μ and λ are constants, the second term looks like a mass term, but the sign is wrong. But for this Lagrangian, the ground state is not $\phi = 0$. To find the ground state, one has to find the minimum of the potential $\mathscr{U} = -\frac{1}{2}\mu^2\phi^2 + \frac{1}{4}\lambda^2\phi^4$. The minimum is found to be

$$\phi_0 = \pm\frac{\mu}{\lambda} \tag{2.11}$$

Thus, $\mathscr{L}$ can be rewritten depending on a different field variable $\eta = \phi \pm \frac{\mu}{\lambda}$

$$\mathscr{L} = \frac{1}{2}(\partial_\mu\eta)(\partial^\mu\eta) - \mu^2\eta^2 \pm \mu\lambda\eta^3 - \frac{1}{4}\lambda^2\eta^4 + \frac{1}{4}(\mu^2/\lambda)^2 \tag{2.12}$$

Here, the second term has the correct sign to be a mass term. The third and fourth terms represent couplings of three and four particles and the fifth term is a constant.

While the Lagrangian in Eq. 2.10 was invariant under transformations as $\phi \rightarrow -\phi$, the Lagrangian in Eq. 2.12 is not even. Although the Lagrangian was symmetric in the beginning, this symmetry is lost when choosing one specific ground state to work with. This is often referred to as spontaneous symmetry-breaking. The system's symmetry, which is discrete in this example, is hidden by selecting one specific ground state.

A Lagrangian with spontaneously broken continuous symmetry could look like

$$\mathscr{L} = \frac{1}{2}(\partial_\mu\phi)^*(\partial^\mu\phi) + \frac{1}{2}\mu^2(\phi^*\phi) - \frac{1}{4}\lambda^2(\phi^*\phi)^2 \tag{2.13}$$

where two fields ϕ_1 and ϕ_2 have been combined into one complex field $\phi = \phi_1 + i\phi_2$. Here, ϕ is invariant under global $U(1)$ gauge transformations, $\phi \rightarrow e^{i\alpha}\phi$. As before, a gauge field A_μ and covariant derivatives have to be introduced to make it locally gauge invariant as well. If ϕ is split up in its real and imaginary parts,

$$\phi \rightarrow \phi' = (\cos\theta + i\sin\theta)(\phi_1 + i\phi_2) \tag{2.14}$$

and θ is chosen as $\theta = -\tan^{-1}(\phi_2/\phi_1)$, ϕ_2' will vanish (giving an additional degree of freedom to the massive particle) and ϕ' thus be real.

With this choice, the Lagrangian will render one massive particle, the 'Higgs' boson (the Lagrangian used here is only exemplary), and a massive gauge field A_μ.

$$\begin{aligned}\mathscr{L} = &\left(\underbrace{\frac{1}{2}(\partial_\mu\eta)(\partial^\mu\eta) - \mu^2\eta^2}_{\text{massive scalar particle}}\right) + \left(\underbrace{\frac{-1}{16\pi}F^{\mu\nu}F_{\mu\nu} + \frac{1}{2}\left(\frac{q\mu}{\lambda}\right)^2 A_\mu A^\mu}_{\text{free gauge field with mass}}\right) \\ &+ \left(\underbrace{\frac{\mu}{\lambda}q^2\eta(A_\mu A^\mu) + \frac{1}{2}q^2\eta^2(A_\mu A^\mu) - \lambda\mu\eta^3 - \frac{1}{4}\lambda^2\eta^4}_{\text{term defining couplings}}\right) + \left(\underbrace{\frac{\mu^2}{2\lambda}}_{\text{constant}}\right)^2\end{aligned} \tag{2.15}$$

The mechanism described above employing an example Lagrangian can be applied to the electroweak Lagrangian density. The scalar Higgs field in the Standard Model can be written as

$$\Phi = \begin{pmatrix} \Phi_3 + i\Phi_4 \\ \Phi_1 + i\Phi_2 \end{pmatrix} \tag{2.16}$$

Here, the Φ_i are real, the hypercharge Y is 1 and the weak isospin $I_W = 1/2$. This presentation is the simplest that satisfies the requirements, such as those of the symmetry breaking described below. The Higgs mechanism yields a possibility to explain the masses of W and Z bosons as well as those of the fermions, while the photon remains massless. Furthermore, it renders a massive scalar particle, the Higgs boson. Since the ground state of the Lagrangian shows $U(1)_Q$ symmetry but not $U(1)_Y \times SU(2)_{I_W}$, the scalar Higgs field has to have non-vanishing components of weak isospin and hypercharge but $q = 0$. The $U(1)_Y \times SU(2)_{I_W}$ symmetry of the electroweak theory is thus broken to $U(1)_Q$.

With the Higgs potential being of the form

$$V(\Phi) = -\mu^2\Phi^*\Phi + \lambda(\Phi^*\Phi)^2 \tag{2.17}$$

where $\mu^2 > 0$ and $\lambda > 0$, the ground state of the potential is found at $\Phi^*\Phi = \mu^2/2\lambda$. It is referred to as vacuum expectation value, usually called $v = \mu/\sqrt{\lambda}$.

For leptons, the same Higgs doublet can be used to generate the masses as for the W and Z bosons. By entering an $SU(2) \times U(1)$ gauge invariant term such as

$$L = \lambda_e(\bar{\nu}_e, \bar{e})_L \phi e_r + h.c. \tag{2.18}$$

where λ represents a Yukawa coupling for the first lepton generation into the electroweak Lagrangian and spontaneously breaking the symmetry, terms representing the coupling of leptons (here the first generation) to the Higgs boson appear.

For quarks, the same mechanism can be employed, but another Higgs doublet with opposite hypercharge has to be constructed from Φ, $\Phi_c = i\tau_2\Phi$ for generating masses of up-type quarks, where τ is an isospin matrix.

Although the Higgs mechanism only yields a way to explain the origin of masses and it is not possible to predict any of them, including the mass of the Higgs boson itself, relations between masses can be given:

$$\begin{aligned} M_W &= v\frac{g}{2} \\ M_Z &= v\frac{\sqrt{g' + g}}{2} \\ M_H &= v\sqrt{2\lambda} \end{aligned} \tag{2.19}$$

Here, g and g' are the coupling constants from $SU(2)_{I_W}$ and $U(1)_Y$. The masses of the gauge bosons and fermions are proportional to the vacuum expectation value times the Yukawa couplings. The mass of the Higgs boson is the only unknown parameter in the Standard Model.

The couplings of fermions (Hff) and gauge bosons (HVV, where V stands for $W^\pm$ or Z)

to the Higgs boson are given by

$$g_{Hff} = \frac{m_f}{v} \text{ and } g_{HVV} = \frac{2m_V^2}{v} \tag{2.20}$$

2.4.1 Constraints on the Standard Model Higgs boson

From theoretical arguments, the mass of the Standard Model Higgs boson has to be less than 850 GeV .

The vacuum expectation value and hence the mass of the Higgs boson is constrained by

$$\frac{G_F}{\sqrt{2}} = \frac{1}{2v^2} \Rightarrow v = 246\,\mathrm{GeV} \tag{2.21}$$

where G_F is the Fermi constant. Although the Higgs mechanism was developed in the 1960s, no experimental evidence for a Higgs boson could be found up to date.

In Figure 2.1, a fit of all Standard Model parameters to precision measurements is shown. From the minimum of the parabola one can extract that a light Higgs boson seems to be favored in the Standard Model. An upper limit on the Standard Model Higgs boson mass of 161 GeV at a 95% confidence level results from the fit.

At LEP, a Higgs boson lighter than 114.4 GeV could be excluded at a 95% confidence level [8] and the Tevatron experiments excluded a mass range between 156 and 177 GeV as well as between 100 and 108 GeV [9] at a 95% confidence level, shown in Figure 2.1.

Just recently, the CMS and ATLAS collaborations at the LHC excluded further mass ranges for the Standard Model Higgs boson, shown in Figures 2.2 and 2.3. CMS excluded the mass ranges between 149-206 GeV and between 300-440 GeV at a 95% confidence level. Similar ranges, between 155-190 GeV and 295-450 GeV have been excluded at a 95% confidence level by the ATLAS collaboration.

2.5 Beyond the Standard Model

Although the Standard Model has met most precision tests so far (for latest results see e.g. [7]), there are a few problems it provides no answer and solution to [13].

First, the Standard Model is based on the product of three gauge symmetries (accounting for strong, weak and electromagnetic forces) with separate coupling parameters. This symmetry combination seems to be arbitrary and an underlying symmetry is expected, which combines all forces within one single gauge group. In the Standard Model the coupling constants of the electromagnetic, weak and strong forces, do not meet. Thus a **G**rand **U**nified **T**heory (GUT) [14] based on one gauge group and involving one coupling constant only is not possible in the Standard Model.

In the last years, it has become clear that most matter in the universe is non-luminous, non-baryonic matter. It does not consist of any of the particles mentioned above appearing in the Standard Model. To explain this abundance of so-called Dark Matter, a new massive particle that is electrically neutral, non-relativistic and only very weakly interacting is needed [15].

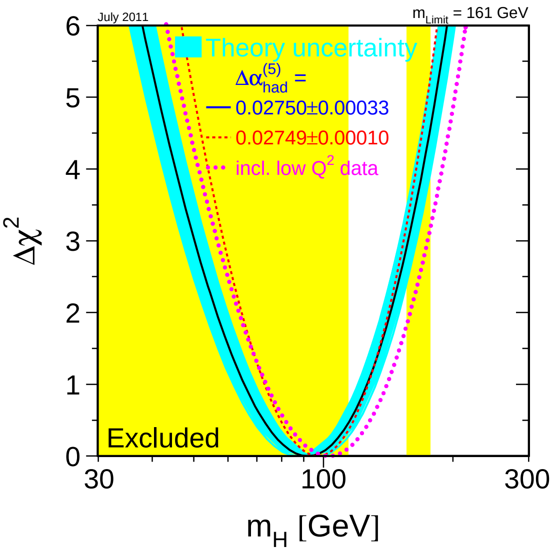

Figure 2.1: Fit of Standard Model parameters to precision measurements (parabola) and excluded mass ranges of the Standard Model Higgs boson at 95% confidence level. Masses below 114 GeV have been excluded by the LEP experiments, the mass range between 156 and 177 GeV by the Tevatron experiments (yellow areas) [10].

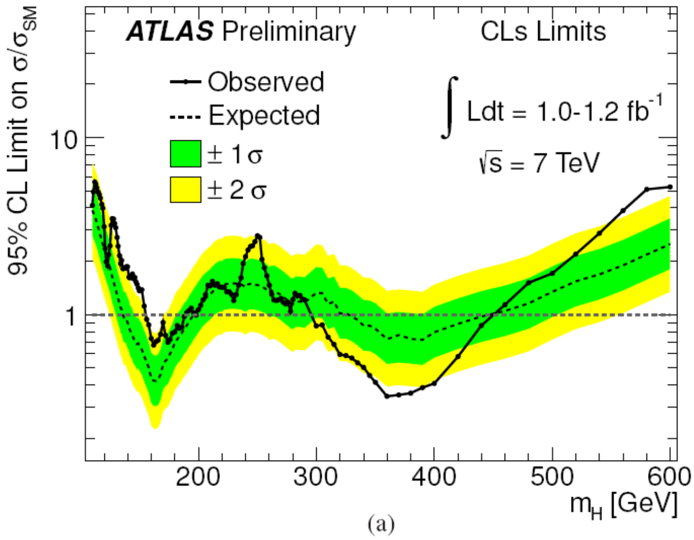

(a)

Figure 2.2: Upper limit on the Standard Model Higgs boson production cross section divided by the SM expectation extracted by the ATLAS collaboration. Wherever the solid black line dips under the dotted gray line, the corresponding Higgs boson mass is excluded at a 95% confidence level [11]

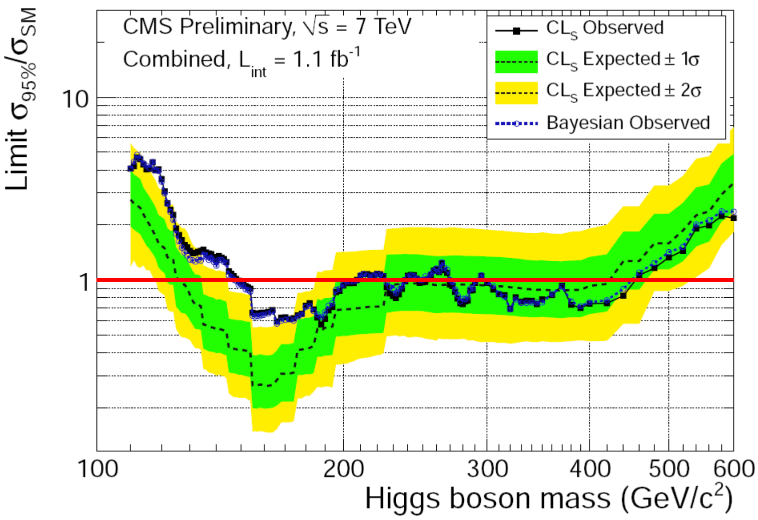

Figure 2.3: Upper limit on the Standard Model Higgs boson production cross section divided by the SM expectation extracted by the CMS collaboration. Wherever the black solid line dips under the red solid line, the corresponding Higgs boson mass is excluded at a 95% confidence level [12]

A third problem is the so-called fine-tuning or naturalness problem [16]. In the Standard Model, divergences that are quadratic in the cut-off scale (above which the theory is not valid anymore) appear when calculating radiative corrections to the Higgs boson mass. If the cut-off scale is chosen to be the GUT scale, the mass of the Higgs boson will be of this order, around 10^{16} GeV. To avoid this, very finely adjusted parameters are needed. This fine-tuning appears to be unnatural.

Supersymmetric (SUSY) extensions to the Standard Model can address these issues [17]. The Minimal Supersymmetric Standard Model or MSSM is one possibility of a supersymmetric Standard Model extension [18]. In supersymmetry, bosons are related to fermions and vice versa: for each quark and lepton from the Standard Model, squarks and sleptons are added with the same properties as their 'partner particles' but integer spin. For leftchiral and rightchiral fermions, supersymmetric partners are added separately. They are still referred to as chiral, although they have integer spin $s = 0$. For each gauge boson, a fermionic partner is added. Standard Model particles and their supersymmetric partners are combined in superfields. In supersymmetric theories, up-type quarks cannot be given masses by means of a conjugate Higgs field, making the introduction of a second Higgs doublet with hypercharge $Y = -1$ necessary. Furthermore, the supersymmetric partners of the first Higgs doublet spoil the cancelation of so-called gauge anomalies [19]. In the MSSM, this problem is fixed by the introduction of the second Higgs doublet.

The coupling constants of the electromagnetic, weak and strong forces meet in supersymmetric models such that a GUT would be valid at about 10^{16} GeV. If R-parity is introduced, a symmetry enforcing conservation of baryon and lepton numbers, a **l**ightest **s**upersymmetric **p**article (LSP) that is stable appears. This LSP is a natural candidate for Dark Matter. The naturalness problem is solved in supersymmetry because the loop corrections leading to divergences are canceled exactly. No fine-tuning is needed if the SUSY mass scale is at a few TeV.

If supersymmetry were an exact symmetry, the supersymmetric particles should have the exactly same masses as their Standard Model partners. Since no corresponding particles have been detected so far, supersymmetry (if it is realized in nature) cannot be exact but must be broken. The masses of supersymmetric particles are expected to be greater than those of the Standard Model particles. However, to solve the hierarchy problem of the Standard Model, the supersymmetric particles may not be too heavy. Furthermore, no quadratic divergences in the Higgs boson mass should appear and gauge invariance and renormalizability should be kept. Since so far no dynamical way has been found to break SUSY, the SUSY-breaking terms can be introduced manually. Thus the ignorance of the mechanism breaking SUSY can be evaded by adding parameters. The MSSM is one of these manually SUSY-broken theories. Without further constraints, 105 parameters appear in the MSSM, in addition to those of the Standard Model.

2.5.1 Non-minimal Higgs scenarios

The following introduction can only give a brief overview of non-minimal Higgs scenarios, especially to charged Higgs bosons which are of interest in the following analyses. Further information can be found in e.g. [13].

The Higgs sector of the MSSM is a so-called Type II-2HDM. 2HDM here means 2 Higgs Doublet Model, an unspecific Higgs potential that is compatible with gauge invariance. The type refers to the mass generation of fermions: in Type II models, the masses of isospin down-type fermions are generated by one Higgs field and those of isospin up-type fermions by the other Higgs field. The doublets consist of complex scalar fields that have opposite hypercharges Y:

$$H_1 = \begin{pmatrix} H_1^0 \\ H_1^- \end{pmatrix} \text{ with } Y_{H_1} = -1 \qquad H_2 = \begin{pmatrix} H_2^+ \\ H_2^0 \end{pmatrix} \text{ with } Y_{H_2} = +1 \tag{2.22}$$

After electroweak symmetry breaking both fields obtain a non-vanishing vacuum expectation value. The vacuum expectation values of the neutral fields are

$$\langle H_1^0 \rangle = \frac{v_1}{\sqrt{2}} \text{ and } \langle H_2^0 \rangle = \frac{v_2}{\sqrt{2}} \tag{2.23}$$

The relation

$$(v_1^2 + v_2^2)^2 = v^2 \propto \frac{1}{G_F} \tag{2.24}$$

where v is the Standard Model vacuum expectation value holds.

The parameter $\tan\beta$ is defined as

$$\tan\beta = \frac{v_2}{v_1} \tag{2.25}$$

The complex scalar fields H_1 and H_2 have to be developed around the vacuum into real and imaginary parts in order to get the physical Higgs fields and masses. Three of the eight degrees of freedom of the Higgs doublets give masses to the W- and Z- bosons, just as in the Standard Model. But other than in the Standard Model, not one but five Higgs bosons are left: three electrically neutral ones, usually called h, H and A, and two charged ones, called H^+ and H^-.[6] The Higgs bosons h and H are CP-odd while A is even under CP transformation.

In the MSSM, the supersymmetric partners of the γ, W, Z and Higgs bosons will mix to so-called neutralinos and charginos.

Due to the supersymmetric structure, constraints are imposed on multiple parameters, resulting in only two completely independent ones. These are usually taken to be $\tan\beta$ and m_A or m_{H^+}. Also, a strong hierarchy exists in the mass spectrum, although masses are not fixed to any values but rather depend on each other and Standard Model particle masses.

The charged Higgs bosons are obtained from a mixing of the charged parts of the Higgs doublets.

$$H^\pm = -\sin\beta \cdot H_1^\pm + \cos\beta \cdot H_2^\pm \tag{2.26}$$

In the MSSM, their mass is constrained at Born level by

$$m_{H^+} = \sqrt{m_W^2 + m_A^2} \tag{2.27}$$

The mass of the lightest Higgs boson, m_h is constrained to be less than the mass of the Z boson, but can be lifted up to $\approx 140\,\mathrm{GeV}$ due to radiative corrections.

In the MSSM, the coupling of charged Higgs bosons to fermions is proportional to $m_d \tan\beta + m_u \cot\beta$, where the $m_{u(d)}$ stand for up- (down-)type quark masses, respectively. Thus if $\tan\beta > 1$, the coupling of charged Higgs bosons to isospin down-type fermions is enhanced while that to up-type fermions is suppressed. The coupling to b quarks e.g. is then very strong for large $\tan\beta$.

For the decay of charged Higgs bosons, the branching ratios BR into quarks or leptons in dependence of the respective masses and β are given by

$$\begin{aligned} BR(H^+ \to u\bar{d}) &\propto m_u^2 \cot^2\beta + m_d^2 \tan^2\beta \\ BR(H^+ \to l\nu_l) &\propto m_l^2 \tan^2\beta \end{aligned} \tag{2.28}$$

Hence for the branching ratio of charged Higgs bosons into leptons, it is expected that mostly decays involving τ leptons and ν_τ occur. For a light charged Higgs boson, i.e. $m_{H^+} < m_{top}$ and $H^+ \to t\bar{b}$ is thus kinematically not allowed, the decay channel $H^+ \to c\bar{s}$ is important if $\tan\beta < 1$.

---

[6] For the rest of this thesis, H^+ always refers to both charged Higgs bosons such that charge-conjugate processes will always be implied if not named explicitly.

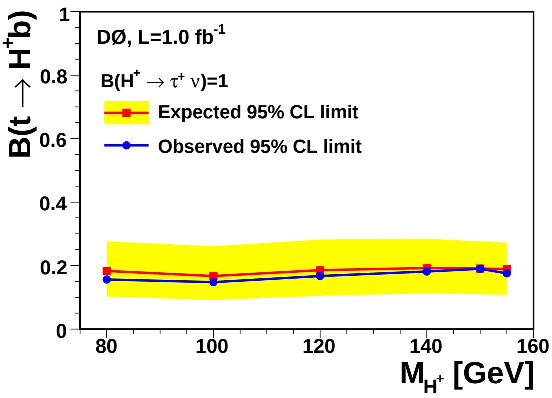

Figure 2.4: Exclusion limits on the branching ratio $t \longrightarrow H^+b$ depending on assumed charged Higgs boson masses from the D0 experiment at Tevatron [21]. For the decay, $H^+ \longrightarrow \tau\nu = 1$ is assumed.

2.5.2 Results on charged Higgs boson searches from earlier experiments

Earlier experiments, such as those at LEP or Tevatron, have set limits on the masses of charged Higgs bosons. So far, no excess of data over the Standard Model background expectation has been observed at any experiment in charged Higgs boson searches.

From LEP, a constraint on m_{H^+} for general 2HDM of $m_{H+} > 78.6\,\text{GeV}$ results [22].

Upper limits have been set on the branching ratio $t \longrightarrow H^+b$ assuming different masses and decay channels of the charged Higgs boson by the Tevatron experiments. In Figure 2.4, the exclusion limits on the charged Higgs boson mass from the D0 experiment are shown. The m_h^{max} scenario [23] is assumed in this plot.

This MSSM benchmark scenario is characterized by the parameters being chosen such that depending on $\tan\beta$, the maximum possible Higgs boson mass is obtained for h with m_A set to the maximum value of 1 TeV. Depending on the charged Higgs boson mass, branching ratios $t \longrightarrow H^+b$ up to about 20% were excluded with data corresponding to an integrated luminosity of $1\,\text{fb}^{-1}$ assuming $H^+ \longrightarrow \tau\nu = 1$.

Just recently, the CMS collaboration has published new limits on the branching ratio $t \longrightarrow H^+b$. In Figure 2.5 they are shown for different masses of the charged Higgs boson assuming $H^+ \longrightarrow \tau\nu = 1$. Branching ratios $t \longrightarrow H^+b$ up to 4-5% have been obtained in a mass range $80 < m_{H^+} < 160\,\text{GeV}$.

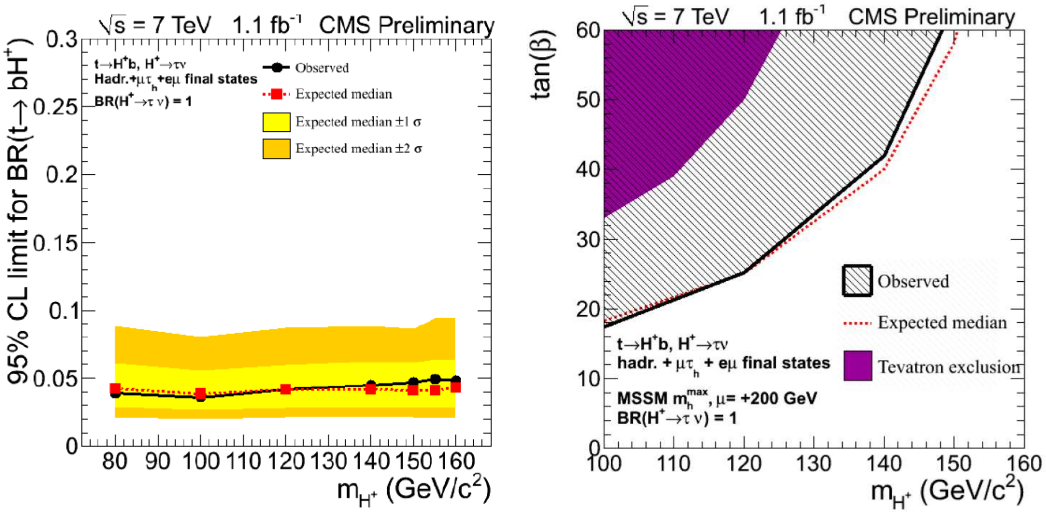

Figure 2.5: Limits on the branching ratio $t \longrightarrow H^+ b$ assuming $\mathrm{BR}(H^+ \longrightarrow \tau\nu = 1)$ at a 95% confidence level (left) and the corresponding exclusion region in the $\tan\beta$-m_{H^+}-plane assuming the m_h^{max} scenario, extracted by the CMS collaboration [24].

3 The ATLAS detector at LHC

3.1 The LHC

The LHC (**L**arge **H**adron **C**ollider) is a particle accelerator at CERN near Geneva, Switzerland. Situated in the former LEP (Large Electron-Positron Collider) tunnel it measures about 27 km in circumference. It can be run in two modes, either colliding high-energy protons or heavy ions. With a design center-of-mass energy of 14 TeV, it pushes the frontier of high energy physics to a new limit. Not only should a Higgs Boson be found here (if it exists), but the potential is offered to rule out or confirm models describing physics beyond the Standard Model at the TeV scale.

The four major LHC experiments are placed in caverns 50 to 150 m underground: ATLAS, CMS, LHCb and ALICE, illustrated in Figure 3.1. While ATLAS and CMS are multi-purpose physics experiments, LHCb and ALICE are specialized in studying b- and heavy ions physics, respectively.

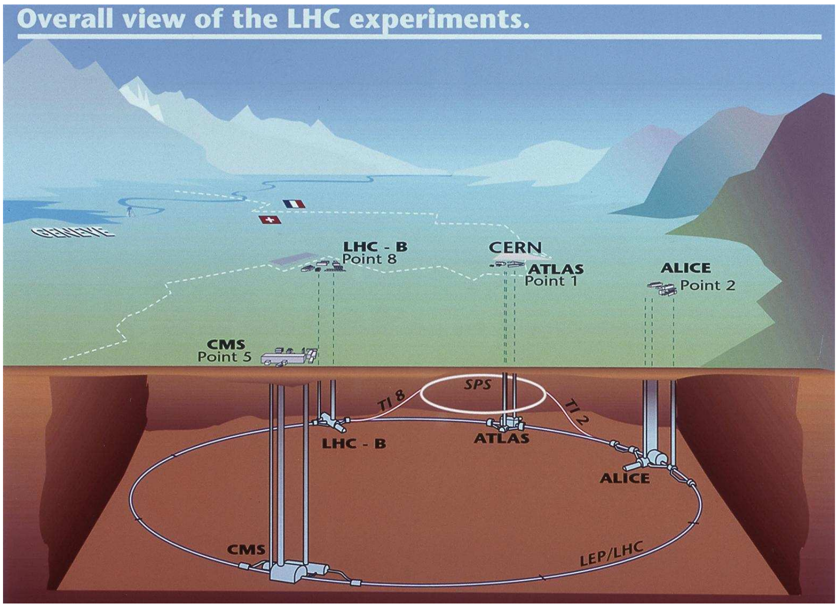

Figure 3.1: Overview of the LHC and major experiments [25].

In 2008, the first beams circled the LHC, but after an accident repairs made it necessary to shut the machine down for about a year. On November 23rd, 2009, first collisions were observed at a center-of-mass energy of 900 GeV. In March 2010, collisions at a center-of-mass energy of 7 TeV were achieved. Starting off with proton-proton collisions at an instanta-

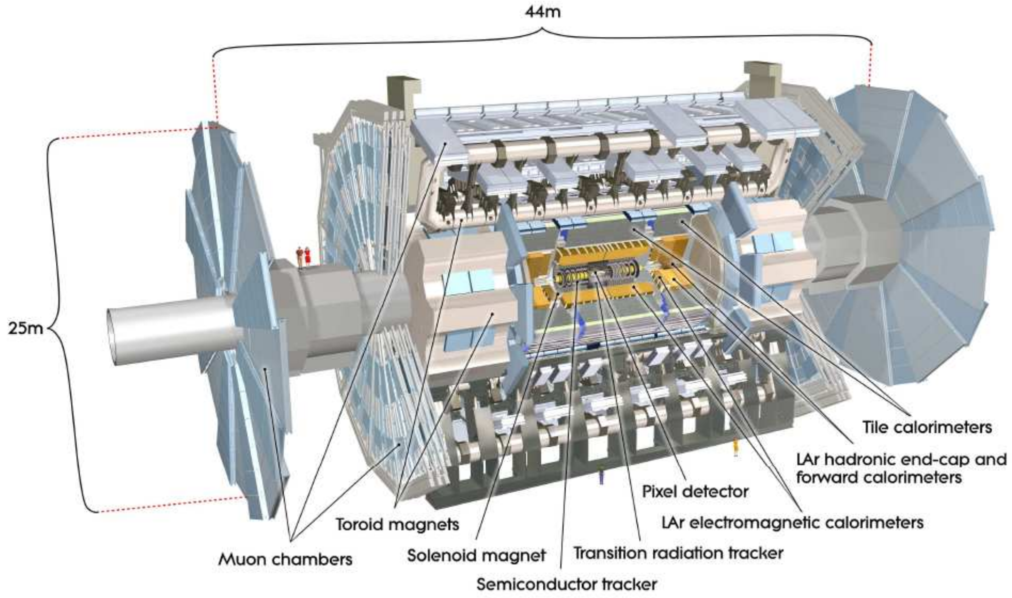

Figure 3.2: The ATLAS detector [28]

neous luminosity of $8{\cdot}10^{26}\,\mathrm{s}^{-1}\mathrm{cm}^{-2}$ in March 2010, LHC was operated until December 2010, reaching a luminosity of $2{\cdot}10^{32}\,\mathrm{s}^{-1}\mathrm{cm}^{-2}$ in October before a heavy-ion run started and a winter break was taken [26]. In March 2011, operation was taken up again. During the proton-proton run in 2010 an integrated luminosity of 42 to 48 pb^{-1} of data was delivered to the different experiments [26], with ATLAS recording about 45 pb^{-1} [27]. It is planned to keep the current LHC run at 7 TeV in 2011 and 2012, before a major upgrade will make it possible to run at the design center-of-mass energy of 14 TeV.

3.2 The ATLAS detector

ATLAS (**A** **T**oroidal **L**HC **A**pparatu**S**) [28] is one of the two general-purpose physics experiments at the LHC, shown in Figure 3.2. It measures 44 m in length, 25 m in diameter and weighs about 7000 tons.

The coordinate system used to describe processes in the ATLAS detector is centered around the nominal interaction point, which is defined as origin. The positive x-axis is defined as pointing from the interaction point towards the center of the accelerator ring, the positive y-axis as pointing upward towards the surface and the z-axis is defined as the beam direction such that a right-handed coordinate system results.

The polar angle θ is measured from the beam axis while ϕ, the azimuthal angle, is measured around the beam axis. The pseudorapidity η is defined by $\eta = -\ln\tan(\theta/2)$. The angular distance in an η-ϕ-space, ΔR, is given by $\Delta R = \sqrt{(\Delta\eta)^2 + (\Delta\phi)^2}$.

impact parameter	$0.25 < \|\eta\| < 0.50$		$1.50 < \|\eta\| < 1.75$	
	$\sigma_X(\infty)$ [μm]	p_X [GeV]	$\sigma_X(\infty)$ [μm]	p_X [GeV]
transverse: d_0	10	14	12	20
longitudinal: $z_0 \sin\theta$	91	2.3	71	3.7

Table 3.1: Track-parameter resolutions expected at infinite transverse momentum and p_T for two $|\eta|$ regions, corresponding to regions in the barrel and end-caps. Formula to calculate resolution corresponding to a certain transverse momentum is given in the text. Values are shown for pions. Table adapted from [45].

High energies and particle densities at the LHC make it necessary for the detector to be extremely resistant against radiation to avoid damage. Read-out electronics must be fast in order to cope with the interaction rate, which will be about 40 MHz at a luminosity of $10^{33}\,\mathrm{cm}^{-2}\mathrm{s}^{-1}$. As most of the collisions yield uninteresting processes, a trigger system is implemented to reduce the rate of events that are saved for further analysis. Precise reconstruction of particles requires high detector granularity and good momentum resolution. These demanding requirements determined the design of the different parts of ATLAS.

3.2.1 Tracking detectors

The Inner detector (ID), consisting of several tracking detectors, is the most central part of ATLAS, illustrated in Figure 3.3. It is important for precise momentum measurement, reconstruction of track parameters and reconstruction of primary and secondary vertices. Secondary vertex reconstruction is especially important for b-tagging (see chapter 5.)

The ID encloses the beam pipe and is immersed in a 2 T magnetic field, generated by the central solenoid. It consists of pixel and silicon microstrip trackers (SCT), especially important at small radii, combined with a transition radiation tracker (TRT) which covers a range up to $|\eta| < 2.0$. Each of these parts is made up of a barrel region, where pixel and SCT detectors are placed concentrically around the beam axis while the straw tubes of the TRT run parallel to it, and two end-caps with radially mounted detectors. Together, they provide the fine granularity needed for precise momentum and vertex measurements ($\sigma_{p_T}/p_T = 0.05\% p_T \oplus 1\%$) in a range up to $|\eta| < 2.5$.

The resolution of the longitudinal and transverse impact parameters, $z_0 \sin\theta$ and d_0, σ_X, where X is either d_0 or $z_0 \sin\theta$, depends on $|\eta|$, is a function of the transverse momentum p_T and is given by $\sigma_X(p_T) = \sigma_X(\infty)(1 \oplus p_X/p_T)$. Here, $\sigma_X(\infty)$ is the resolution of the track parameter expected at infinite momentum and p_X is a constant and represents the transverse momentum for which multiple-scattering and intrinsic terms are equal for the track parameter considered. The corresponding values for two pseudorapidity regions corresponding to barrel and end-caps are given in Table 3.1.

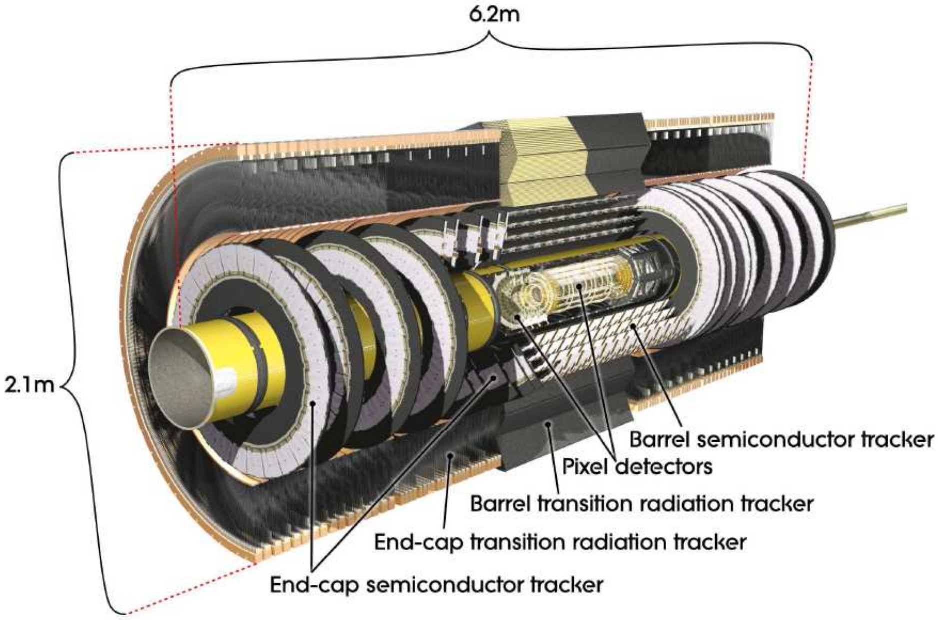

Figure 3.3: The inner detector [28]

3.2.2 Calorimeters

The ATLAS calorimeter system is shown in Figure 3.4. The individual components are optimized for measuring several quantities.

Electromagnetic calorimeter The electromagnetic calorimeter uses lead - liquid Argon sampling technology, and is optimized for measuring the energy of photons and electrons very precisely. This is made possible by the fine granularity. It is divided into a barrel part, which is itself divided into two identical half-barrels, covering a pseudorapidity range up to $|\eta| < 1.475$ and two end-caps, each consisting of an inner and an outer wheel, covering the range $1.375 < |\eta| < 3.2$. The electromagnetic calorimeter is built of accordion-shaped electrodes and lead absorber plates, guaranteeing a complete symmetry in ϕ. The lead absorber plates have been optimized in thickness with respect to energy resolution, reaching a resolution of $\sigma_E/E = 10\%/\sqrt{E} \oplus 0.7\%$. The granularity of the electromagnetic calorimeter depends on the layer and pseudorapidity range. Values for the granularity in $\Delta\eta \times \Delta\phi$ lie between $0.025/8 \times 0.1$ and 0.1×0.1 and are similar for barrel and end-caps.

To compensate energy that electrons and photons lost upstream of the calorimeter, a presampler detector is added in the region $|\eta| < 1.8$ in the barrel. It consists of an active liquid Argon layer.

Hadronic calorimeters The hadronic calorimeters have a coarser granularity than the electromagnetic calorimeter, fulfilling the needs for reconstruction of jets and measurements of missing transverse energy. The barrel part of the hadronic calorimeters consists of a

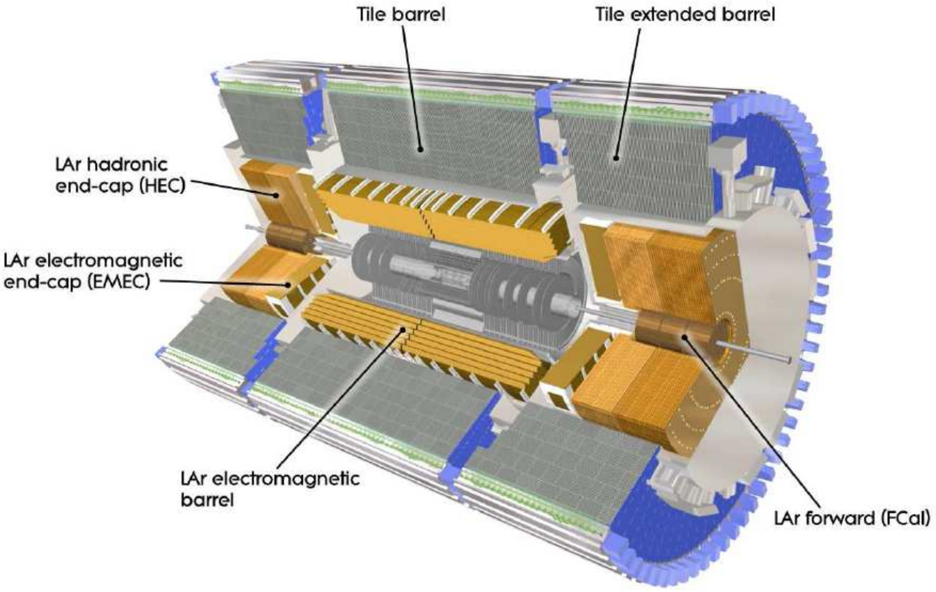

Figure 3.4: The calorimeter system [28]

tile calorimeter around the barrel of the electromagnetic calorimeters and two extended barrels covering a larger $|\eta|$-range. Scintillating tiles are used as active material while steel plates serve as absorber. The barrel and extended barrel cover the region in $|\eta| < 3.2$. The hadronic end-cap calorimeter (HEC) and forward calorimeter (FCal) both use liquid Argon as the sensitive material. Copper plates are used as absorbers in the HEC and both copper and tungsten are used in the FCal. The HEC is made up of two wheels in each end-cap with the FCal in the center, right around the beam pipe. The part of the FCal closest to the interaction point measures mostly electromagnetic interactions, while the other two parts have been optimized for hadronic measurements. Due to the chosen geometry, with some parts of calorimeters overlapping with others or sharing cryostats, uniformity of calorimetric coverage is improved. The forward calorimeter extends the pseudorapidity range to $|\eta| < 4.9$. For the barrel and end-cap calorimeters, an energy resolution of $\sigma_E/E = 50\%/\sqrt{E} \oplus 3\%$ is achieved while for the FCals this is $\sigma_E/E = 100\%/\sqrt{E} \oplus 10\%$ for jets.

The resolution of the missing transverse energy, E_T^{miss}, depends on the transverse energy sum, ΣE_T and follows a function $\sigma_{E_T^{miss}} = a \cdot \sqrt{\Sigma E_T}$ if $20 < \Sigma E_T < 2000\,\mathrm{GeV}$. Values for a vary between 0.53 and 0.57.

3.2.3 Muon system

Measurement of muon tracks and momenta relies on the bending power of the magnetic field generated by superconducting air-core toroids. One of these toroids with eight coils covers the barrel region, two more systems of eight coils, each perpendicular to the first one provide the magnetic field in the end-caps. The coils in each of the systems are arranged symmetrically around the beam axis. Those in the end-cap toroids are rotated with respect to the barrel coils. Because of this geometry, the magnetic field is orthogonal to the muon tracks. The muon system is presented in Figure 3.5.

Monitored Drift Tubes (MDTs) are installed over a pseudorapidity range up to $|\eta| < 2.7$ for precise measurement of the muon track coordinates. For large $|\eta|$, Cathode Strip Chambers (CSCs) are used as well, covering a range $2.0 < |\eta| < 2.7$. The chambers for measuring muon tracks all exist threefold, in the barrel region on three layers arranged cylindrically around the beam axis and in the end-caps on three layers perpendicular to the barrel. In the muon system, a momentum resolution of $\sigma_{p_T}/p_T = 10\%$ is achieved for muons with $p_T = 1\,\mathrm{TeV}$.

The muon trigger system consists of two parts: Resistive Plate Chambers (RPCs) in the barrel ($|\eta| < 1.05$) and Thin Gap Chambers (TGCs) in the end-caps ($1.05 < |\eta| < 2.7$, $|\eta| < 2.4$ for triggering). They are necessary for measuring the coordinates of the muon trajectory orthogonal to the one measured by the tracking chambers. Furthermore, they supply identification of bunch-crossing and provide distinct transverse momentum thresholds.

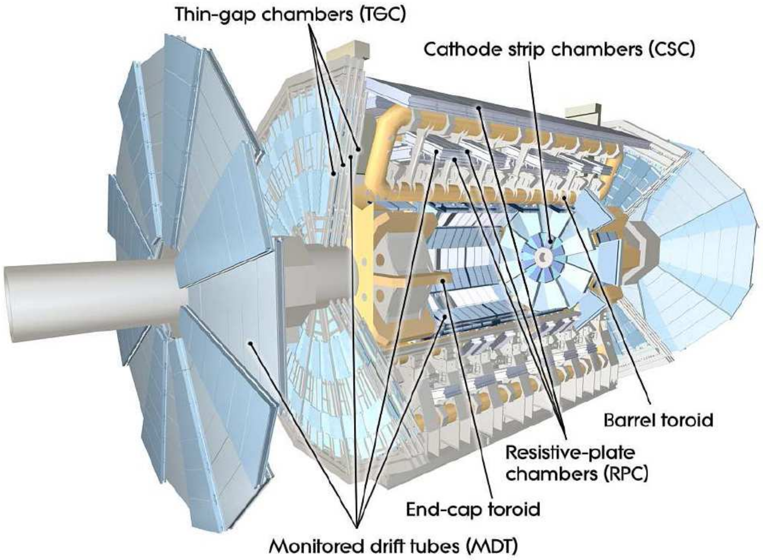

Figure 3.5: The muon system [28]

3.2.4 Trigger system

The trigger consists of three levels: level 1 (L1), level 2 (L2) and event filter (EF).

L1 triggers on muons, electrons, jets and photons with high transverse momentum, but also large total or missing transverse energy, taking about $2.5\,\mu$s to make a decision. One or several Regions of Interest (RoIs) in η and ϕ are defined if interesting features are detected. Information such as what kind of object or thresholds passed are also saved for usage of higher level triggers. Level 1 is designed to reduce the trigger rate to about 75 kHz.

L2 then refines the selection using all the detector information of the RoIs defined by L1, thus lowering the trigger rate significantly to about 3.5 kHz. About 40 ms are needed to process one event.

Finally, the EF selects events applying offline analysis routines, reaching a final event rate of approximately 200 Hz. Processing an event takes about 4 s.

4 Signal process, backgrounds and collision data

4.1 Signal process

If charged Higgs bosons exist in nature and if they are lighter than the top quark, the main production mode for them at the LHC is expected to be via top quark pair decays. Instead of the Standard Model process $t\bar{t} \rightarrow W^{+}bW^{-}\bar{b}$, one of the top quarks could decay to a charged Higgs boson and a b quark: $t\bar{t} \rightarrow H^{+}bW^{-}\bar{b}$. The leading-order Feynman diagram of the signal process is shown in Figure 4.1.

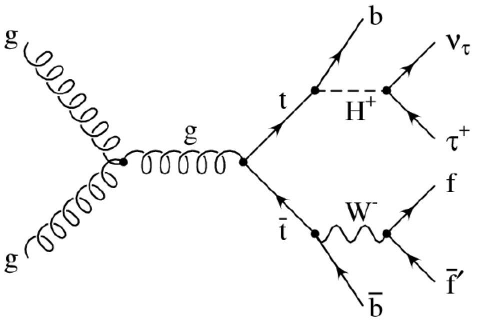

Figure 4.1: Leading-order (LO) Feynman diagram for the signal channel. The W boson can decay either leptonically or hadronically, but only hadronic decays are considered in the following. The charged Higgs boson decay to $\tau + \nu$ is important for most values of m_{H^+} and $\tan\beta$ [55].

Cross sections for charged Higgs boson production at a center-of-mass energy of 7 TeV are shown in Figure 4.2 assuming different values for $\tan\beta$ and m_{H^+} for the m_h^{max} scenario [29]. With increasing $\tan\beta$, cross sections decrease from $\tan\beta = 2$ to $\tan\beta = 8$ and then increase again. For all values of $\tan\beta$, the cross sections quickly decrease as the mass of the charged Higgs boson increases. For $m_{H^+} < m_{top}$, charged Higgs bosons result from top quark decays, whereas for a charged Higgs boson mass greater than that of the top quark, the production takes place via $gg/gb \rightarrow t[b]H^{+}$. At around the top mass, a bend can be seen in Figure 4.2, corresponding to the change of the production mechanism.

For light charged Higgs bosons, the cross section results from the top quark pair production cross section and the branching ratio for top quarks decaying to a charged Higgs boson and a b quark.

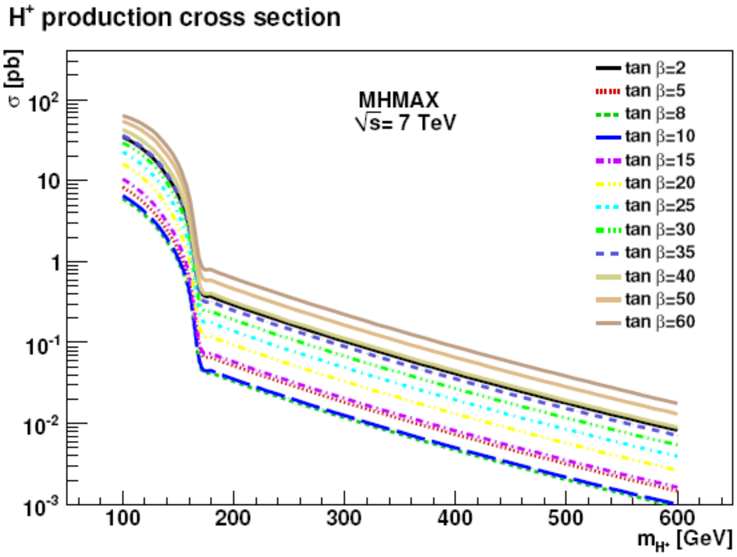

Figure 4.2: Production cross sections for charged Higgs bosons at $\sqrt{s} = 7\,\text{TeV}$ for the m_h^{max} scenario assuming different values of $\tan\beta$ [29].

In Figure 4.3, the branching ratios of charged Higgs bosons for two different values for $\tan\beta$ are shown as a function of m_{H^+} in the m_h^{max} scenario. The final states shown in this Figure include supersymmetric ones, which will be sizable if existent and kinematically available. The branching ratio to $\tau + \nu$ is large for most charged Higgs boson masses if $\tan\beta$ is not too small.

In the following studies, a branching ratio of $H^+ \rightarrow \tau\nu = 1$ is assumed. Only hadronically decaying τ leptons are considered and the W boson from the top quark pair decay is assumed to decay hadronically as well. Thus the final state investigated is defined by a hadronically decaying τ lepton, 2 b jets, 2 other jets and missing transverse energy due to the two neutrinos in the decay chain. In the signal selection, only one jet identified as b jet

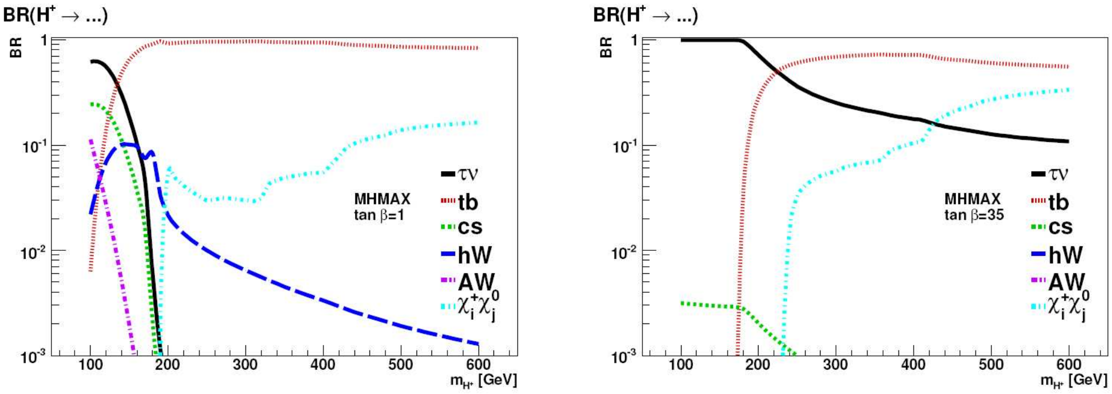

Figure 4.3: Branching ratios of charged Higgs bosons assuming a low (left) and high (right) value of $\tan\beta$ in the m_h^{max} scenario [29].

will be required since requiring 2 identified b-jets results in efficiencies that are too low.

The signal sample is generated with PYTHIA [30]. PHOTOS [31] is used to add photon radiation off charged leptons and TAUOLA [32] for the decay of τ leptons. The ATLAS Minimum Bias Tune (AMBT1) [33] is used. A charged Higgs boson mass of $m_{H^+} = 130\,\text{GeV}$ and $\tan\beta = 35$ is assumed. The charged Higgs boson NLO+NNLL [34] cross section is assumed to be 18.467 pb, resulting from a $t\bar{t}$ cross section of 164.6 pb [42] and corresponding to a branching ratio $t \rightarrow H^+ b$ of about 6%. The branching ratio $H^+ \rightarrow \tau\nu = 1$ is assumed.

4.2 Background processes

Relevant background processes to the charged Higgs boson searches presented in the following include production of $t\bar{t}$ pairs with Standard Model decays, single top production in the s- and t-channel and associated Wt production, W + jets, Z + jets and QCD multi-jet events. The cross sections for all processes considered in the analyses presented in the following chapters are summarized in Table 4.1. K-factors are included for some samples so that lower order cross sections match NNLO calculations. Monte Carlo simulation samples generated using HERWIG [35] and JIMMY [36] use the ATLAS Underlying Event Tune 1 (AUET1) [37] while samples using PYTHIA use the AMBT1. For ALPGEN [38] samples the MLM matching scheme [39] is used to avoid double counting of partons arising from parton shower or matrix element calculations. For this, the ΔR cut is set to 0.7 and the jet p_T cut to 20 GeV. Detailed ATLAS detector simulation [40] using GEANT4 [41] is run on all events. They are reconstructed using the same algorithms as for data.

Vertex Reweighting Because the vertex distribution in simulation samples follow a Poisson distribution but those in collision data do not, which has an impact on distributions of other variables, vertex reweighting has been applied to simulation. The vertex distributions in simulated events are scaled to match data, i.e. events in Monte Carlo simulation are weighted with a factor from the rescaling of the vertex distributions.

Top quark pair production Standard Model $t\bar{t}$ decays, shown in Figure 4.4, are partly an irreducible and the most important background to the signal process. Samples with at least one charged lepton are considered. The Standard Model process $t\bar{t} \rightarrow W^+ b W^- \bar{b}$ can occur with the same final state as the signal, and can be potentially selected with little rejection. $t\bar{t}$ decays with different final states, that is with the W bosons decaying to everything else but $\tau + \nu$ and quarks but including at least one lepton, can be better suppressed. But since particles in these different final states may be incorrectly identified (e.g. electrons or muons faking τ jets), these events may also pass the signal selection.

An NLO+NNLL $t\bar{t}$ cross section of 164.6 pb is used [42]. If a charged Higgs boson exists and the $t\bar{t}$ production cross section stays the same as in the Standard Model, the branching ratio $t \rightarrow Wb$ will be reduced according to the branching ratio $t \rightarrow H^+ b$. This leads to a smaller cross section of Standard Model $t\bar{t}$ decays.

process	cross section [pb] (·K-factor)
$t\bar{t} \to H^+bWb \to \tau\nu bqqb$ ($m_{H^+} = 130\,\text{GeV}$, $\tan\beta = 35$)	18.467
$t\bar{t}$	164.6
$t\bar{t}$ ($\geq$ 1lepton)	89.7
$W(\to \mu\nu)$ + 1 jet	1281 (·1.20)
$W(\to \mu\nu)$ + 2 jets	375 (·1.20)
$W(\to \mu\nu)$ + 3 jets	101 (·1.20)
$W(\to \mu\nu)$ + 4 jets	25.7 (·1.20)
$W(\to \mu\nu)$ + 5 jets	7 (·1.20)
$W(\to \tau\nu)$ + 1 jet	1277 (·1.20)
$W(\to \tau\nu)$ + 2 jets	377 (·1.20)
$W(\to \tau\nu)$ + 3 jets	101 (·1.20)
$W(\to \tau\nu)$ + 4 jets	25.7 (·1.20)
$W(\to \tau\nu)$ + 5 jets	7 (·1.20)
$Z(\to \mu\mu)$ + 1 jet	132.8 (·1.25)
$Z(\to \mu\mu)$ + 2 jets	39.6 (·1.25)
$Z(\to \mu\mu)$ + 3 jets	11.1 (·1.25)
$Z(\to \mu\mu)$ + 4 jets	2.8 (·1.25)
$Z(\to \mu\mu)$ + 5 jets	0.8 (·1.25)
$b\bar{b}$ (with μ filter)	73900
QCD dijet	$4.4066 \cdot 10^7$
single top (Wt associated production)	14.581
single top (s-channel, $\tau\nu$)	0.4700
single top (t-channel, $\tau\nu$)	7.128

Table 4.1: Monte Carlo simulation samples included in the signal (τ final states) or embedding (μ final states) cut optimization and corresponding NLO+NNLL cross section for $t\bar{t}$, NLO for single top and LO cross sections for all other samples in pb. For some samples, K-factors have been included to match NNLO calculations when comparing estimates from data-driven methods to events in collision data.

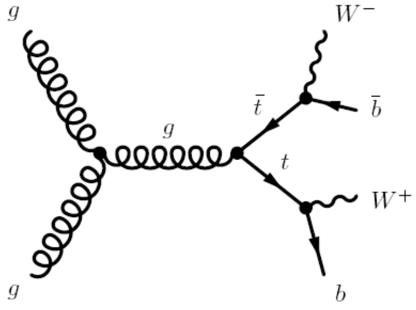

Figure 4.4: Leading order Feynman diagram of a Standard Model top quark pair decay [60].

$t\bar{t}$ samples are generated with MC@NLO [43], with HERWIG used for hadronization and JIMMY for the underlying event.

Single top Single top processes in the s- and t-channel and in associated production with a W boson are taken into account.

In the s-channel, the final state includes a t and a b quark. These events can mimic signal events if $t \rightarrow Wb \rightarrow \tau\nu b$ and there are additional jets. The W boson could also decay hadronically, leading to two jets and a b-tagged jet. If additional jets are present and one of these is mis-tagged as a τ, these single top processes can also pass the signal selection. The W boson could also decay leptonically to a muon or electron, which might be mis-tagged as a τ, leading potentially to a final state detected as the signal final state. The cross section for these events is very small and only very few events are expected to be identified as signal

The final state in the t-channel includes a top quark, a b quark and an additional jet. With $t \rightarrow Wb \rightarrow \tau\nu b$ or the W boson decaying to other leptons which are mis-tagged, events can be identified as signal. The W boson could also decay hadronically. If then a jet is misidentified as τ jet and the transverse energy is measured incorrectly, missing transverse energy results and the event may pass the signal selection as well. Because the final state features an extra jet compared to the s-channel, t-channel events are more likely to pass signal selection. Also, t-channel processes are more abundant compared to the s-channel due to a larger cross section.

Processes with a single top quark produced in association with a W boson can easily be mistaken as signal. With the top quark decaying to a b quark and a W boson, which itself can decay to a τ lepton and a neutrino and the other W boson decaying hadronically, almost the same particles are present as in signal processes. Since b-jets are often not correctly identified, these events can easily pass the signal selection.

Single top sample generation is done with MC@NLO, HERWIG and JIMMY. Overlap between single top and $t\bar{t}$ is removed [44]. Cross sections obtained from the MC@NLO output are used.

W + jets Samples with a W boson decaying leptonically and up to five additional partons are taken into account as backgrounds. Since the signal process includes many jets, the backgrounds featuring less additional partons are easier to suppress. If the W boson e.g. decays to $\tau + \nu$ or other leptons which are misidentified, one of the jets is tagged as a b jet and due to the neutrino there is missing transverse energy, this process can be identified as having the same final state as the signal. Also, the W boson can decay hadronically, one of the many jets in the event can be mis-tagged as a τ, one jet can be tagged as a b jet and the transverse energy can be mis-measured, resulting in missing transverse energy and a final state similar to that of the signal. W + jets events with more than one additional parton are an important background to the signal process.

W+jets sample generation is done using ALPGEN with HERWIG and JIMMY. NNLO cross sections are used, resulting from LO cross sections and K-factors to match NNLO calculations.

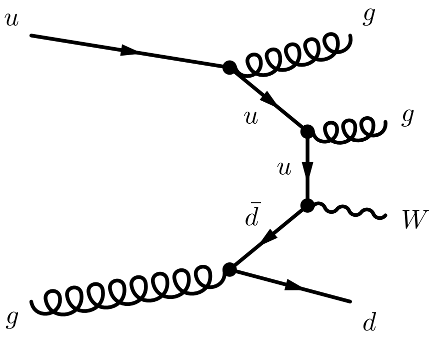

Figure 4.5: Exemplary Feynman diagrams for W+jets production [60].

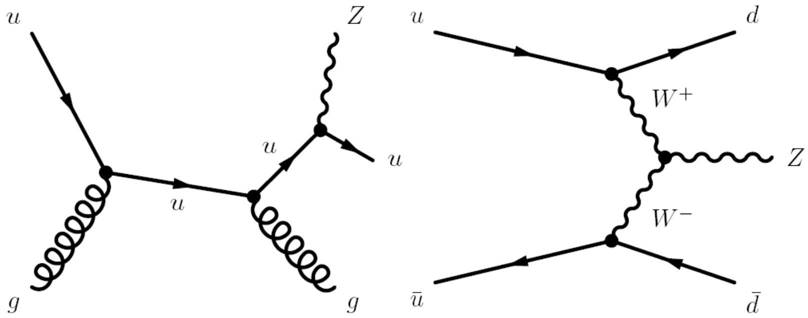

Figure 4.6: Exemplary Feynman diagrams for Z+jets production [60].

Z + jets As for W+jets, samples with a Z boson decaying leptonically and up to five additional partons are considered. With possibly a τ lepton in the final state or other leptons being mis-identified as a τ, mismeasurement of the transverse energy, many jets, and one of the jets might be b-tagged, these events can mimic signal processes and be selected as such. Z bosons can also decay hadronically. If then one jet is mis-identified as a τ-jet, one jet is b-tagged and mismeasurement of the transverse energy results in missing transverse energy, Z+jets processes can be identified as having the same final state as the signal process. Nevertheless, Z+jets backgrounds can be suppressed very well and are negligible after signal selection.

Z+jets samples are generated using ALPGEN, also with HERWIG and JIMMY. LO cross sections are used with K-factors to match NNLO calculations.

QCD, $b\bar{b}$ QCD samples are taken into account because they include many jets and can include leptons. If a jet is tagged as b jet, the transverse energy is mis-measured and a jet is identified as τ jet, QCD events can pass the signal selection if enough jets are present. Exploiting the topology of the signal process, QCD background events can be suppressed well.

The QCD and $b\bar{b}$ samples are generated using PYTHIA, with PHOTOS used for radiation off charged leptons. The cross sections used are LO.

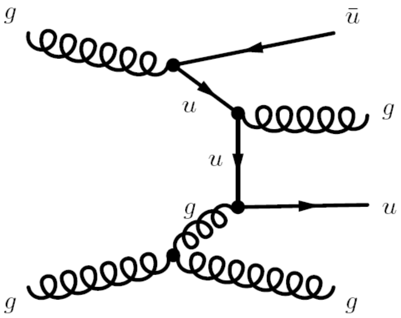

Figure 4.7: Exemplary Feynman diagram for a multi-jet process [60].

4.3 Collision data

Collision data taken by ATLAS in 2010, corresponding to an integrated luminosity of $35.5\,\mathrm{pb}^{-1}$ is used in the analyses presented in this thesis.

5 Object identification and selection

The following sections describe object (τ leptons, muons, jets, electrons, transverse energy sum and missing transverse energy) reconstruction and identification algorithms at ATLAS [45].

For different parts of the analyses in this thesis, varying reconstruction and identification algorithms have been used. Due to changing recommendations from various ATLAS groups, this could not be be avoided. Furthermore, because reconstruction and identification algorithms are always subject to modifications and improvements, availability of some algorithms could not always be ensured.

5.1 τ jets

τ leptons can decay either leptonically or hadronically, with the latter process taking place about 65% of the time. Hadronically decaying τ leptons, so-called τ jets can feature one or more charged pions. Thus they leave one or more charged tracks. In contrast to QCD jets, the tracks are placed in a narrow cone, the track multiplicity is low, an energy deposition is placed in the calorimeter and isolation from the rest of the event is possible in the inner detector and calorimeter. Nevertheless, since the signature of τ jets is similar to those of QCD jets, a separate identification step after reconstruction is needed.

Reconstruction τ jet reconstruction is based on two different algorithms, one calorimeter-seeded and one track-seeded [46]. The calorimeter-based algorithm (TauRec) starts from topological calorimeter clusters to build τ candidates. These are required to have a minimum transverse momentum of $p_T > 10\,\mathrm{GeV}$. Track-based reconstruction (Tau1p3p) requires a high-quality seed track with minimum transverse momentum ($p_T > 6\,\mathrm{GeV}$). Combining both algorithms yields double-seeded τ candidates with a maximum distance in ΔR of 0.2. In this thesis, calorimeter-seeded τ leptons are required.

Identification τ jets are identified as such using rectangular cuts, a projective likelihood or a boosted decision tree. When the studies presented in this thesis were done, up to seven variables listed in Table 5.1 out of a large number of potential variables are used for identification. The selection of variables has already changed in current data [48]. Due to worse separation power of some variables because of pile-up, it will be necessary to employ variables more robust under pile-up. Hence the likelihood variables will change further. With these variables, a likelihood function and a boosted decision tree are built. Depending on the required signal efficiency these identified τ jets are classified as 'loose' ($\approx$70%),

Variable	Description
cluster mass	invariant mass of associated topological clusters
track mass	invariant mass of the track system
track radius	track width weighted with transverse momenta of all associated tracks $R_{track} = \frac{\Sigma_i^{\Delta R_i<0.2} p_{T,i} \Delta R_i}{\Sigma_i^{\Delta R_i<0.2} p_{T,i}}$
leading track momentum fraction	fraction of transverse momentum of leading track over transverse momentum of the τ candidate
electromagnetic radius	width in the EM calorimeter, weighted with transverse energy $R_{EM} = \frac{\Sigma_i^{\Delta R_i<0.4} E_{T,i}^{EM} \Delta R_i}{\Sigma_i^{\Delta R_i<0.4} E_{T,i}^{EM}}$
core energy fraction	fraction of transverse energy in $\Delta R < 0.1$ of the τ candidate
electromagnetic fraction	fraction of transverse energy of the τ candidate deposited in the EM calorimeter

Table 5.1: List of the τ variables used for identification with the likelihood method (all except core energy fraction) and boosted decision tree (all) in early 2010 data [46]

’medium’ (≈50%) or ’tight’ (≈30%). For better discrimination, identification is applied separately to bins of p_T and number of tracks. The three classifications are defined such that tight is a subset of medium, which itself is a subset of loose. Background efficiencies, defined as the number of τ candidates passing identification divided by all reconstructed τ candidates, corresponding to the three different selections for the likelihood identification are shown in Figure 5.1.

In Figure 5.2, the background and signal efficiencies from data and simulation are shown as a function of the transverse momentum for the three different selections using the cut-based identification.

Object selection In studies optimizing the embedding and signal selections (see chapter 7), a tight cut-based τ ID built on the track radius, the leading track momentum fraction and the electromagnetic radius, is required, corresponding to a selection efficiency of about 30%.

The likelihood identifier is required for τ jets in collision data. A τ jet with one associated track has to pass medium selection criteria, a 3-prong τ has to be identified as tight.

For embedded data, the likelihood identification did not work due to a software problem in the embedding package. Instead, τ jets are identified using truth information, which is available in embedded data because the τ jet is simulated and inserted into a collision data event. If the ΔR distance between a reconstructed τ and a truth τ with $p_T > 20\,\text{GeV}$ is less than 0.2, the τ jet is accepted in the embedded samples.

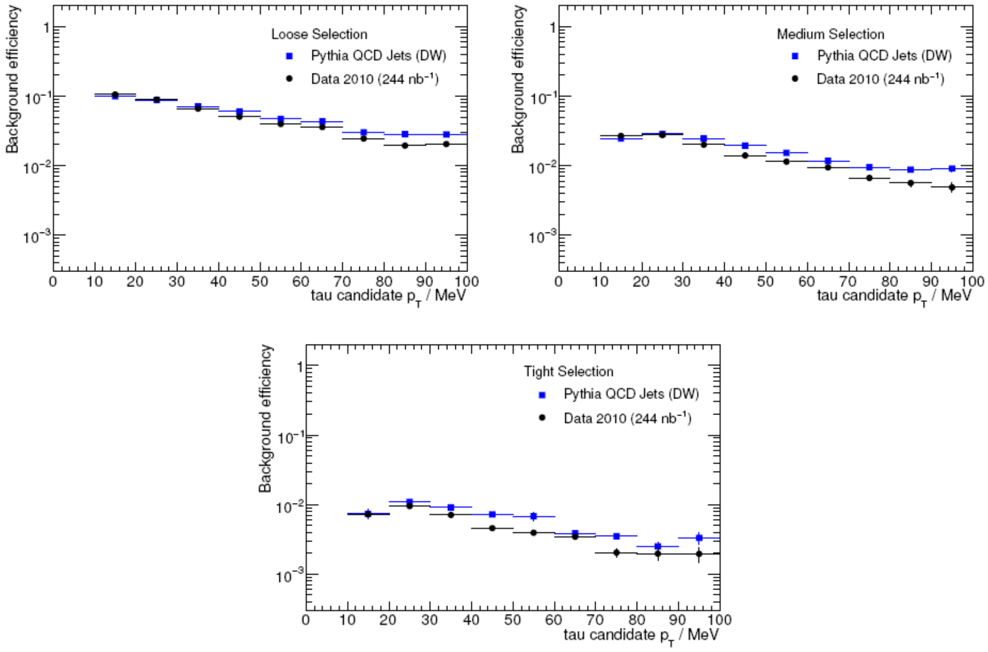

Figure 5.1: Background efficiency corresponding to the loose, medium and tight selection using a likelihood method as a function of the transverse momentum of the τ candidate [47].

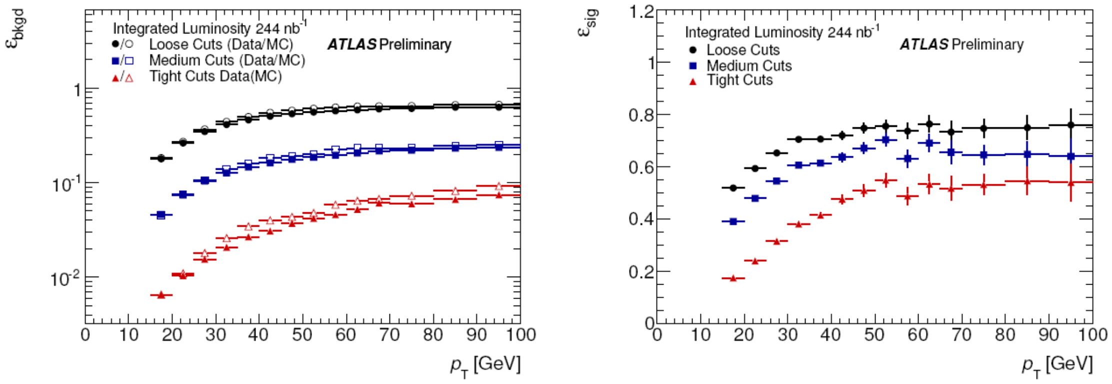

Figure 5.2: Signal and background efficiencies for loose, medium and tight selections using the cut-based identification [46]

5.2 Jets

Reconstruction and identification Jet reconstruction algorithms can be divided into two categories, cone types and sequential recombination types. Depending on the event topology one is interested in, different algorithms may be preferred [45]. Cone-type algorithms suffer from some problems (e.g. overlapping of cones, collinearity of seeds, energy deposits are spread wider than a single cone), wherefore other 'cone-like' and also 'non-cone-like' algorithms have been invented, not using fixed cone sizes. One such sequential recombination algorithm that yields cone-like jets without fixed cones is the anti-k$_\mathrm{T}$ algorithm [49]. Between particles or pseudojets one defines the distance d_{ij} and between a particle and the beam the distance d_{iB}.

$$\begin{aligned} d_{ij} &= min(k_{T\,i}^{2p}, k_{T\,j}^{2p}) \frac{\Delta_{ij}^2}{R^2} \\ d_{iB} &= k_{T\,i}^{2p} \end{aligned} \tag{5.1}$$

Here, Δ_{ij} is the distance between two entities i and j in the ϕ-y-plane, R is the radius, p is a parameter and k_T refers to the transverse momentum. Starting from a particle, the shortest distance of all d_{ij} and d_{iB} is identified: if it is a distance between particles, they are combined and if it is a distance to the beam, a jet is identified and the particle is removed from the list of particles. This is repeated until all particles are added to jets. In contrast to other sequential recombination algorithms, a negative power p appears in the definition of distance measures. The anti-k_T algorithm is used within ATLAS with different radius values of ΔR, within which particles are clustered.

Object selection The anti-k$_\mathrm{T}$ algorithm with ΔR=0.4 is used for reconstructing jets. Collision data events with jets that have E>0 GeV and fulfill the 'bad loose' criterion are rejected. So-called bad jets are due to e.g. hardware problems, beam conditions or cosmic-ray showers and not associated to real in-time energy deposits in the calorimeters [50]. Due to mis-measurement of the energy, it can happen that jets are assigned negative energies. The jets used are calibrated at the electromagnetic level.

5.3 b-Tagging

Identification b-Tagging describes the identification of jets that arise from the hadronization of b quarks. It is especially relevant for Higgs production channels. Due to the long lifetime of hadrons with b quarks ($c\tau \approx 450\mu$m), the decay vertices of b-hadrons are well separated from the primary vertices. Furthermore, the decay products of b-hadrons will have predominantly high transverse momentum because of the high b quark mass and hard fragmentation of b-hadrons. Algorithms identifying b jets utilize these properties. They rely e.g. on the reconstruction of secondary vertices (SV), track impact parameter measurements (IP) or track counting. For the latter, a jet is tagged as b jet if at least some tracks with large impact parameters are identified.

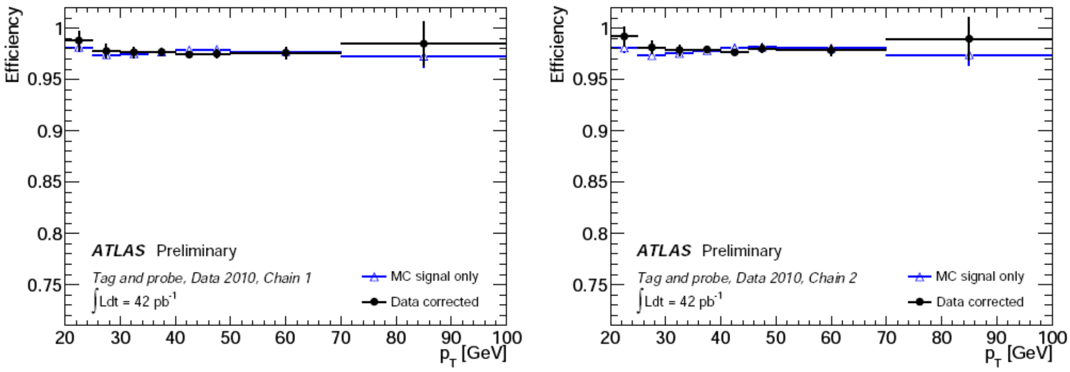

Figure 5.3: Reconstruction efficiencies for combined STACO muons (chain 1) and Muid muons (chain 2) as a function of p_T. Efficiencies are measured in a $Z \rightarrow \mu\mu$ sample, where backgrounds estimated using Monte Carlo simulation have been subtracted [52].

Object selection Different b-tagging algorithms were used in the analyses presented here. Either a combination of secondary vertex and impact parameter algorithm was employed, (SV1+IP3D, used for optimizing the embedding selection, see chapter 7) or a secondary vertex only algorithm (SV0, used for background estimations). The cut values were chosen for an efficiency of 50% and changed according to updated recommendations. Applied to a $t\bar{t}$ sample, a purity of about 93% is reached with a cut on SV0>5.85, yielding a purity of about 50% [51]. The mis-tag rate on light jets is about 0.4%, while that for τ jets is about 2% and for charm jets about 10%.

5.4 Muons

Identification For muons, different identification strategies are available. Because more than one algorithm exists for each of these strategies, several muon candidate collections are available. Two of these are STACO and Muid. They each provide three algorithms to reconstruct standalone, combined and tagged muons. To reconstruct standalone muons, tracks in the muon spectrometer are extrapolated to the beam line. For combined muons, standalone muons are matched to tracks in the inner detector and the two measurements are combined. To get tagged muons, tracks in the inner detector are extrapolated to the muon spectrometer where nearby hits are searched. As for other objects, different tightness for the identification criteria is available. The reconstruction efficiency for both STACO and Muid muons is shown in Figure 5.3.

Object selection Tight combined Muid muons are used in collision data. Only STACO muons are available in embedded data, hence these are used. Muons are required to have high transverse momenta ($p_T > 20\,\text{GeV}$), be isolated (sum of transverse energy deposits in calorimeter cells <10 GeV in a hollow cone with $\Delta R = 0.3$ around the muon) and be detected in a pseudorapidity range $|\eta| < 2.5$. In the signal selection, a veto is applied to events containing muons fulfilling the above mentioned requirements. For the control sample that the embedding is applied to events that contain exactly one muon fulfilling the above mentioned requirements are selected.

5.5 Electrons

Identification Electrons in ATLAS are identified using cut-based reconstruction algorithms. These can be either cluster-seeded or track-seeded or a combination of both. The cluster-based algorithm starts from reconstructed clusters in the electromagnetic calorimeter, which are matched to tracks in the inner detector. It is optimized for electrons with high transverse momenta. Low-energetic and non-isolated electrons are identified more efficiently with a track-based algorithm. Here, tracks in the inner detector are matched to energy depositions in the electromagnetic calorimeter. For electrons in the forward direction, with $2.5 < |\eta| < 4.9$, no track matching is performed. Information for identification variables is taken from the calorimeter only. To select electrons, a variable is given that specifies the algorithm it was reconstructed with. As for other objects, different cut values on the identification variables can be required, leading to 'loose', 'medium' and 'tight' identification of electrons. As soon as more data are available, it is planned to move the identification algorithms from cut-based to other, more sophisticated techniques such as likelihood discriminants, neural networks or boosted decision trees.

Object selection Cluster-seeded or cluster- and track-seeded electrons which are not located in the crack region of the detector ($1.37 < |\eta| < 1.52$) and at $|\eta| < 2.47$ are considered. They have to be isolated (sum of transverse energy deposits in calorimeter cells <10 GeV in a hollow cone with $\Delta R = 0.2$ around the electron + $0.023 \cdot E_T(\text{electron})$ [GeV]<4 GeV) and have a transverse momentum of at least 10 GeV. Events containing such electrons are vetoed.

5.6 Missing transverse energy E_T^{miss}

Reconstruction Assuming energy conservation in the transverse plane, the vectorially added transverse energies of all detectable particles in an event should add up to zero. Since calorimeters have finite resolution and coverage and more importantly, since particles like neutrinos do not leave any energy or trace in the detector, a certain amount of transverse energy is 'missing' in events. This is called missing transverse energy or E_T^{miss}. It is defined as

$$E_T^{miss} = \sqrt{(E_x^{miss})^2 + (E_y^{miss})^2}. \tag{5.2}$$

The E_x and E_y term each consist of one term accounting for energy depositions in the calorimeters, one for muons and and one for energy lost in the cryostats [53].

In the calorimeter, topological clusters (topoclusters) are built from cells in order to reduce noise: cells not neighboring a cluster are identified as noisy and removed from the event. Different calibrations schemes are available, either weighting cells locally or glob-

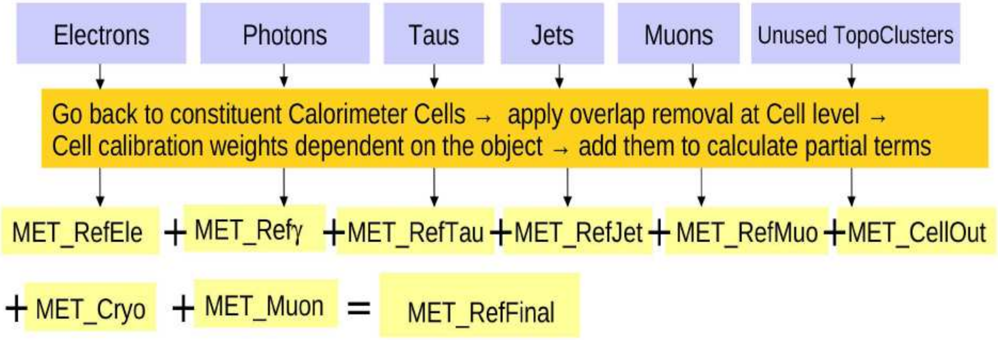

Figure 5.4: Illustration of how transverse missing energy is calculated using the refined calibrations scheme [53].

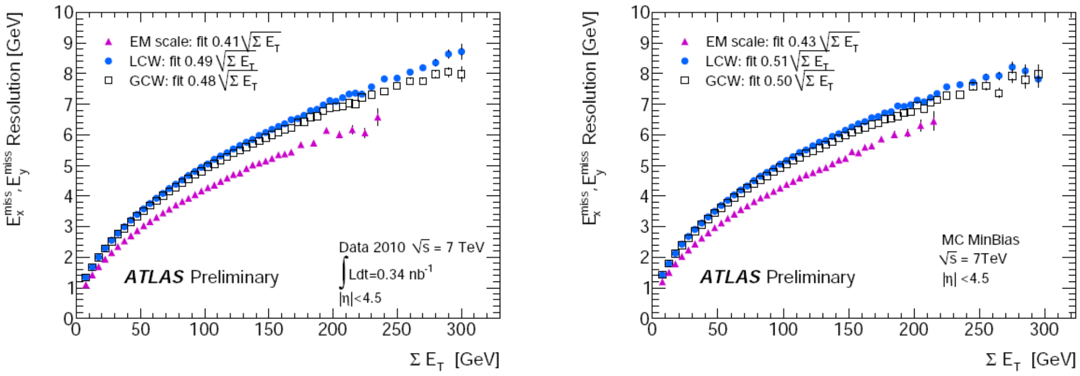

Figure 5.5: Resolution of $E_{x,y}^{miss}$, depending on the transverse energy sum ΣE_T in data (left) and simulation (right) for different calibrations. Resolution using the refined calibration is very close to that of the local cell weighting scheme, LCW [53].

ally, or using a ’refined’ calibration. This refined procedure is based on reconstructed objects and illustrated schematically in Figure 5.4. Cells belonging to different objects (electrons, jets, muons, ...) are calibrated separately. The same applies to cells from topoclusters that could not be associated to any object.

The muons term is based on the momenta of muons. It is calculated differently, depending on whether the muon is isolated or close to a jet. If the muon is isolated, the measurements from the muon spectrometer and inner detector are combined. The energy deposited by a muon in the calorimeters is then not added to the calorimeter term. If the muon is not isolated, it is not possible to separate the energy deposited in the calorimeter by the muon or by a near-by jet. Thus the measurement from the muon spectrometer is used exclusively. Only in the case of large discrepancies between the measurement from the spectrometer only and the combined measurement a combination is used, with parametrized energy deposits in the calorimeter subtracted.

In Figure 5.5, the resolution of the missing transverse energy depending on the transverse energy sum is shown for data and simulation.

Selection In all studies performed, a missing transverse energy variable based on the refined calibration scheme is used.

5.7 Transverse energy sum ΣE_T

Reconstruction Adding energies of an event measured in the calorimeters as scalars yields the total transverse energy of the event ΣE_T. Just as for the missing transverse energy, different algorithms are available to calculate ΣE_T, using different calibration schemes.

Selection A transverse energy sum variable using the refined calibration described above was used in the studies for optimizing the embedding selection. For optimizing the signal selection and in studies containing collision data, the ΣE_T variable was built from τ jets, jets and missing transverse energy that passed standard selection criteria described above.

5.8 Overlap removal

Jets are rejected if they overlap within $\Delta R < 0.2$ with τ jets. For the embedding selection, events that contain high-energetic jets overlapping with muons are rejected. The specific criteria are subject to the optimization of the selection and explicitly named in chapter 7.

6 Signal selection

6.1 Motivation

To discover New Physics (or to exclude it), an event selection has to be applied to data that filters out events with the wanted topology and rejects background processes as well as possible. Here, the signal process consists of a charged Higgs boson decaying to a τ and a neutrino, a W boson decaying hadronically and two b quarks resulting from the decay $t \rightarrow H^{+}b/Wb$, thus events containing these objects are to be selected.

In the following, the selection to find charged Higgs bosons with the above-mentioned decays is optimized using simulation. The main signal selection is optimized using TMVA (Toolkit for Multivariate Data Analysis with ROOT) [54]. For easier and faster usage, the samples are preselected.

Background processes considered for this study are Standard Model $t\bar{t}$ decays, W+jets, single top and QCD events.

The selection is applied to $35.5\,\mathrm{pb}^{-1}$ of data taken by ATLAS in 2010 in chapter 7.

6.2 Preselection

In the preselection, the kinematics and final state products of signal processes are exploited in a very general way, e.g. imposing minimum requirements on the transverse momenta of jets and the τ and requiring low values of the missing transverse energy.

The requirements imposed in this preselection include

- a combined tau and E_T^{miss} trigger with $p_T(\tau) > 16\,\mathrm{GeV}$ and $E_T^{miss} > 20\,\mathrm{GeV}$
- one tau lepton with $p_T > 15\,\mathrm{GeV}$ and $|\eta| < 2.5$ that passes tight identification cuts
- at least four jets with $p_T > 15\,\mathrm{GeV}$ and $|\eta| < 5$ that do not overlap ($\Delta R < 0.2$) with a tau
- missing transverse energy greater than 20 GeV
- a veto on events containing any isolated electrons (E_T of calorimeter cells in a hollow cone around the electron with radius $R = 0.2$<4 GeV$+0.023 \cdot E_T(\text{electron})$) with $p_T > 10\,\mathrm{GeV}$ outside the crack regions of the detector located at $1.37 < |\eta| < 1.52$
- a veto on events containing any isolated muons (p_T of calorimeter cells in a hollow cone around the muon with radius $R = 0.3$<4 GeV, less than 4 tracks in a cone with radius $R < 0.3$) with $p_T > 10\,\mathrm{GeV}$ and $|\eta| < 2.5$

A signal selection efficiency of about 10% was achieved for the preselection. Z+jets events have not been taken into account because their contribution to the background is

$H+$	$t\bar{t}$	W+jets	QCD	single top
59.4±7.7	188.6±13.7	156.4±12.5	42548.5±206.3	16.0 ± 4.0

Table 6.1: Events expected from MC for an integrated luminosity of 35.5 pb^{-1} after preselection. Uncertainties are statistical only.

negligible. After preselection, the background is still dominated by QCD events. Since so far events containing high-momentum objects have been selected, this is expected. The topology of the signal process has not been exploited, but this will be done in the final selection. Events expected to pass the preselection for an integrated luminosity of 35.5 pb^{-1} are summarized in Table 6.1.

6.3 Main selection

In the main selection, the exploiting of the topology of signal events is much more pronounced than in the preselection. Cuts on different objects are tightened for a better rejection of background processes. Due to e.g. $m_{H^+} > m_W$, the τ from the charged Higgs boson decay is expected to have on average a higher transverse momentum than a τ resulting from a W boson decay would have. Hence, the cut on $p_T(\tau)$ can be set to a higher value. The same applies e.g. to the missing transverse energy: in signal events this quantity is expected to be greater than in background processes and the cut can be tightened correspondingly.

To find the optimal selection cut values, TMVA is used. TMVA optimizes cuts for the best background rejection at fixed signal efficiencies. The signal and background samples are each weighted with the corresponding cross sections.

The cuts to be optimized are given to TMVA, possibly with certain specific constraints such as minimum values of the variables. Different combinations out of a variety of variables have been passed to TMVA. The cuts on the following variables are considered:

- the transverse energy sum of the events, ΣE_T: with at least four jets and one τ coming from the $t\bar{t}$ decay, a large transverse energy sum is expected in signal events
- the missing transverse energy, E_T^{miss}: due to the neutrino coming from the H^+ decay, which is not detected, a significant missing transverse energy is expected
- the missing transverse energy significance, that is E_T^{miss}Significance $= E_T^{miss}/\sqrt{\Sigma E_T}$ (the significance of E_T^{miss} is $E_T^{miss}/\delta_{E_T^{miss}}$, where δE_T^{miss} is the uncertainty in E_T due to energy deposits in dead material and proportional to $\sqrt{\Sigma E_T}$): this cut has been shown to be better suited to suppress especially QCD background without losing much signal in contrast to simply increasing the E_T^{miss} or ΣE_T cuts
- the transverse momentum of the leading jet, p_T(jet): the transverse momentum spectrum in signal events may be different than to that in background events
- the transverse momentum of the sub-leading jet, p_T(jet)
- the transverse momentum of the τ, $p_T(\tau)$

	H^+	$t\bar{t}$	W+jets	QCD	single top
cut 1	49.2±7.0	160.6±12.7	101.6±10.1	28731.0±169.5	11.2±3.3
cut 2	48.9±7.0	160.1±12.7	98.0±9.9	28564.0±169.0	11.2±3.3
cut 3	30.0±5.5	88.3 ±9.4	49.8 ±7.1	10484.9±102.4	6.3±2.5
cut 4	15.9±4.0	35.5 ±6.0	24.2 ±4.9	112.2 ±10.6	2.5±1.6
cut 5	10.7±3.3	24.6 ±5.0	1.7 ±1.3	34.5 ±5.9	1.5±1.2
cut 6	4.7 ±2.2	9.5 ±3.1	0.9 ±0.9	2.9 ± 1.7	0.6±0.8
cut 7	3.9 ±2.0	8.1 ±2.8	0.6 ±0.8	0.7 ± 0.8	0.5±0.7

Table 6.2: Cutflow for the TMVA-optimized selection. Event numbers are scaled to expected events in 35.5pb^{-1} and uncertainties are statistical only. For the signal, $m_{H^+} = 130$ GeV and $\tan\beta = 35$ are assumed.

- the highest b-jet tagger weight, $SV0$: several working points referring to different efficiencies of the b-tagger may be used
- the top quark mass m_{jjb} of the top quark decaying $t \to Wb \to qqb$: with two jets and the jet with the highest b-weight it should be possible to reconstruct the nominal top quark mass within a certain mass window
- the angle $\Delta\phi$ between the τ and E_T^{miss}: if the mass of the charged Higgs boson is greater than that of a W boson, the angle $\Delta\phi$ between the decay products of the H^+ can be smaller than that of the τ and neutrino from the W boson decay because of a higher transverse momentum of the τ

A signal efficiency of 3% resulting from the TMVA optimization was finally considered. The corresponding cuts yield good background suppression especially for W+jets and QCD backgrounds. The final signal selection cuts resulting for this are

- cut 0: a combined τ and E_T^{miss} trigger
- cut 1: transverse energy sum: $\Sigma E_T > 300\,\text{GeV}$
- cut 2: transverse momentum of leading jet: $p_T(\text{jet}) > 40\,\text{GeV}$
- cut 3: transverse momentum of tau: $p_T(\tau) > 35\,\text{GeV}$
- cut 4: missing transverse energy: $E_T^{miss} > 70\,\text{GeV}$
- cut 5: b-tagger weight: SV0>5.72, yielding an efficiency of 50%
- cut 6: missing transverse energy significance: $E_T^{miss}\text{Significance} > 5\,\sqrt{\text{GeV}}$
- cut 7: top quark mass window: $145\,\text{GeV} < m_{jjb} < 235\,\text{GeV}$

The cutflow for these cuts (without the trigger requirement) for signal and important backgrounds is summarized in Table 6.2. The trigger requirement is not an optimization variable; in collision data the lowest unprescaled $\tau + E_T^{miss}$ trigger is used. When optimizing the signal selection, it was not foreseeable which trigger this would be in the end.

When applying the signal selection to collision data in chapter 7, events are not prefiltered and thus a veto on events containing high-energetic, isolated muons and electrons as in the preselection is added to the signal selection cuts.

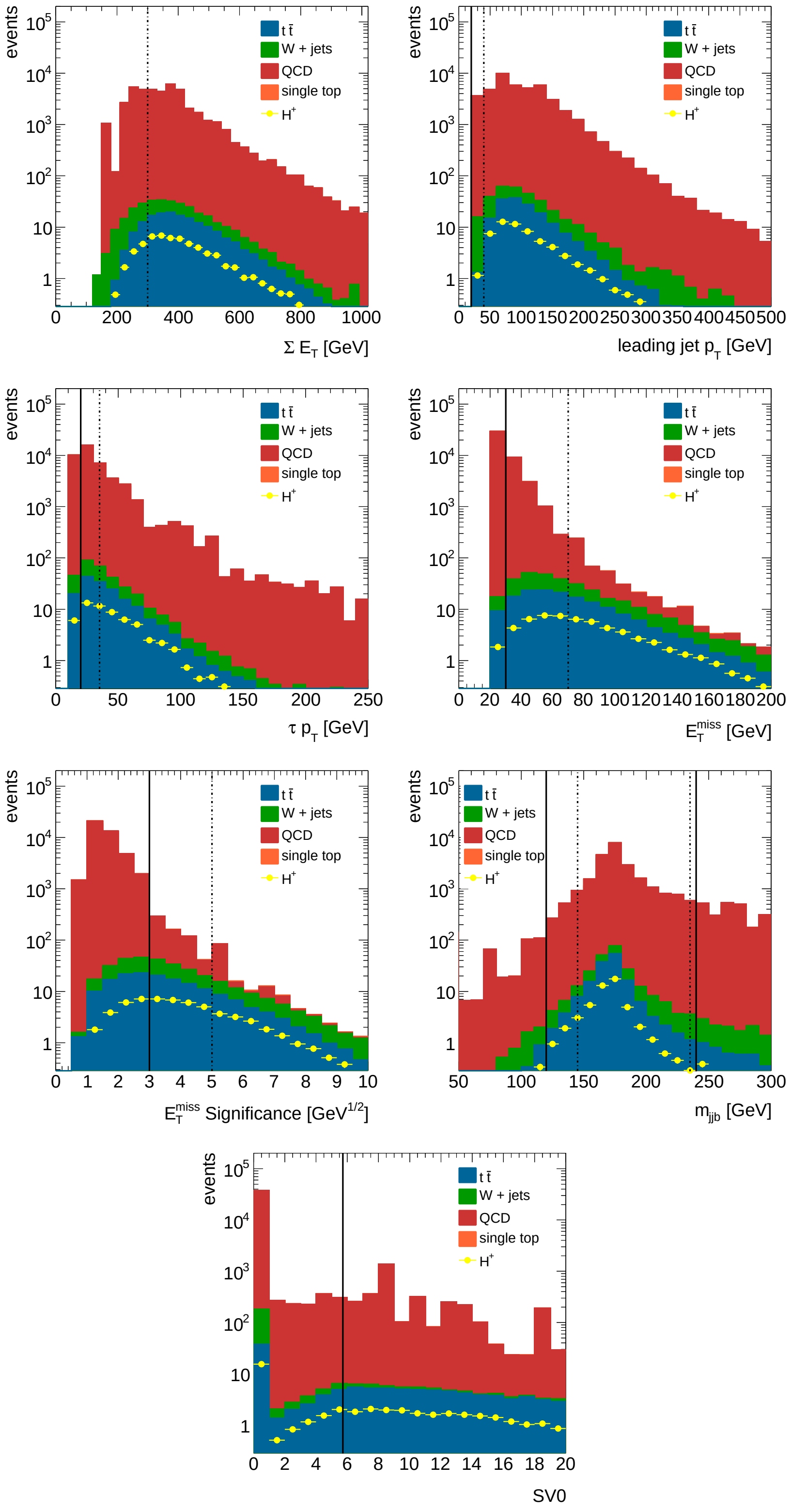

Figure 6.1: Distribution of variables after preselection. The background contributions are stacked, a hypothetical signal assuming $m_{H^+} = 130\,\mathrm{GeV}$ and $\tan\beta = 35$ is superimposed. Signal selection cut values of the optimized selection are indicated as dash-dotted lines. Baseline cuts are shown in solid lines. Events are normalized to $35.5\,\mathrm{pb}^{-1}$.

After applying the TMVA-optimized signal selection, the background is dominated by $t\bar{t}$ processes with 8.1±2.8 events. All other backgrounds are well reduced with W+jets, QCD and single top processes resulting in only 0.6 ± 0.8, 0.7 ± 0.8 and 0.5 ± 0.7 events, respectively. From charged Higgs processes, 3.9 ± 2.0 events are expected.

The cut on E_T^{miss}Significance is very effective in reducing especially the QCD background as expected. W+jets events are harder to suppress because of more similarities to the signal compared QCD and signal. The same applies to the $t\bar{t}$ background, as discussed in chapter 4.

Preselected distributions with the optimized signal selection cut values and loosened cut values corresponding to the baseline selection (see below) indicated are shown in Figure 6.1. The transverse mass calculated from the momenta of the τ lepton and the missing transverse energy is used as discriminating variable. For background processes with two W bosons coming from the $t\bar{t}$ decay, this corresponds to the transverse mass of a W decaying to a τ lepton and a neutrino while for signal processes it corresponds to the transverse mass of the H^+. It is defined as

$$m_T = \sqrt{2 \cdot p_T(\tau) E_T^{miss}(1 - \cos \Delta\phi)}. \tag{6.1}$$

Here, $\Delta\phi$ is the angle between the missing momentum and the τ jet in the transverse plane. The m_T distribution after the TMVA-optimized signal selection is shown in Figure 6.2. If the mass of the charged Higgs boson is greater than the W boson mass, the distribution of m_T is expected not to drop at the W mass, but at m_{H^+} as can be clearly seen in Figure 6.2.

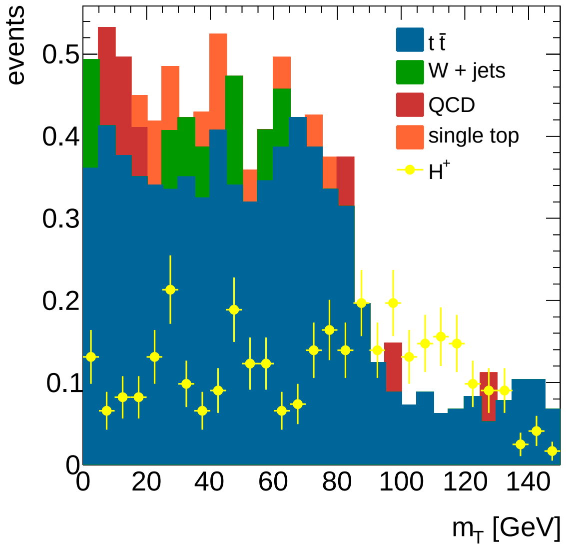

Figure 6.2: Distribution of the transverse mass after TMVA-optimized signal selection. Shown are events expected in $35.5\,\mathrm{pb}^{-1}$. Background contributions are stacked, hypothetical signal assuming $m_{H^+} = 130\,\mathrm{GeV}$ and $\tan\beta = 35$ is superimposed.

The TMVA-optimized selection has to be loosened slightly when applied to data taken by

	H^+	$t\bar{t}$	W+jets	QCD	single top
(cut 1)	59.4±7.7	188.6±13.7	156.4±12.5	42548.5±206.3	16.0±4.0
cut 2	59.4±7.7	188.6±13.7	156.4±12.5	42548.5±206.3	16.0±4.0
cut 3	53.4±7.3	166.3±12.9	131.0±11.4	32539.3±180.4	14.0±3.7
cut 4	51.8±7.2	156.6±12.5	124.0±11.1	9726.5 ±98.6	12.4±3.5
cut 5	33.7±5.8	109.5 ±10.5	6.8 ±2.6	1058.6 ±32.5	7.6 ±2.8
cut 6	23.2±4.8	63.1 ±7.9	4.2 ±2.1	161.0 ±12.7	4.5 ±2.1
cut 7	20.0±4.5	56.4 ±7.5	3.1 ±1.8	89.2 ±9.4	3.7 ±1.9

Table 6.3: Cutflow for the baseline signal selection. Event numbers are scaled to expected events in 35.5 pb^{-1} and uncertainties are statistical only. Compared to Table 6.2, cut 1 has been dropped and cuts 2, 3, 4, and 6 have been set to lower values and the mass window in cut 7 has been widened. The p_T requirement is applied to the leading jet only. For the signal, $m_{H^+} = 130\,\mathrm{GeV}$ and $\tan\beta = 35$ are assumed.

ATLAS in 2010 because otherwise event yields after the final selection are too low. With an expectation of scarcely 10 background events, the results after the TMVA-optimized selection are subject to statistical fluctuations, leading to not very reliable or significant results.

Some of the cut values from the TMVA-optimized selection are thus altered or dropped:

- no cut on ΣE_T: because of the cut on E_T^{miss} and E_T^{miss} Significance, no additional ΣE_T cut is necessary
- E_T^{miss} Significance: the cut value is lowered to $3\sqrt{\mathrm{GeV}}$
- E_T^{miss}: the cut values is lowered to 30 GeV
- p_T of leading jet: lowered to 20 GeV, but four jets with this transverse momentum are required
- p_T of τ jet: lowered to 20 GeV
- top quark mass window: $120\,\mathrm{GeV} < m_{jjb} < 240\,\mathrm{GeV}$

Expected events in 35.5 pb^{-1} for this loosened selection, called 'baseline' in the following, are summarized in Table 6.3. Applying the baseline selection, the background is no longer dominated by $t\bar{t}$ but by QCD events, with 56.3 ± 7.5 $t\bar{t}$ and 89.2 ± 9.4 QCD events. Single top and W+jets processes are still well suppressed, contributing 3.1 ± 1.8 and 3.7 ± 1.9 events, respectively. With 20.0 ± 4.5 about five times as much signal events as before pass the selection now, compared to the TMVA-optimized cuts.

The S/B ratio drops from 0.39 for the TMVA-optimized selection to 0.13 for the baseline selection.

The m_T distribution after loose signal selection is shown in Figure 6.3.

When applied to collision data, the cut on the b-tagger weight is set to 5.85 instead of 5.72 following recommendations.

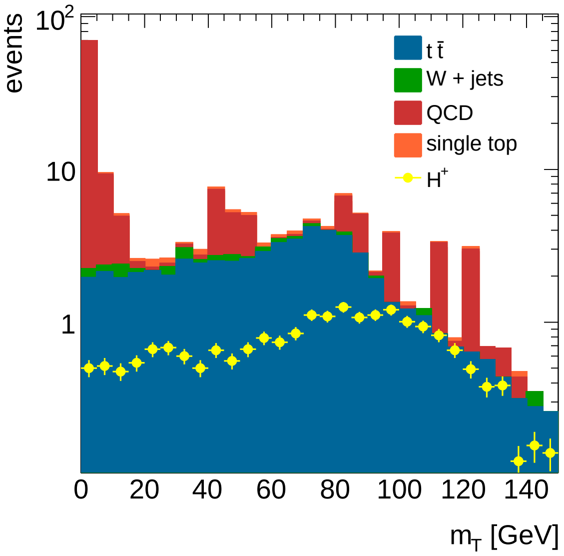

Figure 6.3: Distribution of the transverse mass after baseline signal selection. Shown are events expected in $35.5\,\text{pb}^{-1}$. Background contributions are stacked, hypothetical signal assuming $m_{H^+} = 130\,\text{GeV}$ and $\tan\beta = 35$ is superimposed.

7 Background estimation

7.1 Approach to data-driven background estimation

An accurate understanding of background processes is crucial for making discoveries or setting valid limits on hypothetical New Physics processes. Since pile-up conditions, underlying event, trigger efficiencies and the detector response in general are not always well-modeled in simulation and associated with some degree of uncertainty [45], data-driven background estimates are needed. By not relying on Monte Carlo simulation but rather taking most of the information directly from data, problems in the modeling can be avoided and systematic uncertainties can be reduced.

In the following, different contributions to the backgrounds in charged Higgs boson searches are estimated using data-driven methods. Events that contain true τ jets are studied and estimated using the so-called embedding method. The optimization and validation of the embedding technique is performed in the context of this thesis. Estimating the background contribution with the embedding method, everything but the τ jet is taken from collision data. If electrons, muons or jets in events are wrongly identified as τ jets, their contribution are estimated using so-called fake rates. A fake rate is determined by the number of objects of a certain type wrongly identified as τ jets divided by all objects of that type that are reconstructed as τ jets (see chapter 5).

$$\text{fake rate} = \frac{\text{No. of objects } (e, \mu, jet) \text{ identified as } \tau}{\text{No. of objects } (e, \mu, jet) \text{ reconstructed as } \tau} \tag{7.1}$$

For background estimations using fake rates, everything but the fake rate itself is taken from simulation. The contribution from QCD multi-jet background is estimated based on a data-driven control sample. Only very little input is taken from Monte Carlo simulation.

Finally, methods and results from estimating all contributions to charged Higgs boson backgrounds are summarized. The results from the data-driven background estimates are merged and compared to collision data.

The methods to estimate the fake-rates and the QCD contribution and corresponding results are reported for completeness [55, 56].

7.2 Estimating the background with true τ leptons using the embedding method

Standard Model $t\bar{t}$ events decaying to a τ jet, 4 jets and missing transverse energy are an irreducible and very important background to the signal channel investigated in this thesis

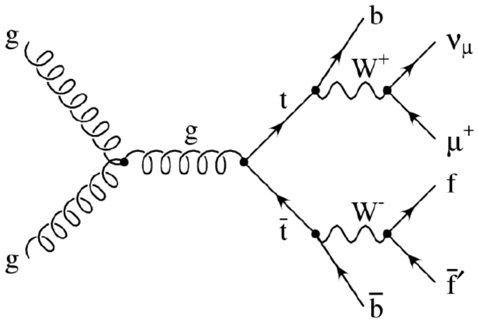

Figure 7.1: Leading-order Feynman diagram of the Standard Model process wanted for the embedding. The final state of the W boson not decaying to a muon includes two quarks.

(see chapter 4) once the baseline selection is applied. It is therefore impossible to select background events of this topology without selecting signal events as well. The goal of the analysis presented here, however, is to predict the shape and normalization of the m_T distribution for events featuring exactly the above mentioned objects. This is done using an embedding technique. Compared to background estimations based on Monte Carlo simulation, this method has the advantage that everything but the τ jet, including pile-up and the underlying event, is taken from collision data.

To apply the embedding, events are collected from data that show an identical topology but are free of signal. The branching ratio $H^+ \to \mu\nu$ is negligibly small. Thus in events of the type $t\bar{t} \to W^b bW^-\bar{b} \to \mu\nu bqqb$, very little signal contribution is expected.

The embedding technique takes advantage of such events with a topology and kinematics similar to those of the channel that is investigated but including different final state particles, i. e. a muon instead of a hadronic τ decay. The final state particle not wanted in the analysis (here a muon) is removed from the event and replaced by a simulated one (here a hadronically decaying τ), hence leading to the process needed for background estimation while guaranteeing that the sample is signal-free.

Embedding has been successfully applied to $Z \to \mu\mu$ events to estimate the $Z \to \tau\tau$ background in $H \to \tau\tau$ searches [57] and first studies in charged Higgs boson searches have been performed [58].

In the following, the embedding selection to collect events featuring a muon, four jets and missing transverse energy is optimized. The dominating process for this is shown in Figure 7.1. Embedded $t\bar{t}$ Monte Carlo simulation samples are compared to reference $t\bar{t}$ Monte Carlo simulation samples. In the following, reference samples mean that the embedding selection has been applied requiring a τ instead of a muon. Embedded collision data taken by ATLAS in 2010 are then compared to reference Monte Carlo simulation including $t\bar{t}$, single top, W+jets and QCD processes. Systematic uncertainties due to the embedding are studied.

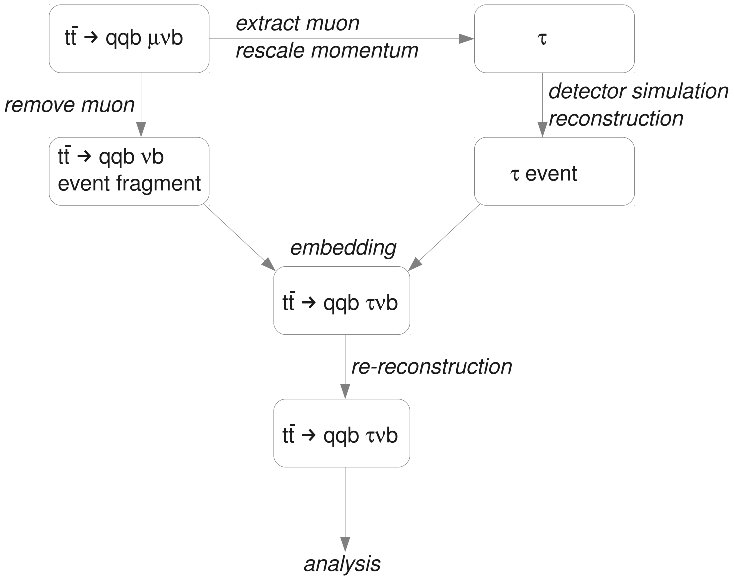

Figure 7.2: Schematic illustration of the embedding method, adapted from [58]

7.2.1 Embedding technique

The method can be divided roughly into four separate steps, illustrated schematically in Figure 7.2 [57, 58, 60]: decay identification, rescaling and manipulation of the event, merging and reconstruction.

In the studies presented here, embedding takes place on cell level in the detector. That is, the detector response (i.e. individual cells) of a muon is replaced by that of a τ lepton instead of replacing reconstructed objects. The replacement takes place in a small inner cone (here of radius $\Delta R = 0.1$) around the original muon. Calorimeter cell energy depositions in an area between this inner cone and a wider outer cone are added to the cells from the original event instead of replacing them, as is illustrated in Fig. 7.3. Since E_T^{miss} is calculated on cell-level in ATLAS, having to calculate or correct this quantity manually is avoided.

Decay identification As first step, events are identified to which the embedding will be applied. The events should satisfy certain criteria, such as containing a high energetic muon, four jets, a minimum total transverse energy and minimum missing transverse energy to account for the neutrino, that describe the final state well. A good purity is wanted in the embedded samples, such that the criteria describe the process shown in Figure 7.1 as well as possible.

The reconstructed vertex the muon points to is used as vertex position.

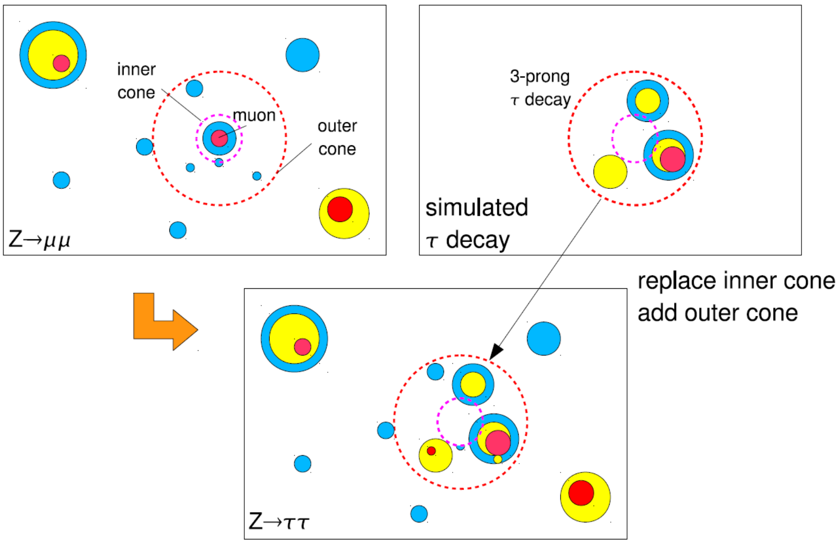

Figure 7.3: Schematic illustration of inner and outer cones around original muon/simulated τ and adding/replacement of energy depositions. The rectangle represents an area in the calorimeter. Full circles show energy depositions, where blue represents less and red more deposited energy compared to yellow. The dashed circles represent the inner and outer cones. Although this illustration shows a $Z \to \mu\mu$ event, the mechanism is the same for $W \to \mu\nu$ as used in this thesis. The muon in this figure is replaced by a τ jet with three charged tracks (3-prong) [60].

Rescaling and manipulation In the selected events, the muon is extracted and its momentum is rescaled to account for the higher τ lepton mass.

$$\vec{p}_\tau = \frac{\sqrt{E_\mu^2 - m_\tau^2}}{|\vec{p}_\mu|} \cdot \vec{p}_\mu$$

The decay of the rescaled τ is handled by TAUOLA, and PHOTOS is used to generate final state radiation. An event record of the τ decay is produced and fed into a realistic ATLAS detector simulation. The τ lepton then gets digitized and reconstructed. Calorimeter noise simulation or vertex smearing are not applied, following recommendations [61].

Merging In the first step of the actual embedding, the muons used as input for the τ leptons are identified and linked to the decay products of the τ. Since sometimes TAUOLA adds photon radiation in a decay, the four-vectors of the τ leptons can be altered, leading to different positions of the original muon and the τ.

In a second step, the tracks of the original muon in the muon spectrometer and inner detector are removed and those from the simulated τ decay are added. Track segments in a cone around the original muon in the muon spectrometer are also removed and replaced by simulated track segments in the same cone. Calorimeter cells in the inner cone around the former muon and tracks associated to it are replaced by those of the simulated τ decay products. Thus the original muon is completely removed from the event.

The final step consists of merging the event fragment and the simulated τ in the calorimeter. Energy depositions in a small inner cone around the muon are removed. In a larger cone ('outer cone') around the muon, the energy depositions in the calorimeter cells from the simulated τ decay are added to the original event.

Reconstruction Finally, some of the ATLAS reconstruction algorithms are run on the merged events to reconstruct higher level objects such as leptons, jets, τ jets and missing transverse energy.

7.2.2 Embedding parameters

To adjust the embedding method to the different implementations possible, flags can be set. Some parameters concern the kind of decay the embedding is run on, while others determine e.g. the cone size around the muon in which tracks and calorimeter cell energy depositions are replaced or added. Important parameters are:

Muon Identification Algorithm: Several muon collections can be used.

Jet Identification Algorithm: Different jet algorithms are available and can be used for reconstructing jets.

E_T^{miss} Algorithm: As for muons and jets, several algorithms are available to calculate missing transverse energy.

Calorimeter noise: Noise in the calorimeter in the digitization step, switched on or off.

CopyAllSimTracks: If this flag is set true, all simulated tracks are added to the original event.

UseOuterCone: If this flag is set true, cells in the outer cone are added.

MaxDRMuonToTruthTau: Maximum distance in R between the original muon and the truth τ (see explanation to 'Merging' step).

NumMuonsToReplace: Depending on the selected events, either one or two muons have to be replaced.

TauDecayMode: τ leptons can decay hadronically, forming jets, or leptonically to electrons or muons.

TauCone: Cells in $\Delta R <$TauCone are replaced, used for hadronically decaying τ leptons

TauOuterCone: Cells in TauCone$<\Delta R<$TauOuterCone are added to the event, used for hadronically decaying τ leptons

The settings used in the studies presented are summarized in Table 7.1.

Muon Identification Algorithm	STACO
Jet Identification Algorithm	AntiKt4TopoEM [1]
Missing ET Algorithm	MET_RefFinal [2]
Calorimeter noise	off
CopyAllSimTracks	true
UseOuterCone	true
MaxDRMuonToTruthTau	0.1
NumMuonsToReplace	1
TauDecayMode	had
TauCone	0.1
TauOuterCone	0.45

[1] anti-k_T algorithm with $\Delta R < 0.4$, calibrated at the electromagnetic scale

[2] refined E_T^{miss} calculation

Table 7.1: Parameter settings used in the Embedding. The settings for parameters that are not decay-specific follow recommendations [61].

7.2.3 Event selection and cut optimization

Starting off with the event selection proposed in ref. [59] for the muon + jets channel, the cuts have been optimized further. Since in 2009 it was still expected that the LHC would run at a center-of-mass energy of $\sqrt{s} = 14$ TeV, some of the cut values are quite tight for current conditions at a center-of-mass energy of $\sqrt{s} = 7$ TeV. Events containing the decays $t\bar{t} \to bWbW \to b\mu\nu_\mu bqq$, which can be identified using Monte Carlo simulation truth information, are treated as 'signal' for the embedding, since these are the processes wanted. All other $t\bar{t}$ channels with at least one lepton are called 'background' or 'other' in the following. The cuts for the event selection have been optimized on simulation event samples, considering the $t\bar{t}$, W + jets, Z + jets and $b\bar{b}$ processes (see chapter 4).

The selection presented in [59] requires events to pass the following criteria:

- one isolated (less than 10 GeV deposited in calorimeter cells in a hollow cone with $\Delta R < 0.2$ around the muon) muon with a high transverse momentum (p_T>20 GeV) is found
- the transverse energy sum has to be greater than 250 GeV
- two jets with transverse momenta above 40 GeV have to be present
- at least one of these high-momentum jets has to have a b-tag with JetWeight (combination of secondary vertex and impact parameter algorithms) >3
- the transverse mass of two additional jets with transverse momenta greater than 40 GeV lies within 20 GeV of the nominal W mass
- there are no muons with p_T>20 GeV within ΔR<0.4 of jets with p_T>20 GeV
- missing transverse energy of at least 40 GeV
- events are rejected if isolated (less then 20 GeV deposited in calorimeter cells in a hollow cone with $\Delta R < 0.3$ around the electron) electrons with transverse momenta

greater than 20 GeV are found

This selection filters out events with the required topology: one W is expected to decay to a muon and a neutrino, the other W decays hadronically. From the decay of the top-quark pair there are be two b jets present. Overall, four jets with high transverse momenta should be present. Since no electrons are expected, a veto is applied to events containing these. With four jets and the muon, the overall transverse energy of the events should exceed a certain value.

When applying these cuts to 7 TeV samples, a signal selection efficiency of only 6.9% is reached, compared to 8.6% in [59]. The signal purity improves a little, from 74.2% to 75.6% when implementing the cuts on the new samples. To improve the signal selection efficiency, different variations of the initial cuts have been studied. In detail, this meant to vary:

- the transverse momentum requirements on the jets: lower the required p_T values of several or all of them
- the b-tag requirement: tighten or loosen it, require zero, one or two b-tagged jets
- the missing transverse energy and transverse energy sum requirements
- the conditions for the veto on overlapping muons and jets: ΔR, p_T requirement of the muons and jets taken into account
- add new cuts: require a hadronically decaying top quark: $x < m_{jjb} < y$

More than 40 different combinations of altered cut values have been tested for the resulting signal selection efficiency and purity. In Figure 7.4, some of these combinations yielding clearly better results than the initial cut values, are displayed. Here, initial values mean the cuts starting off from for the optimization. For the other cuts, always the values that differ from the initial values are given: the red square shows the resulting purity and efficiency for the initial cuts but with requiring only $E_T^{miss} > 30$ GeV (E_T^{miss} is labeled 'MET' in this plot) instead of $E_T^{miss} > 40$ GeV and four jets with $p_T > 30$ GeV instead of > 40 GeV. The blue triangle shows the initial cuts but requiring four jets with $p_T > 25$ GeV and $E_T^{miss} > 30$ GeV. Shown with a yellow triangle are the results when requiring four jets with transverse momenta greater than 25 GeV, a missing transverse energy greater than 30 GeV and a transverse energy sum of at least 200 GeV. The 'final' cut values are discussed below. Besides altering other cuts, for the examples shown the transverse momentum requirements on the four jets in the event are lowered, combined with a lower missing transverse energy and lower total transverse energy requirement. It is also attempted to add new cuts, for example require an invariant mass within 20 GeV of the nominal top quark mass from the combination of two jets and a b-jet and choose that combination as top quark with its invariant mass closest to the nominal one. Some cuts, e.g. requiring a second b-tagged jet or adding the hadronically decaying top quark, improve the purity of the collected sample but lower the efficiency excessively. A combination of cuts that result in a good signal efficiency while not leading to a bad purity of the sample is sought.

The cut values yielding the best signal efficiency of 19.07% (called 'embedding selection' in the following) with an acceptable purity of 76.90% are labeled final values in Figure 7.4. In detail, these are:

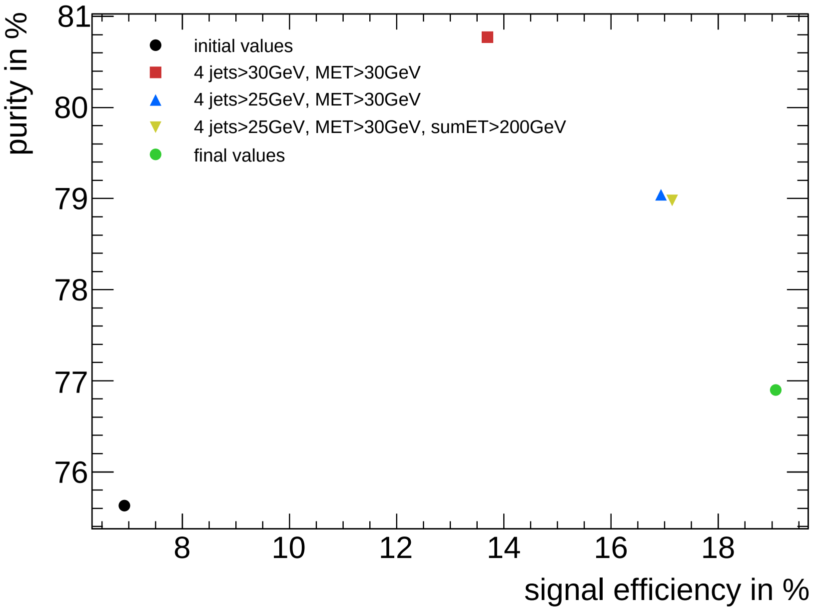

Figure 7.4: Examples of purities and embedding signal selection efficiencies obtained from testing different cut values. Initial values means the cuts from ref. [59]. For the other entries, the specified cut values have been changed in relation to the initial values.

- cut 1: one muon with transverse momentum above 20 GeV and less than 10 GeV deposited in calorimeter cells in a hollow cone with $\Delta R < 0.2$ around the muon is found
- cut 2: transverse energy sum of more than 200 GeV
- cut 3: require four jets with transverse momenta greater than 20 GeV
- cut 4: one of the four jets is required to have an associated b-tag with jet weight of at least 5.72
- cut 5: the invariant mass of two jets with transverse momenta greater than 35 GeV should lie within 20 GeV of the nominal W mass
- cut 6: events with muons ($p_T > 20$ GeV) overlapping with jets ($p_T > 15$ GeV) within ΔR<0.3 are rejected
- cut 7: missing transverse energy above 30 GeV
- cut 8: events containing high-energetic, isolated electrons ($p_T > 20$ GeV, less than 20 GeV deposited in calorimeter cells in a hollow cone with $\Delta R < 0.3$ around the electron) are removed

The event numbers expected for an integrated luminosity of 35.5 pb^{-1} to pass the final cuts are summarized in Table 7.2. As can be seen, most of the W + jets background can be well suppressed, the Z + jets background is negligible and the QCD $b\bar{b}$ background is cut away almost completely. The 4 jets requirement and the b-tag are very effective cuts. $t\bar{t}$ decays with at least one lepton other than that wanted for the embedding constitute the dominant background.

	$t\bar{t}$ 'signal' $t\bar{t} \to \mu\nu bqqb$	other $t\bar{t}$ with ≥ 1 lepton	W+jets	Z+jets	$b\bar{b}$	all backgrounds
no cut	820.1 ± 28.6	2318.2 ± 48.1	76241.2 ± 276.1	8302.6 ± 91.1	2623450.0 ± 1619.7	2710311.9 ± 1646.3
cut 1	618.0 ± 24.9	282.9 ± 16.8	18813.3 ± 137.2	1212.8 ± 34.8	378723.3 ± 615.4	399032.2 ± 631.7
cut 2	597.6 ± 24.4	247.4 ± 15.7	8974.3 ± 94.7	587.2 ± 24.2	118399.6 ± 344.1	128208.5 ± 358.1
cut 3	487.2 ± 22.1	158.2 ± 12.6	995.2 ± 31.5	73.1 ± 8.5	23233.3 ± 152.4	24459.8 ± 156.4
cut 4	366.9 ± 19.2	119.9 ± 10.9	57.9 ± 7.6	2.8 ± 1.7	14660.5 ± 121.1	14841.1 ± 121.8
cut 5	233.9 ± 15.3	60.9 ± 7.8	18.5 ± 4.3	1.0 ± 1.0	2684.4 ± 51.8	2764.8 ± 52.6
cut 6	201.8 ± 14.2	47.4 ± 6.9	16.9 ± 4.1	0.9 ± 0.9	167.9 ± 13.0	233.0 ± 15.3
cut 7	157.9 ± 12.6	40.6 ± 6.4	11.8 ± 3.4	0.5 ± 0.7	7.9 ± 2.8	60.8 ± 7.8
cut 8	156.3 ± 12.5	26.9 ± 5.2	11.7 ± 3.4	0.5 ± 0.7	7.9 ± 2.8	47.0 ± 6.9

Table 7.2: Expected number of events for the different background processes after embedding selection for an integrated luminosity of $35.5\,\mathrm{pb}^{-1}$.

7.2.4 Comparison of embedded and reference simulation

To validate the embedding procedure, an embedded Monte Carlo simulation $t\bar{t}$ event sample is compared to a reference $t\bar{t}$ simulation sample. The single steps for this consist of applying the embedding selection to a Monte Carlo simulation $t\bar{t}$ sample, running the embedding on the selected events and finally applying a modified embedding selection on the embedded events. In this modified embedding selection, the same cuts as in the embedding selection are applied but a high-energetic τ lepton ($p_T > 20\,\mathrm{GeV}$) is required instead of the muon. The reference, not-embedded sample is collected by applying the modified embedding selection to a $t\bar{t}$ simulation sample.

The distributions of some variables are shown in Figure 7.5. Although there are some differences between embedded and reference samples, the overall shapes agree within 10-20%, even for complex quantities such as the reconstructed transverse W boson and top quark masses.

Discrepancies in the transverse momentum distributions can result from the embedding step. From the reconstruction of the embedded τ lepton, slightly different momenta than those of the original muon may result due to e.g. inexact measuring or smearing in the reconstruction algorithm. Differences in the p_T distributions will affect energy distributions and thus small discrepancies between the embedded and reference sample are expected in the missing transverse energy and transverse energy sum distributions as well.

7.2.5 Comparison of embedded data and reference simulation

Embedded collision data is compared to a mixture of reference Monte Carlo simulation samples.

In collision data, the lowest unprescaled muon trigger ($p_T(\mu) > 13\,\mathrm{GeV}$) is required, basic event cleaning cuts are applied and a Good Runs List is used. The embedding selection is then applied but due to too few events in data, only 3 instead of four jets are required. The embedding is run on the selected events. After the embedding, a modified embedding selection is applied to embedded data, requiring a τ jet with $p_T > 20\,\mathrm{GeV}$ instead of the muon. No trigger information is available after the embedding, thus no additional $\tau + E_T^{miss}$ trigger is added to the modified embedding selection on data.

The loosened embedding selection (requiring 3 instead of 4 jets) plus the muon trigger is also applied to different Monte Carlo simulation samples to calculate how many events of what background process are to be expected. Since this selection is the one that initially filters out data events, it is thus possible to scale the individual simulation samples according to expectations in data.

The modified embedding selection requiring a τ lepton instead of a muon is then applied to Monte Carlo simulation samples. Additionally, a combined $\tau + E_T^{miss}$ trigger is required, with the thresholds set to $p_T > 20\,\mathrm{GeV}$ and $E_T^{miss} > 25\,\mathrm{GeV}$ The individual background contributions are scaled to the expectations extracted from the preceding step (applying the loosened embedding selection to different Monte Carlo simulation samples).

Additionally, the loosened embedding selection plus the muon trigger are required on $t\bar{t}$ Monte Carlo simulation. The selected events are embedded and the modified embedding

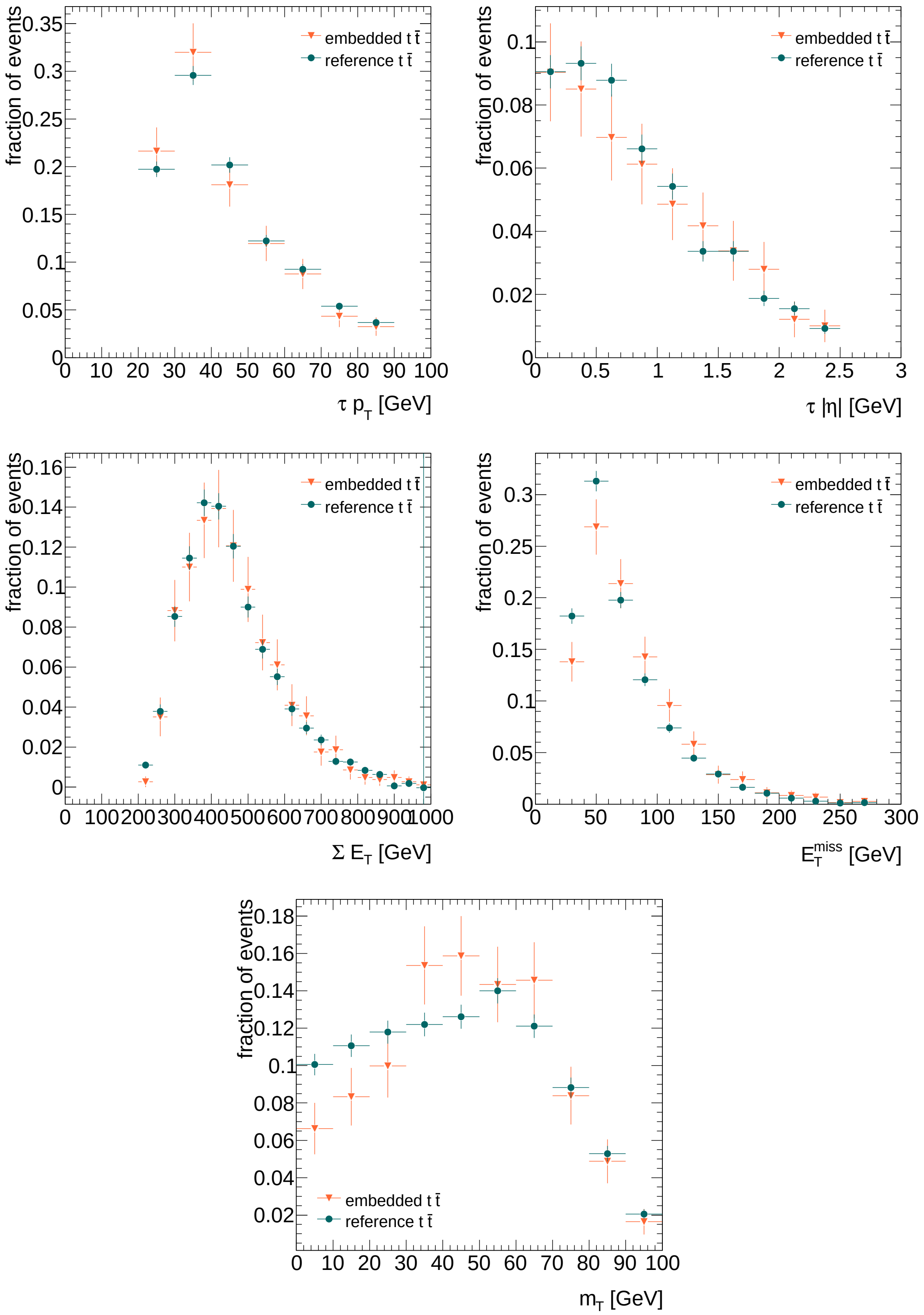

Figure 7.5: Comparison of several distributions in embedded and reference $t\bar{t}$ Monte Carlo simulation. Errors are statistical only. Shown are τ p_T and $|\eta|$ distributions, transverse energy sum, missing transverse energy and reconstructed transverse W boson mass.

sample	expected events
$t\bar{t}$	171.2±1.4
single top	11.3±0.3
W + jets	16.8±2.1
QCD	12.4±3.2
Sum MC	212±7
Data	219

Table 7.3: Expected events from Monte Carlo simulation and observed events from data after embedding selection. Uncertainties are statistical only.

selection requiring a τ instead of a muon and no $\tau + E_T^{miss}$ trigger is applied to the embedded simulation events.

Distributions for some variables in embedded data and reference Monte Carlo simulation are shown in Figure 7.6. Expected events from simulation after applying the muon trigger and embedding selection and observed events in embedded data after applying the selections as described above are summarized in Table 7.3.

As for the comparison of reference and embedded Monte Carlo simulation (see preceding paragraph), the overall shapes of reference simulation and embedded collision data agree mostly well within errors. Discrepancies in the pseudorapidity distributions are expected for low $|\eta|$ because of a low muon detection efficiency in this region. The differences between the transverse momentum distributions is studied separately. Differences between the embedded $t\bar{t}$ simulation and reference $t\bar{t}$ simulations can be seen in all variable distributions. However, they are not as large as for embedded data and reference simulation. It could not be finally explained where the discrepancies between embedded collision data and reference Monte Carlo simulation for low transverse momenta and pseudorapidity of the τ lepton arise from. It may be that the effect is at least part due to the low statistics and in further studies with more data it may be reduced.

For the transverse $\tau + E_T^{miss}$ mass shown in Figure 7.6, the shapes agree mostly within large statistical errors. As the integrated luminosity collected by ATLAS increases, the distributions are expected to agree better as statistical fluctuations won’t have such a large impact on them.

7.2.6 Systematic uncertainties

To study systematic uncertainties of the embedding, different approaches are made. The studies are performed on $t\bar{t}$ Monte Carlo simulation samples as well as on data taken by ATLAS in 2010.

$\mu \rightarrow \mu$ embedding Systematic uncertainties introduced by the embedding itself are studied by applying the embedding selection, running $\mu \rightarrow \mu$ embedding on selected events, i.e. replacing the selected muon with a simulated one and comparing different variables of the

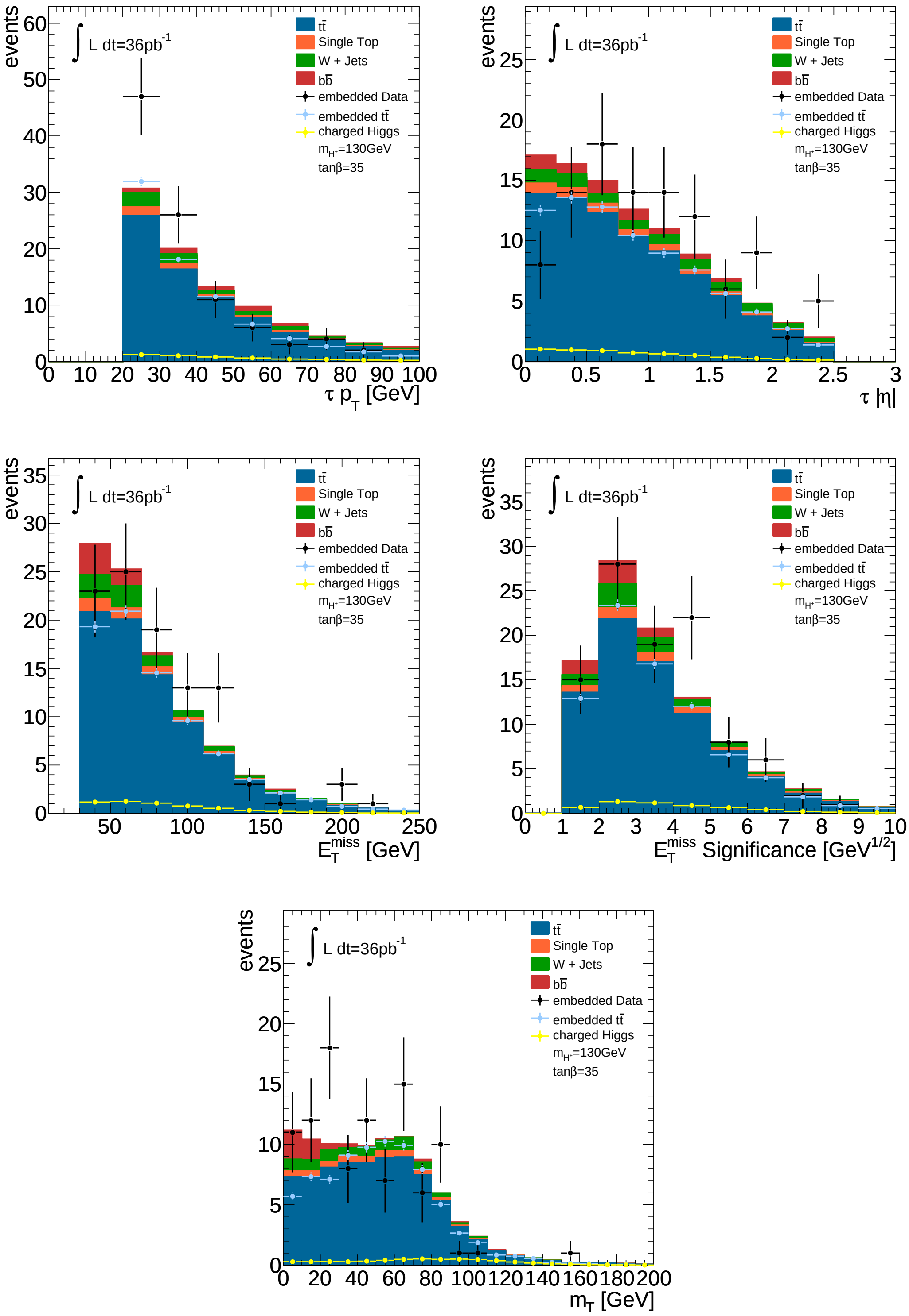

Figure 7.6: Comparison of distributions of embedded data with reference Monte Carlo simulation after embedding selection applied to collision data and modified embedding selection applied to simulation. Hypothetical signal for a reference point in parameter space and embedding performed on $t\bar{t}$ are superimposed. Shown are τ p_T and $|\eta|$ distributions, missing transverse energy, its significance and the reconstructed transverse mass. Errors are statistical only.

embedded events to those of the initially selected events. Thus uncertainties in distributions such as the transverse momentum, pseudorapidity, transverse energy sum and missing transverse energy due to the embedding can be studied.

This procedure is applied separately to collision data and $t\bar{t}$ Monte Carlo simulation.

Figure 7.7 shows some variable distributions in data. No deviations in the distributions due to the embedding can be observed. The systematic errors caused by the embedding are almost negligible and always within the 10% error bar shown in the plots of Figure 7.7. Small deviations between the two samples are expected, since e.g. the transverse momentum of the initially selected muon and the embedded muon will not always be exactly the same due to e.g. reconstruction uncertainties. This of course affects other variables such as the missing transverse energy, the transverse energy sum and m_T.

In Figure 7.8, the same distributions as in Figure 7.7 are shown, but using $t\bar{t}$ simulation and embedded $t\bar{t}$ simulation instead of collision data and embedded data. Because of the limited number of events in collision data compared to Monte Carlo simulation, the statistical errors are much smaller in the latter one. Since systematic errors introduced by the embedding step can be studied on simulated data as well, these distributions are used in the following to estimate uncertainties. The systematic uncertainty due to the embedding itself is extracted from the ratio plots in Fig. 7.8. The error bars of the embedded distributions agree mostly within a 15% range with the values of the not-embedded distributions.

$\mu \rightarrow \tau$ embedding In a second study, some embedding settings are altered compared to the default embedding selection. The embedding selection is compared to modified embedding selections:

- a higher transverse momentum of the selected muon is required (25 instead of 20 GeV).
- a tighter isolation of the selected muon is required (less than 4 GeV instead of 10 GeV deposited in calorimeter cells in a hollow cone with $\Delta R < 0.3$ around the selected muon).
- the selected muon is not required to be isolated.

In Figure 7.9 muons are replaced by τ leptons, with varying selection criteria on the muon. The baseline curves correspond to the signal selection (see chapter 6). The other distributions correspond to the signal selection with one specific setting altered at a time. For the ’loose’ distributions (red squares), no isolation requirement on the muon before embedding is imposed. Shown in blue (triangles) are the distributions when requiring a muon with $p_T > 25$ GeV instead of 20 GeV. Finally, shown in green circles, a tighter isolation is required on the muon before embedding with only 4 GeV instead of 10 GeV of calorimeter cell deposits in a hollow cone with $\Delta R < 0.3$ around the muon. The ’loose’ curves in 7.9 are especially interesting for estimating effects from QCD multi-jet events, e.g. if they are not well described in simulation their effect could be underestimated. It is thus important to see that the loose selection, which mimics embedding performed on QCD processes where muons are expected not to be isolated, does not change the shapes of the distributions significantly. The tighter selection shown in 7.9 is important for future studies. With worse pile-up conditions, constraints on selected objects might have to get tighter. Shapes of distributions are not altered or shifted very much compared to the baseline selection.

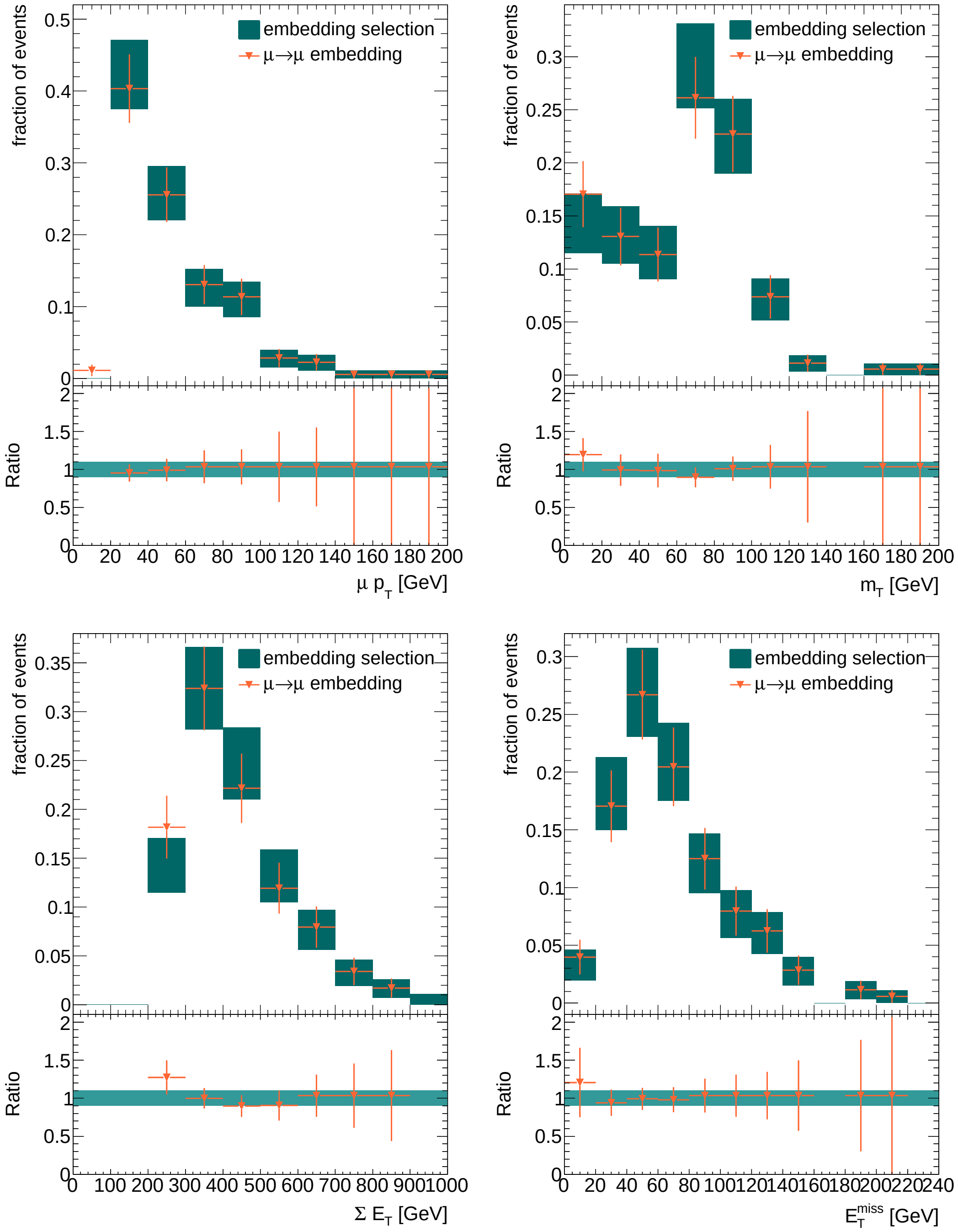

Figure 7.7: Comparison of data that the embedding selection is applied to and $\mu \to \mu$ embedded collision data. The embedding selection is applied to data shown in green and $\mu \to \mu$ embedding is run on these selected events (orange triangles). Shown are transverse momentum of the muon, transverse W mass, transverse energy sum and missing transverse energy. The same events are used in both samples. Uncertainties are statistical only. The ratio plots show embedded data divided by data to which the embedding selection is applied, with the box indicating a 10% error band.

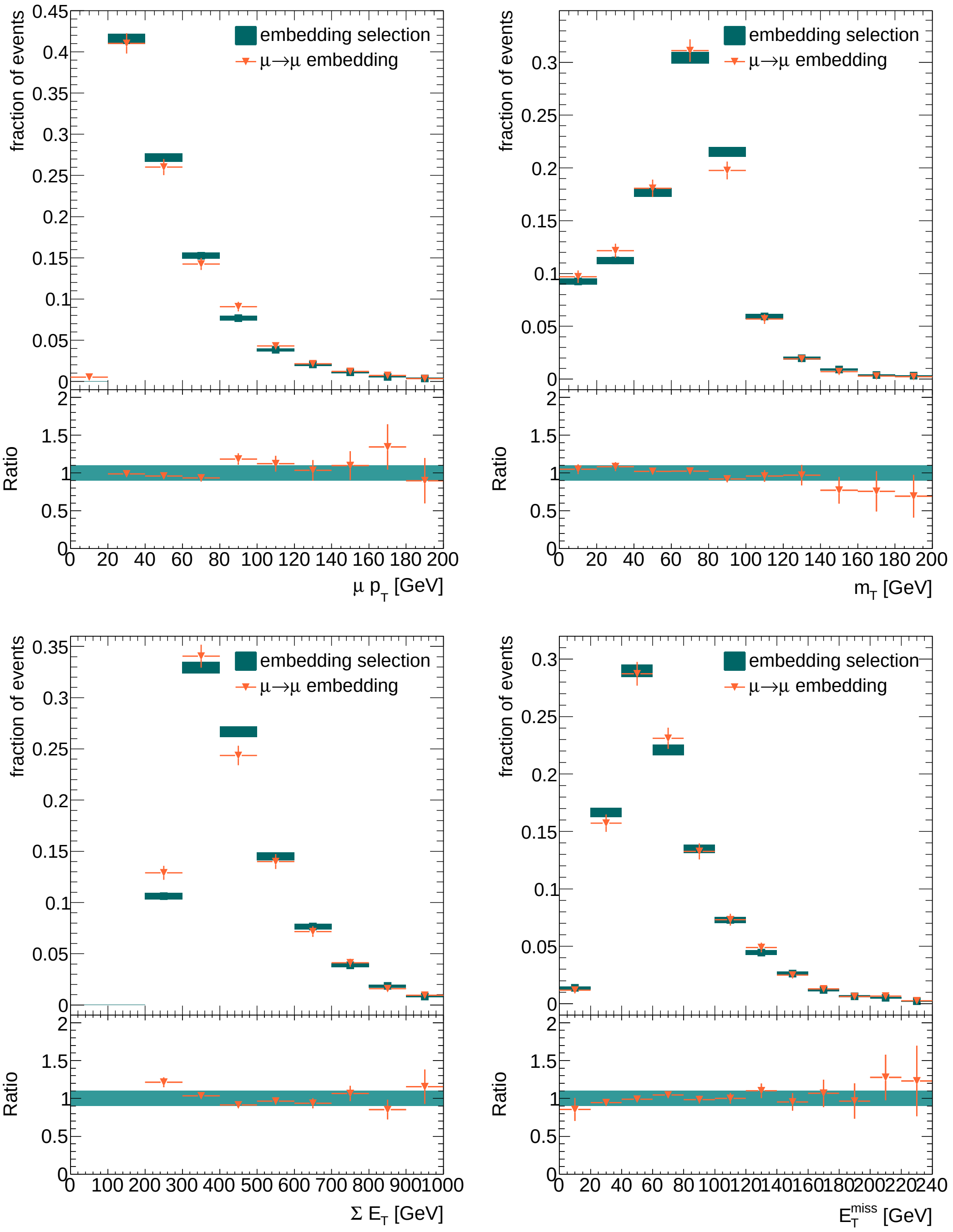

Figure 7.8: Comparison of $t\bar{t}$ Monte Carlo simulation that the embedding selection is applied to and $\mu \longrightarrow \mu$ embedded $t\bar{t}$ simulation. The embedding selection is applied to Monte Carlo simulation shown in green and $\mu \rightarrow \mu$ embedding is run on these selected events (orange triangles). Shown are transverse momentum of the muon, transverse W mass, transverse energy sum and missing transverse energy. Uncertainties are statistical only. The ratio plots show embedded simulation divided by simulation to which the embedding selection is applied, with the box indicating a 10% error band.

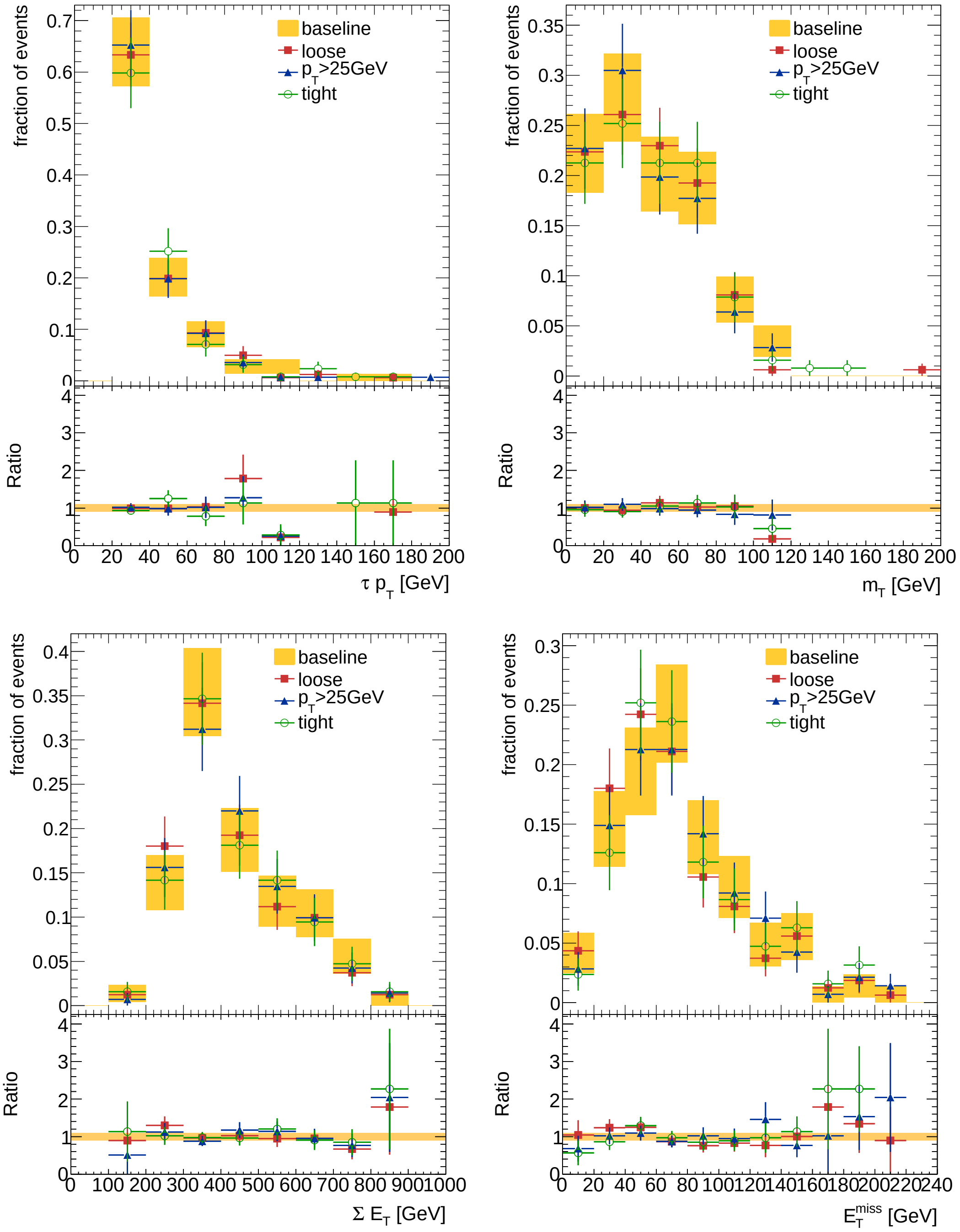

Figure 7.9: Comparison of $\mu \rightarrow \tau$ embedded collision data with varying requirements on the selected muon. ’Baseline’ means settings as in the embedding selection (yellow boxes), for ’loose’ no isolation cuts have been required for the selected muon (red squares), for one sample the p_T cut on the muon was set to 25 instead of 20 GeV (blue triangles) and in green circles the distributions are shown for a tighter isolation cut on the selected muon (less than 4 GeV instead of 10 GeV of calorimeter cell deposits in a hollow cone with $\Delta R < 0.3$ around the muon). Uncertainties are statistical only. The ratio plots show each varied distribution divided by the baseline distribution, drawn in the corresponding colors. The box indicates a 10 % error band.

Because of large statistical uncertainties due to the limited size of the collision data sample, the corresponding distributions are also shown for $\mu \rightarrow \tau$ embedded $t\bar{t}$ Monte Carlo simulation in Figure 7.10. With a larger simulated data sample and thus smaller statistical errors, it is easier to estimate systematic errors. Since it could be shown in Figure 7.9 that looser isolation criteria do not cause an exceeding increase of QCD events, one can rely on simulation.

Systematic errors in $\mu \rightarrow \tau$ embedding on $t\bar{t}$ Monte Carlo simulation due to different selection criteria in the embedding selection concerning the kinematics and isolation of the muon are extracted from the ratio plots in Figure 7.10. The error bars of the varied selections and the baseline values agree mostly within a 20% range.

τ energy scale The effect of varying the τ energy scale on the transverse $\tau + E_T^{miss}$ mass distribution is investigated on embedded data. An uncertainty of ±5% is assumed on the τ energy scale [55]. Applying it causes a maximum modification of 6.5% events that pass the signal selection. The effect of varying the τ energy scale on the m_T shape in embedded data is shown in Fig. 7.11.

7.2.7 Application

Because of limited statistics and software problems, the signal selection presented in the previous chapter had to be loosened for the estimation of the background containing true τ jets with the embedding method.

A minimum of three instead of four jets is required in the events. Furthermore, the reconstruction of the hadronically decaying top quark is dropped.

No trigger could be required in embedded data, because the information is currently not available after embedding. Due to a current software problem in the embedding package, τ identification does not work properly. Therefore selected τ jet candidates are matched to a true τ instead of requiring τ identification. Since the τ is the only part in the embedded data coming from simulation, truth information is available.

This loosening causes a bias in the shape of the m_T distribution, shown in Figure 7.12. The m_T distribution is shown for the baseline selection applied to $t\bar{t}$ Monte Carlo simulation as well as the loosened selection, for which no trigger, a truth-matched τ, only 3 jets and no hadronically decaying top quark are required. Furthermore, the loose selection is applied to embedded $t\bar{t}$ simulation.

To estimate the bias, the loose distribution in Figure 7.12 is normalized to the baseline distribution in the m_T range of 30-70 GeV, since embedded data will be normalized to collision data in this range and thus differences between the distributions in a higher m_T range resulting from the loosening of the selection can be estimated. The normalization factor is then applied to the higher mass range of the loose distribution and the variation to the baseline distribution in this range is calculated.

The systematic error due to the bias is estimated to be about $+15\%$.

The overall systematic error is calculated by taking the square root of the sum of the squared uncertainties: ±15% due to the embedding, ±20% from the embedding settings,

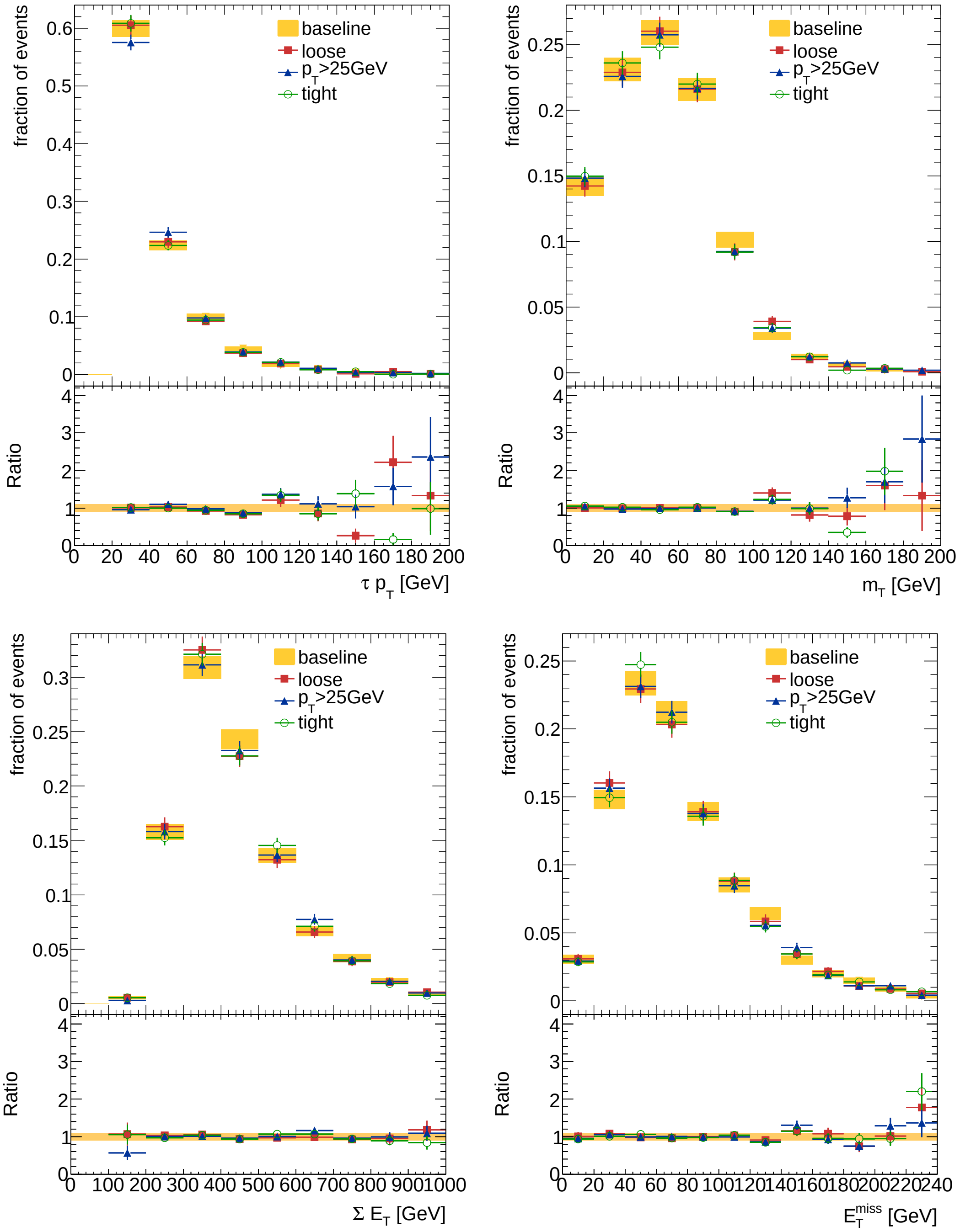

Figure 7.10: Comparison of $\mu \to \tau$ embedded $t\bar{t}$ Monte Carlo simulation with varying requirements on the selected muon. 'Baseline' means settings as in the signal selection (yellow boxes), for 'loose' no isolation cuts have been required for the selected muon (red squares), for one sample the p_T cut on the muon was set to 25 instead of 20 GeV (blue triangles) and in green circles the distributions are shown for a tighter isolation cut on the selected muon (less than 4 GeV instead of 10 GeV in a hollow cone with $\Delta R < 0.3$ around the muon). Uncertainties are statistical only. The ratio plots show each varied distribution divided by the baseline distribution, drawn in the corresponding colors. The box indicates a 10% error band.

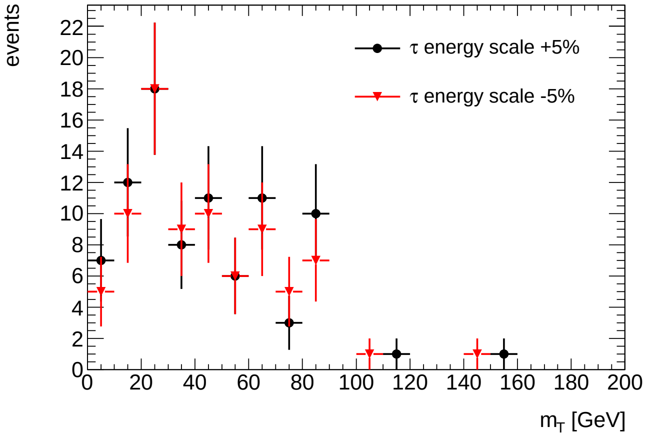

Figure 7.11: Effect of varying the τ energy scale on the m_T distribution in embedded collision data. Errors are statistical only.

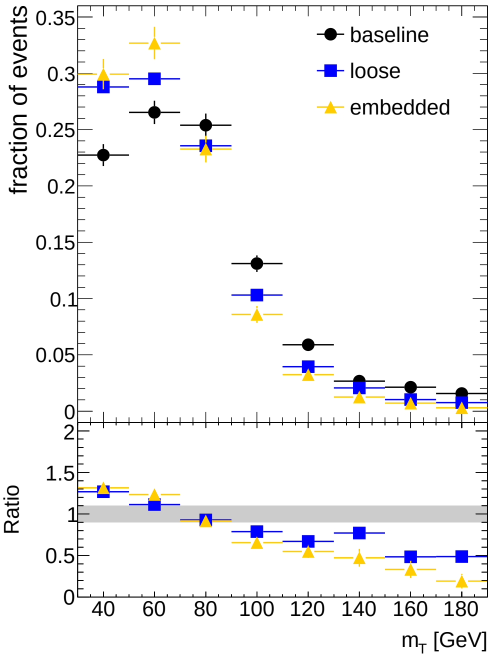

Figure 7.12: Comparison of the m_T shape for different selections. The distribution is shown for full signal selection (baseline), loosened signal selection (no trigger, truth-matching the τ instead of requiring τ identification, requiring a minimum of three instead of four jets and not reconstructing the hadronically decaying top quark) applied to $t\bar{t}$ Monte Carlo simulation. The loose selection is also applied to embedded $t\bar{t}$ simulation (embedded). In the ratio plot, the loose and embedded distributions are each divided by the baseline distribution with the gray box indicating a 10% error band. Errors are statistical only.

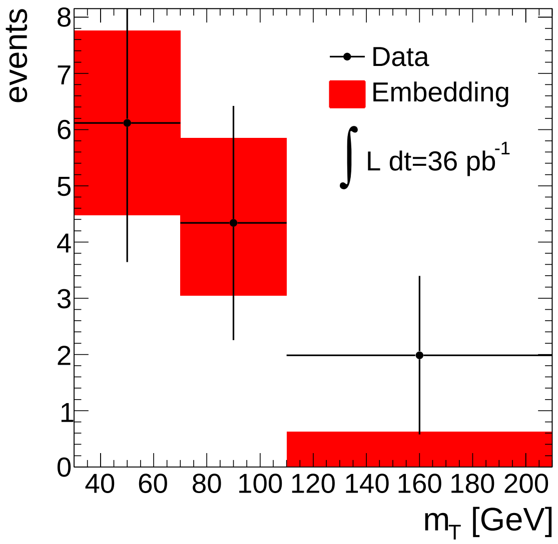

Figure 7.13: Comparison of the m_T distribution of collision data with contributions from fake τ jets subtracted and embedded data. The full baseline selection is applied to collision data, the loosened signal selection to embedded data. Embedded data are normalized to collision data in the range of 30 to 70 GeV (first bin). Uncertainties are systematic and statistical.

-6.5% because of the uncertainty of the τ energy scale and -20% due to the loosening of the signal selection.

To estimate the background contribution with true τ jets, the shape of the m_T distribution is taken from embedded data. The normalization is taken directly from collision data. The full signal selection is applied to collision data, where contributions from other backgrounds have already been subtracted using results from the other background estimation methods (see subsequent sections). After applying the loose signal selection to embedded data, the embedded m_T distribution is normalized to that of collision data in a range of 30 to 70 GeV and the resulting normalization factor is applied to embedded data for $m_T > 70$ GeV. In the region from 30 to 70 GeV, the signal contribution is expected to be low and the events in collision data are expected to be from background processes. The two distributions are shown in Figure 7.13.

Between 70 and 210 GeV, 6.3± 2.5 events are seen in collision data, with backgrounds from fake rates and QCD estimations subtracted (see subsequent sections). From embedded data, even with the loosened selection only $4.7 \pm 1.3(\text{stat.})^{+1.4}_{-1.2}(\text{syst.})$ events with true τ jets are retained in this range. As can be seen from Figure 7.13, the background estimation is still limited by statistical errors because of low event numbers in the control sample used for embedding. But within large statistical uncertainties, background estimation and data agree well.

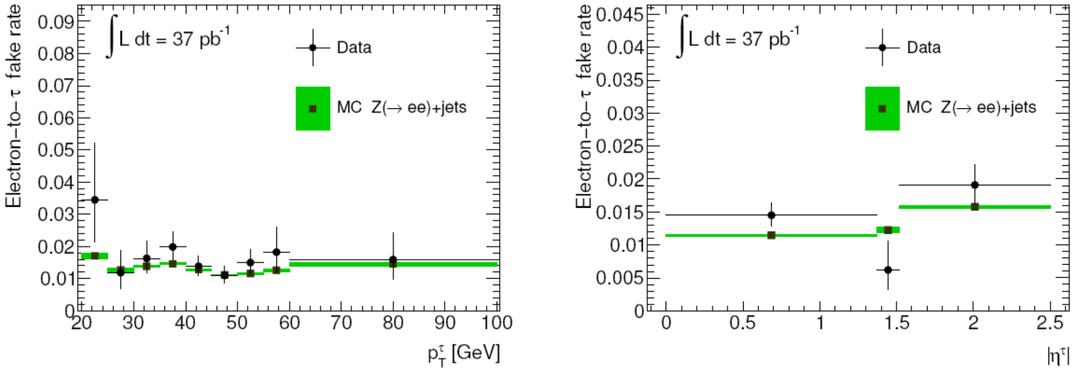

Figure 7.14: Fake rate of probe electrons that pass τ ID, electron veto and overlap removal with electrons, binned in the transverse momentum and pseudorapidity. Errors are statistical only [56].

7.3 Background with electrons faking τ leptons

The background contribution with electrons mis-identified as τ leptons are estimated with a fake rate. These events can result from W+jets and single top processes as well as from $t\bar{t}$ decays. The electron-to-τ fake rate is estimated using a tag-and-probe method [55, 56].

A clean and unbiased electron sample is collected from data in the $Z \to ee$ channel. One of the electrons, the tag electron, has to pass a tight electron selection. The other electron is used as the probe if it is reconstructed as a τ candidate. As the rate of electrons faking τ jets with three associated tracks is negligible compared to that with exactly one associated track, only the latter are taken into account for this study. The results of the fake rate measured in data and that modeled in simulation, shown in Figure 7.14, agree mostly within errors. Relevant systematic uncertainties taken into account are

- the contamination of the sample with QCD multi-jet events: ≈30%
- the choice of the mass window around the Z boson mass applied to tag-and-probe objects: ≈13%
- the uncertainty on the electron energy scale: ≈2%

The number of events with electrons faking τ leptons is estimated by labeling each true electron from Monte Carlo simulation passing as a τ candidate as τ jet and weighting it with the probability of the fake rate measured before. Quantities such as e.g. ΣE_T, E_T^{miss} and m_T are recalculated assuming the electron is a τ jet. Finally, the baseline cuts (see chapter 6) without the τ identification are applied and the events passing the selection are counted. The results are shown in Table 7.4. For data, both statistical and systematic uncertainties are given, while for Monte Carlo simulation only statistical uncertainties are given. Results from the fake rate and from Monte Carlo simulation agree within large uncertainties.

Sample	Fake rate prediction	Monte Carlo simulation prediction
$t\bar{t}$	1.08±0.01±0.38	1.50±0.09

Table 7.4: Predicted number of events after baseline selection from the fake rate from a $Z \rightarrow ee$ sample and Monte Carlo simulation, applied to a $t\bar{t}$ sample. For simulation events, statistical errors only are given. The expected event numbers from simulation are normalized to 36 pb^{-1} [55].

7.4 Background with muons faking τ leptons

To estimate the muon-to-τ fake rate, a $Z \rightarrow \mu\mu$ control sample is studied with a method similar to that for the electron-to-τ fake rate [55, 56]. Data and simulation agree well. With the Monte Carlo simulation expectations on this fake rate being much smaller than the uncertainties of the other backgrounds, it is found that processes in which muons are misidentified as τ jets are negligible.

7.5 Background with jets faking τ leptons

As for the estimation of the background with mis-identified electrons, the background contribution of jets faking τ leptons is measured using a fake rate [55, 56]. Mis-identified jets result mostly from $t\bar{t}$ decays, single top and W+jets events.

A γ + jet control sample is selected from data. Jets in these events are dominantly of quark origin, as it is the case especially in the dominant $t\bar{t}$ backgrounds, but also in single top and W + jets processes. Events are required to pass a γ trigger and the photon must pass a tight isolation selection. Additionally, a jet fulfilling certain criteria must be present. An object enters the numerator of this fake rate if it passes complete τ identification. The denominator is made up of objects passing τ jet candidate reconstruction and lepton vetoes. This procedure is applied to Monte Carlo simulation as well. Predictions from data and simulation agree well within uncertainties as shown in Figure 7.15.

Relevant systematic uncertainties taken into account are

- the contamination of the sample with QCD multi-jet events: ≈10%
- uncertainties of the control sample selection: ≈15%
- correlations of the tag and probe objects: ≈3%

A jet is labeled as τ jet if it passes the denominator requirements of the fake rate (reconstructed as τ jet candidate and surviving lepton vetoes) and weighted with the calculated fake rate. It is removed from the event to avoid double-counting. The event selection is then applied and the weights of all events passing the cuts are summed. The prediction from Monte Carlo simulation agrees well with observation in data. The results are shown in Table 7.5.

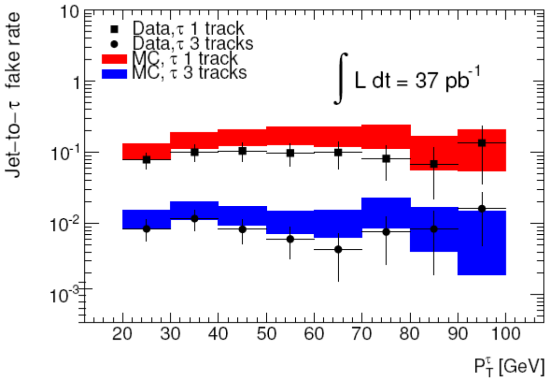

Figure 7.15: Jet-to-τ fake rate, determined from a γ+jet sample. The fake rate is measured separately for τ jets with 1 or 3 tracks. For data, statistical uncertainties are given and for MC statistical and systematic uncertainties [56].

Sample	Fake rate prediction	Monte Carlo simulation prediction
$t\bar{t}$	1.7±0.2±0.3	1.9±0.2

Table 7.5: Predicted number of events after baseline selection from the fake rate from a γ+jets sample and $t\bar{t}$ Monte Carlo simulation. For simulation, statistical errors only are given. The event numbers are normalized to 36 pb^{-1} [55].

7.6 QCD background

The QCD multi-jet background to the τ + jets channel is estimated using an inverted selection [55, 56]. This is identical to the τ + jets selection but requires looser τ jet identification and rejects events with tight τ identification. The inverted selection is applied to data. After subtracting contributions from other non-QCD backgrounds estimated from simulation, the E_T^{miss} distribution is used to model the QCD background. Using the shape from this model and that for the distribution of the sum of non-QCD events from simulation, a fit is performed on the distribution of the missing transverse energy on data after the τ + jets signal selection is applied to extract the number of QCD multi-jet events. The result is shown in Figure 7.16, separately for τ jets with one associated track and for all τ jets. The assumption here is that the E_T^{miss} distribution for QCD has the same shape for the signal and the inverted selection, respectively. It can be shown that this assumption is justified and the distributions of missing transverse energy after the two different selections agree within statistical errors.

Relevant systematic uncertainties taken into account are

- in the shape and relative normalization of $t\bar{t}$ and W processes which are taken from Monte Carlo simulation: ≈ 15%
- differences in the E_T^{miss} shape in control and signal regions: ≈5%

The contribution from QCD multi-jet processes after all cuts is estimated to be 18.8±6.2±3.0 events.

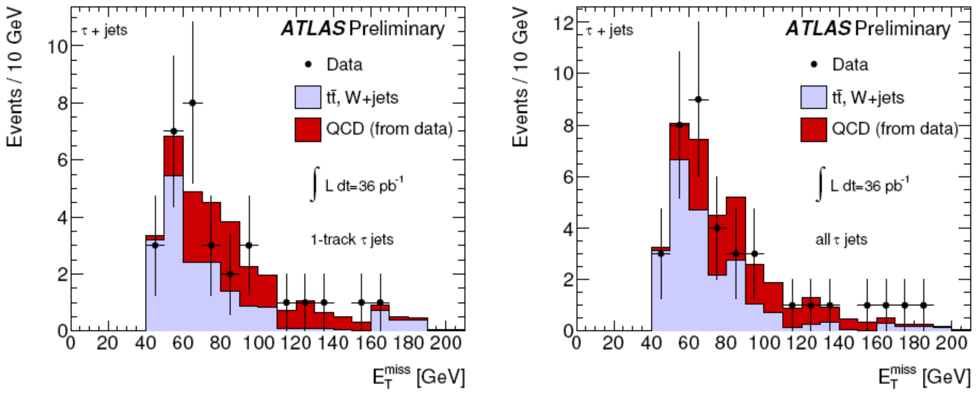

Figure 7.16: Fit to the missing transverse energy distribution after all cuts. Two shapes are used, one for $t\bar{t}$ and W+jets backgrounds and one for QCD. The fit is shown separately for 1-prong τ jets and all τ jets. Errors are statistical only [55]

e→ τ fakes	jet→ τ fakes	QCD	true τ jets	all	data
1.1±0.0±0.4	1.7±0.2±0.3	18.8±6.2±3.0	$10.8\pm3.1^{+1.4}_{-1.2}$	32±9±7	33

Table 7.6: Expected events from different contributions to the background in charged Higgs boson searches where $H^+ \to \tau\nu = 1$ is assumed. Errors are statistical and systematic.

7.7 Final results

Combining the estimates of different background contributions, 32±9±7 events are expected and 33 are observed in collision data. The numbers with statistical and systematic uncertainties from the different background contributions for the whole m_T range are summarized in Table 7.6. Figure 7.17 shows the m_T distribution in 2010 collision data compared to the data-driven background estimation. The agreement is reasonably good within the large uncertainties.

The transverse mass distribution is used in chapter 8 to derive a limit on the branching ratio $t \to H^+b$ assuming $H^+ \to \tau\nu = 1$.

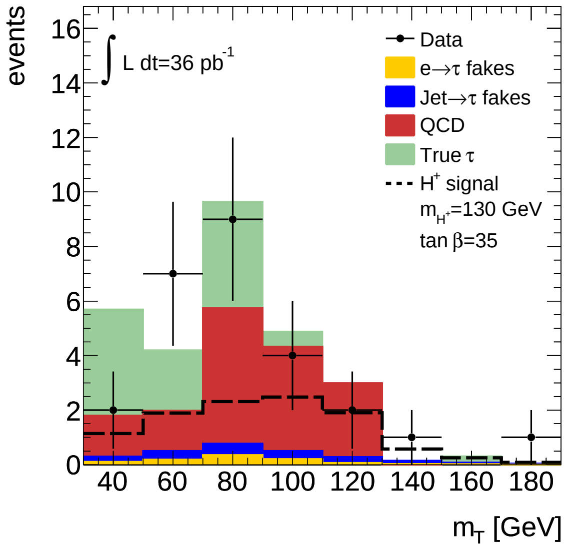

Figure 7.17: Result of data-driven background estimation. Shown is the $\tau + E_T^{miss}$ transverse mass distribution as observed in collision data after applying the full signal selection and estimates for different background contributions. Error bars on data indicate statistical uncertainties. A hypothetical charged Higgs boson distribution for $m_{H^+} = 130\,\text{GeV}$ and $\tan\beta = 35$, corresponding to a branching ratio $\text{BR}(t \to bH^+) \approx 6\%$ and assuming $\text{BR}(H^+ \to \tau\nu) = 1$ is superimposed. Standard Model $t\bar{t}$ decays would be reduced accordingly.

8 Exclusion limit

8.1 Theoretical basis

A preliminary goal in particle physics can be to set upper limits on hypothesized signal processes. Since the requirements to set a limit are not as tight as those for discoveries from a statistical point of view, it is possible to exclude i.e. New Physics processes already without much data.

In the following chapter, the method to calculate upper limits is explained based on references [62, 63].

Since no excess of data over the background estimation is found in chapter 7, an upper limit on the branching ratio $t \to H^+ b$ assuming $H^+ \to \tau\nu = 1$ is extracted from data collected by ATLAS in 2010.

8.1.1 Statistical tests

The common procedure to search for New Physics based on a frequentist statistical test consists of testing a hypothesis H_0 against another hypothesis H_1. To claim a discovery, the background-only model of known processes can be defined as H_0 which is tested against a model containing background and a signal playing the role of H_1. For setting upper limits, these roles are reversed: H_0 is then the model that consists of background and signal, while H_1 is the background-only hypothesis. The outcome of such a test can be quantified by specifying a p-value or significance Z. The p-value is defined as the probability to find data that is equally or less compatible with the predictions of the assumed hypothesis H. A hypothesis is regarded as excluded if the p-value is less than a certain value. To convert the p-value into a significance Z, the quantile Φ^{-1} of a standard Gaussian distribution is needed:

$$Z = \Phi^{-1}(1 - p). \tag{8.1}$$

The relation between the p-value and Z is illustrated in Figure 8.1. Standard values in particle physics to claim a discovery or set an exclusion limit require $Z > 5$ (corresponding to p$= 2.87 \cdot 10^{-7}$) and $Z = 1.64$ (p=0.05), respectively.

An often applied method for setting an exclusion limit is a frequentist significance test based on a likelihood ratio. Nuisance parameters, i.e. systematic uncertainties, in signal and background models whose values are unknown can be fitted from data with this method.

As an example, one may assume that a variable x is measured in a sample and a histogram is filled with the measured values n_k. Then

$$E[n_k] = \mu \cdot s_k + b_k \tag{8.2}$$

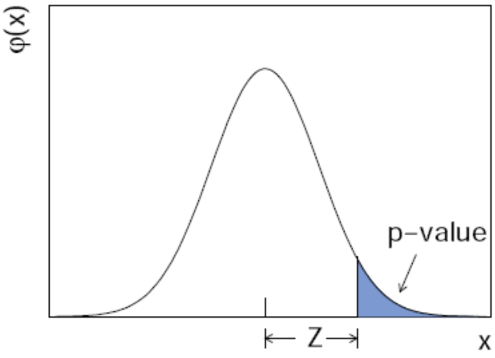

Figure 8.1: Relation between p-value and Z. $\varphi(x)$ shows a standard normal distribution [62].

is the expectation value of n_k, where s_k and b_k are the mean number of entries in the kth bin of the histogram.

$$s_k = s_{tot} \int_{bin\,k} f_s(x;\theta_s)\mathrm{d}x \tag{8.3}$$

$$b_k = b_{tot} \int_{bin\,k} f_b(x;\theta_b)\mathrm{d}x \tag{8.4}$$

The parameter μ defines the strength of the signal: μ=1 corresponds to the signal hypothesis while μ=0 describes the background-only hypothesis. f_s and f_b represent the probability density functions (pdfs) of x for signal and background events, respectively, with θ_s and θ_b characterizing their shapes. The normalization factor s_{tot} is fixed to a certain value depending on and given by the signal model. If other measurements are made to constrain nuisance parameters, i.e. systematic uncertainties, that yield values of m_l, their expectation values can be written as

$$E[m_l] = u_l(\theta). \tag{8.5}$$

Here, the u_l depend on θ and can be calculated.

The likelihood function L is given by the Poisson probabilities for all bins:

$$L(\mu,\theta) = \prod_{i=1}^{N} \frac{(\mu s_i + b_i)^{n_i}}{n_i!} \mathrm{e}^{-(\mu s_i + b_i)} \prod_{l=1}^{M} \frac{u_l^{m_l}}{m_l!} \mathrm{e}^{-u_l} \tag{8.6}$$

The profile likelihood ratio λ is built to test a hypothesized value of μ:

$$\lambda(\mu) = \frac{L(\mu,\hat{\hat{\theta}})}{L(\hat{\mu},\hat{\theta})} \tag{8.7}$$

Here, $\hat{\hat{\theta}}$ is the θ value maximizing L for a specified μ. $\hat{\mu}$ and $\hat{\theta}$ are maximum likelihood estimators. With nuisance parameters present, the profile likelihood is broadened relative to a profile likelihood with fixed values for θ.

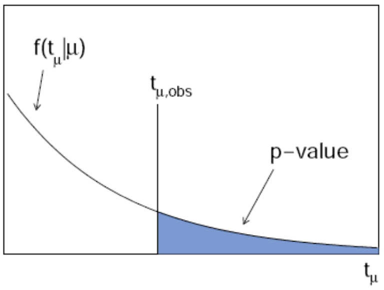

Figure 8.2: Relation between an observed value of the test statistic t_μ and the p-value obtained from it [62].

For reasons of convenience, one often uses

$$t_\mu = -2\ln\lambda(\mu) \tag{8.8}$$

as test statistic. Increasing disagreement between μ and the data is then represented by higher values of t_μ. This incompatibility can be quantified by calculating the p-value:

$$p_\mu = \int_{t_{\mu,\mathrm{obs}}}^{\infty} f(t_\mu|\mu)\mathrm{d}t_\mu. \tag{8.9}$$

The lower integral limit $t_{\mu,\mathrm{obs}}$ is the value of the test statistic observed in data. $f(t_\mu|\mu)$ represents the conditional probability density distribution assuming the hypothesis μ for the test statistic t_μ, which tests the hypothesized value of μ. In Figure 8.2, the relation between an observed value of the test statistic t_μ and the p-value obtained from it is illustrated.

8.1.2 Test statistic for upper limits

To set an upper limit on μ, the test statistic q_μ is defined as

$$q_\mu = \begin{cases} -2\ln\lambda(\mu) & \hat{\mu} \le \mu \\ 0 & \hat{\mu} > \mu \end{cases} \tag{8.10}$$

where $\lambda(\mu)$ is the likelihood ratio as in Equation 8.7. q_μ is set to zero for $\hat{\mu} > \mu$ because this case would not be interpreted as being less compatible with μ than the data acquired and it is hence not included in the rejection region. The way the test statistic is defined, the incompatibility between data and assumed values of μ increases with q_μ. To quantify the disagreement between the hypothesized μ and data, one may calculate the p-value in analogy to equation 8.9 using q_μ as test statistic and integrating from $q_{\mu,\mathrm{obs}}$ to infinity.

$$p_\mu = \int_{q_{\mu,\mathrm{obs}}}^{\infty} f(q_\mu|\mu)dq_\mu \tag{8.11}$$

Here $q_{\mu,\mathrm{obs}}$ is the observed value of the test statistic and $f(q_\mu|\mu)$ is the pdf of q_μ under the assumption of μ.

8.1.3 Alternative test statistic for upper limits

If only non-negative values of the strength parameter μ are to be regarded as physical models, an alternative test variable $\tilde{\lambda}(\mu)$ can be defined as

$$\tilde{\lambda}(\mu) = \begin{cases} \frac{L(\mu,\hat{\hat{\theta}}(\mu))}{L(0,\hat{\hat{\theta}}(0))} & \hat{\mu} < 0 \\ \frac{L(\mu,\hat{\hat{\theta}}(\mu))}{L(\hat{\mu},\hat{\theta})} & \hat{\mu} \geq 0 \end{cases} \tag{8.12}$$

$\hat{\hat{\theta}}(0)$ and $\hat{\hat{\theta}}(\mu)$ are the conditional maximum likelihood estimators of θ for different values of the strength parameter, μ and 0. The test statistic $\tilde{q}_\mu$ corresponding to the alternative test variable is given by

$$\tilde{q}_\mu = \begin{cases} -2\ln\tilde{\lambda}(\mu) & \hat{\mu} \leq \mu \\ 0 & \hat{\mu} > \mu \end{cases} = \begin{cases} -2\ln\frac{L(\mu,\hat{\hat{\theta}}(\mu))}{L(0,\hat{\hat{\theta}}(0))} & \hat{\mu} < 0 \\ -2\ln\frac{L(\mu,\hat{\hat{\theta}}(\mu))}{L(\hat{\mu},\hat{\theta})} & 0 \leq \hat{\mu} \leq \mu \\ 0 & \hat{\mu} > \mu \end{cases} \tag{8.13}$$

While q_μ implies some important simplifications, one may want to use $\tilde{q}_\mu$ for smaller samples as the two test statistics become equivalent in the large sample limit [62].

8.1.4 Approximations on distributions

If testing to find an upper limit, the distributions $f(q_\mu|\mu)$ and $f(q_\mu|\mu')$ or the equivalents using the alternative test statistic $\tilde{q}_\mu$ are needed. Here, as before, the subscript of q defines the hypothesis that is tested, while the second argument of f refers to the values of the strength parameter assumed in data. The pdf with a different strength parameter μ' is needed to calculate what significance can be expected if the data distribution does not correspond to the values of μ that is tested. Usually the significance/p-value of an experiment is described by using the median significance under assumption of a certain signal model and accordingly distributed data, with which the $\mu = 0$ hypothesis can be excluded. For upper limits, normally the median upper limit on the strength parameter at a confidence level of 95% is calculated, given by the μ-value for which the median of the p-value is 0.05. If the sample is large enough, some approximations one the profile likelihood ratio can be made. But even for smaller sample sizes, the approximation usually yields accurate results [64].

For one parameter of interest, it can be shown that

$$-2\ln\lambda(\mu) = \frac{(\mu-\hat{\mu})^2}{\sigma^2} + \mathscr{O}(1/\sqrt{N}) \tag{8.14}$$

where $\hat{\mu}$ is Gaussian distributed with μ' as the mean value, σ is the standard deviation and

N the sample size. In the following, it is assumed that the $\mathscr{O}(1/\sqrt{N})$ term in equation 8.14 can be neglected. Then it can be shown that $q_\mu = -2\ln\lambda$ is χ^2 distributed for one degree of freedom with a noncentrality parameter $\Lambda = (\mu - \mu')^2/\sigma^2$, which is equal to zero if $\mu = \mu'$ [65].

The test statistic for upper limits can then be rewritten as

$$q_\mu = \begin{cases} \frac{(\mu-\hat{\mu})^2}{\sigma^2} & \hat{\mu} \leq \mu \\ 0 & \hat{\mu} > \mu \end{cases} \tag{8.15}$$

with the same requirements on $\hat{\mu}$ as before. The pdf $f(q_\mu|\mu')$ can then be found using the results of Wilks.

$$f(q_\mu|\mu') = \Phi\left(\frac{\mu' - \mu}{\sigma}\right)\delta(q_\mu) + \frac{1}{2\sqrt{2\pi q_\mu}}\exp\left(-\frac{1}{2}\left(\sqrt{q_\mu} - \frac{\mu - \mu'}{\sigma}\right)^2\right) \tag{8.16}$$

The corresponding cumulative function is

$$F(q_\mu|\mu') = \Phi\left(\sqrt{q_\mu} - \frac{\mu - \mu'}{\sigma}\right) \tag{8.17}$$

and if $\mu = \mu'$

$$F(q_\mu|\mu) = \Phi(\sqrt{q_\mu}) \tag{8.18}$$

The p-value is then found to be

$$p_\mu = 1 - \Phi(\sqrt{q_\mu}) \tag{8.19}$$

The upper limit (UL) on μ, i.e. the largest μ for which $p_\mu \leq \alpha$, where α is 0.05 to exclude values of μ at a confidence level of 95%, is calculated using equations (8.15) and (8.19):

$$\mu_{\mathrm{UL}} = \hat{\mu} + \sigma\Phi^{-1}(1 - \alpha) \tag{8.20}$$

Employing a so-called *Asimov data set* [62] the standard deviation σ can be estimated. The Asimov data set always returns the true values of parameters if it is used to evaluate the estimates for these.

To find an upper limit, it can be shown that

$$\sigma^2 = \frac{\mu^2}{q_{\mu,A}} \tag{8.21}$$

where $q_{\mu,A}$ is the test statistic using the Asimov data set [62].

The same procedure can be executed using the alternative test statistic $\tilde{q}_\mu$ instead of q_μ. The pdf does not follow a χ^2 distribution in this case [62]. The corresponding cumulative

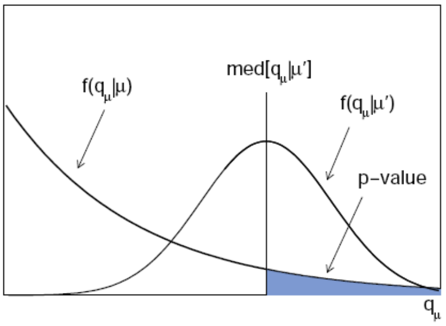

Figure 8.3: Relation between the p-value and the median of q_μ under assumption of a different strength parameter μ' [62].

distribution for $\tilde{q}_\mu$ is given by

$$F(\tilde{q}_\mu|\mu) = \begin{cases} \Phi\left(\sqrt{\tilde{q}_\mu}\right) & 0 < \tilde{q}_\mu \leq \mu^2/\sigma^2 \\ \Phi\left(\frac{\tilde{q}_\mu + \mu^2/\sigma^2}{2\mu/\sigma}\right) & \tilde{q}_\mu > \mu^2/\sigma^2 \end{cases} \tag{8.22}$$

The corresponding significance is given by

$$Z_\mu = \begin{cases} \sqrt{\tilde{q}_\mu} & 0 < \tilde{q}_\mu \leq \mu^2/\sigma^2 \\ \frac{\tilde{q}_\mu + \mu^2/\sigma^2}{2\mu/\sigma} & \tilde{q}_\mu > \mu^2/\sigma^2 \end{cases} \tag{8.23}$$

The upper limit on μ using $\tilde{q}_\mu$ and the corresponding error bands are given by

$$\mu_{UL+N} = \sigma(\Phi^{-1}(1-\alpha) + N) \tag{8.24}$$

The median exclusion significance assuming a strength parameter $\mu' = 0$, med$[Z_\mu|0]$ is given by

$$\text{med}[Z_\mu|0] = \sqrt{q_{\mu,\text{A}}} \tag{8.25}$$

For the alternative test statistic $\tilde{q}_\mu$, an analogous relation holds:

$$\text{med}[Z_\mu|0] = \sqrt{\tilde{q}_{\mu,\text{A}}}. \tag{8.26}$$

The relation between the p-value and the median of q_μ under assumption of a different strength parameter μ' is illustrated in Figure 8.3.

8.1.5 The CL_s procedure

If the pdfs assuming background only or signal and background are very similar and the distributions overlap mostly, the sensitivity of an experiment is very low. To avoid excluding values of the parameter of interest falsely (here μ) when the sensitivity is too low, the so-called CL_s method can be used [66]. If e.g. the result from an experiment agrees with the background-only hypothesis, even a signal strength of zero will be excluded 5% of the time for a confidence level of 95%. However, this result does not say much about the existence of a signal but more about the probability of finding at least an equally strong limit at future experiments.

Using the CL_s method, a hypothesis is excluded if $p_s \leq 1 - 0.95$, where 0.95 is the confidence level and p_s is defined as

$$p_s = \frac{p_{s+b}}{1 - p_b}. \tag{8.27}$$

and $CL_s = 1 - p_s$. Here, p_{s+b} is the 'usual' p-value and p_b is the p-value of the background-only hypothesis ($\mu = 0$). Thus the 'effective' p-value is reduced if the two distributions of background only and signal plus background are much alike. Using the Asimov data set, this p_s value can be written as [70]

$$p_s = \frac{1 - \Phi(\sqrt{q_\mu})}{\Phi(\sqrt{q_{\mu,A}} - \sqrt{q_\mu})}. \tag{8.28}$$

The median upper limit on μ using the CL_s method and the corresponding errors bands are given by [70]

$$\mu_{\mathrm{UL}+N} = \sigma(\Phi^{-1}(1 - \alpha\Phi(N) + N) \tag{8.29}$$

where $N = 0$ for the median limit and $N = 1, 2$ for the corresponding one- and two-sigma bands. The limits calculated in the following are based on the CL_s procedure.

8.2 Exclusion limit on the branching ratio $t \to H^+b$

Since no excess of data over the background estimates could be observed in Chapter 7, the m_T distribution from collision data and background estimates is used to derive a limit on the branching ratio $t \to H^+b$ for $m_{H^+} = 130\,\mathrm{GeV}$ assuming $H^+ \to \tau\nu = 1$.

The test statistics described above have been implemented into RooStats [68], a project to create statistical tools built on top of RooFit [69].

In the case at hand, it has to be taken into account that the $t\bar{t}$ background will be reduced with respect to the Standard Model background in the case of an H^+ signal. With the $t\bar{t}$ cross section staying the same as for Standard Model processes only, the branching ratio $t \to bW$ is reduced compared to the Standard Model only branching ratio if a light charged Higgs boson exists. This affects the background estimation from $e \to \tau$ and jet$\to \tau$ fake rates. The QCD background is not affected because it consists of only non-$t\bar{t}$ processes and the existence of a light charged Higgs boson has no effect on the abundance of QCD events. Background events with true τ leptons are not affected because here the background estimate is taken from collision data. If a light charged Higgs boson exists, the rate of Standard Model events used as input for the background estimation with true τ leptons will already be reduced accordingly.

The systematic uncertainties that are considered are summarized in Table 8.1. For the background with true τ leptons, the uncertainty on the τ energy scale is evaluated as described in chapter 7. The uncertainty on the τ identification is not evaluated for this background as no τ ID is used in the analysis but rather τ jets are identified using truth-matching and it is shown that the result does not depend on the τ identification efficiency. The systematic uncertainties given in Table 7.6 in chapter 7 are taken into account for the fake-rates and QCD background. For the signal, uncertainties as evaluated on $t\bar{t}$ samples are assumed [56]. An uncertainty of 11% is assumed on the integrated luminosity [55]. Limits are calculated for $m_{H^+} = 130\,\mathrm{GeV}$ and a branching ratio $\mathrm{BR}(H^+ \rightarrow \tau\nu) = 1$ is assumed.

The following Likelihood function is used [67]:

$$L(B,\alpha) = \prod_i Pois(n_i|\nu_i) \prod_j N(\alpha_j) \tag{8.30}$$

where B is the branching ratio $t \rightarrow H^+b$ and the parameter of interest, n_i the number of events in bin i of the transverse mass distribution, j numbers sources of systematic uncertainties while the α_j contain their effects. *Pois* is the poissonian pdf and N the normal distribution. ν_i gives the number of expected events in each bin:

$$\nu_i = 2B(1-B)A^{-1}n_i^s\sigma_{1i}(\alpha) + (1-B)^2 n_i^{t\bar{t}}\sigma_{2i}(\alpha) + n_i^b\sigma_{3i}(\alpha) \tag{8.31}$$

Here, A is a normalization factor needed to normalize the signal rate to the branching ratio, the different n_i are the expected numbers of events, n_i^s for signal, $n_i^{t\bar{t}}$ for $t\bar{t}$ background events and n_i^b for non-$t\bar{t}$ background events. The σ_{mi} and α include the systematic uncertainties from Table 8.1, with α being defined in a way that a ±1 standard deviation corresponds to $\alpha = \pm1$ for each individual systematic uncertainty. The σ_{mi} are defined as

$$\sigma_{mi}(\alpha) = \prod_j I(\alpha_j; \sigma^+_{mi\,j}\sigma^-_{mi\,j}) \tag{8.32}$$

with

$$I(\alpha; x^+x^-) = \begin{cases} 1+\alpha x^+ & \text{if} \alpha > 0 \\ 1 & \text{if} \alpha = 0 \\ 1-\alpha x^- & \text{if} \alpha < 0 \end{cases} \tag{8.33}$$

Here, the $\sigma^+_{mi\,j}$ and $\sigma^-_{mi\,j}$ describe the fractional effect of a systematic uncertainty j in bin i for the process m. Thus asymmetric uncertainties can be included in the calculation. The systematics itself are considered as uncorrelated, but each systematic is considered correlated between signal and background.

Observed limit The observed limit is calculated using Equation 8.28. The parameter of interest $\mathrm{BR}(t \rightarrow H^+b)$ is scanned from 0.0 to 0.5 in steps of 0.01. For each value of μ, the p-value according to equation 8.28 is calculated. The branching ratio and corresponding $1-p_s$-values are filled into a histogram. A fit is performed and the branching ratio corresponding to the confidence level of 0.95 is extracted, yielding the upper limit on the branching ratio $t \rightarrow H^+b$ that is compatible with data.

An observed upper limit on the branching ratio $\mathrm{BR}(t \rightarrow H^+b)$ for $m_{H^+} = 130\,\mathrm{GeV}$ assuming $\mathrm{BR}(H^+ \rightarrow \tau\nu) = 1$ of 0.17 results, corresponding to a cross section of about 47 pb.

	uncertainty on signal	uncertainty on background with true τ leptons
τ energy scale	$+0.0, -2.7$	$+0.0, -6.5$
τ identification	±7.4	-
jet energy scale	$+21, -18$	-
embedding	-	±15
embedding settings	-	±20
loose selection	-	$+15, -0.0$
luminosity	±11	±11

Table 8.1: Systematic uncertainties on the signal and background contribution with true τ leptons. Numbers are given in % [56].

+2σ	+1σ	median	-1σ	-2σ
0.44	0.33	0.24	0.17	0.13

Table 8.2: Expected CL_s limits on the branching ratio $t \to H^+b$ at a 95% confidence level assuming $m_{H^+} = 130\,\text{GeV}$, extracted from ATLAS data taken in 2010.

Expected limit The expected upper limit and its errors are calculated using equation 8.29.

The observed and expected upper limit on the branching ratio agree within 1σ. In Figure 8.4, the limits are illustrated depending on $\tan\beta$. Assuming a charged Higgs boson mass of 130 GeV, $\tan\beta$ values greater than 74 (96), where the solid black line crosses the observed (expected) limit line are excluded. The observed limit coincides with the -1σ value of the expected limit. Values for $\tan\beta$ corresponding to branching ratios for m_{H^+} have been calculated with FeynHiggs [72] in the m_h^{max} scenario. One should note that the region $\tan\beta > 65$ is theoretically not well controlled [71].

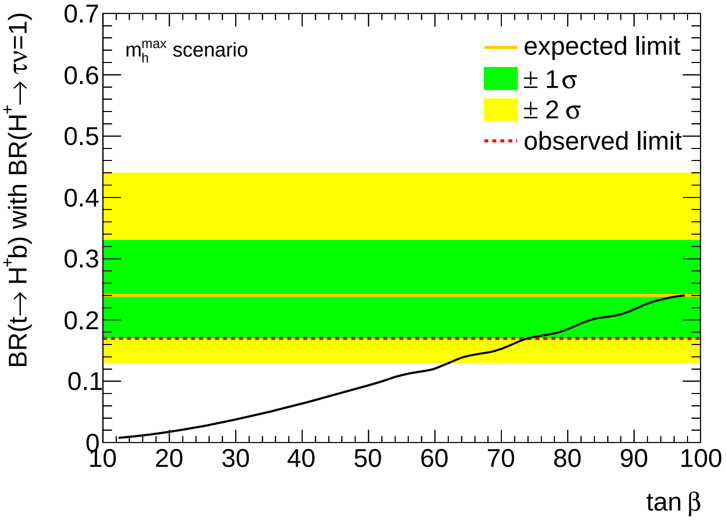

Figure 8.4: Illustration of expected and observed limits in a $BR(t \longrightarrow H^+b)$-$\tan\beta$-plane. Assuming a charged Higgs boson mass of 130 GeV, $\tan\beta$ values greater than those where the solid black line crosses the expected and observed limit line are excluded.

9 Conclusions

In this thesis, a search for a charged Higgs boson with m_{H^+} decaying to a τ and a neutrino has been performed with 35.5 pb^{-1} of data taken by ATLAS in 2010 at $\sqrt{s} = 7\,TeV$.

The discovery of charged Higgs bosons would be a definite sign for physics beyond the Standard Model. The LHC at CERN offers unique opportunities to search for these particles, with a promising topology for charged Higgs bosons, if $m_{H^+} < m_t$, being $t\bar{t} \to H^+bqqb$ and $H^+ \to \tau\nu$. But to search for New Physics, an accurate understanding of Standard Model background processes is indispensable.

The signal selection for light charged Higgs bosons in the channel $t\bar{t} \to WbH^+b \to qqb\tau\nu b$ has been optimized using the TMVA toolkit.

Furthermore, the Standard Model background to these charged Higgs boson searches has been estimated. The Standard Model background processes can be split up into four contributions: processes with true τ leptons, electrons faking τ leptons, jets faking τ leptons and QCD multi-jet processes.

Background processes containing true τ leptons decaying hadronically have been estimated using an embedding method. Events with a similar topology to that of signal events but a different final state that is expected to be almost signal free are collected from collision data. The unwanted final state particle is then removed and replaced by the corresponding particle from signal final states. Thus everything, including pile-up and underlying event, for background estimation but this one simulated particle is taken directly from collision data. The embedding selection, i.e. the sequence of cuts to select $t\bar{t} \to \mu + jets$ events applied to data before the embedding is run, has been optimized on simulation samples. Embedded Monte Carlo simulation have been compared to reference simulation. Also, embedded collision data have been compared to reference Monte Carlo simulation. Event yields and distributions after the embedding selection and embedding procedure applied to collision data and expectations from simulation agree well. Systematic uncertainties due to the embedding procedure and variations in the embedding selection that affect the embedding step have been studied.

The other background contributions have been estimated by other ATLAS members and have been quoted here for completeness.

Combining all background contributions and comparing them to collision data taken by ATLAS in 2010, no excess of collision data over the Standard Model expectations could be observed.

Using the results from the background estimations, upper limits on the branching ratio $t \to H^+b$ assuming $\mathrm{BR}(H^+ \to \tau\nu) = 1$ for $m_{H^+} = 130$ GeV could be set. At 95% confidence level, the observed limit is extracted to be 0.17 and the expected 0.24. Both limits agree within 1σ. These limits could be reinterpreted as limits on $\tan\beta$ for $m_{H^+} = 130$ GeV. For the observed (expected) limit a value of $\tan\beta = 74$ (96) results for the m_h^{max} scenario of the MSSM.

As this thesis is written, more than $2\,\mathrm{fb}^{-1}$ of data have been collected by the ATLAS detector. This allows to tighten the event selection and to study the embedding procedure in more detail. In case no hint for charged Higgs boson production will be found, large parts of the MSSM parameter space may be excluded for $m_{H^+} < m_t$.

Bibliography

[1] D. Griffiths, *Introduction to Elementary Particles*, 2^{nd} revised edition, Wiley-VCH

[2] F. Halzen & A.D. Martin, *Quarks and Leptons: An Introductory Course in Modern Particle Physics*, 1st edition 1984, John Wiley and Sons

[3] A. Djouadi, *The Anatomy of Electro-Weak Symmetry Breaking, Tome I: The Higgs boson in the Standard Model*, arXiv:hep-ph/0503172v2

[4] S. Glashow, Nucl. Phys. 22 (1961), S. Weinberg, Phys. Rev. Lett. 19 (1967), 1264
A. Salam, *Elementary Particle Theory*, ed. N. Svartholm, Almqvist and Wiksells, Stockholm (1969), 367

[5] D. Gross and F. Wilczek, Phys. Rev. Lett. 30 (1973) 1343
H. Politzer, Phys. Rev. Lett. 30 (1973) 1346

[6] P. W. Higgs , Phys. Rev. Lett. 13 (1964) 508
P. W. Higgs, Phys. Rev. 145 (1966), 1156
F. Englert and R. Brout, Phys. Rev. Lett. 13 (1964) 321
G. S. Guralnik, C. R. Hagen and T. W. B. Kibble, Phys. Rev. Lett. 13 (1964) 585
T. W. B. Kibble, PHys. Rev. 155 (1967) 1554

[7] ALEPH, CD, D0, DELPHI, L3, OPAL and SLD Collaborations, *Precision Electroweak Measurements and Constraints on the Standard Model*, CERN-PH-EP-2010-095

[8] ALEPH, DELPHI, L3 and OPAL Collaborations, *Search for the Standard Model Higgs Boson at LEP*, CERN-EP/2003-011

[9] CDF and D0 Collaborations, *Combined CDF and D0 Upper Limits on Standard Model Higgs Boson Production with up to 8.6 fb^{-1} of Data*, arXiv:1107.5518v1 [hep-ex]

[10] http://lepewwg.web.cern.ch/LEPEWWG/plots/summer2011/

[11] The ATLAS Collaboration, *Combined Standard Model Higgs Boson Searches in pp Collisions at $\sqrt{s} = 7\,TeV$ with the ATLAS Experiment at the LHC*, ATLAS-CONF-2011-112

[12] The CMS Collaboration, *Search for standard model Higgs boson in pp collisions at* $\sqrt{s} = 7$ *TeV*, CMS PAS HIG-11-011

[13] A. Djouadi, *The Anatomy of Electro-Weak Symmetry Breaking, Tome II: The Higgs bosons in the Minimal Supersymmetric Model*, arXiv:hep-ph/0503173v2

[14] see e.g.: P. Langacker, Phys. Rept 72C (1985)
R. Mohapatra, *Unification and Supersymmetry*, Ed. Springer 1986

[15] see e.g.: E. W. Kolb and M. S. Turner, *The Early Universe*, Addison-Wesley, New York, 1990

[16] S. Weinberg, Phys. Lett. 82B (1979) 387
M. Veltman, Acta. Phys. Polon. B12 (1981) 437
C. H. Llewellyn Smith and G. G. Ross, Phys. Lett. 105B (1981) 38

[17] Y. Gol'fand, E. Rikhtman, JETP Lett. 13 (1970) D. Volkov and V. Akulov, JETP Lett. 16 (1970) 438
J. Wess and B. Zumino, Nucl. Phys. B70 (1974) 39

[18] P. Fayet, Nucl. Phys. B90 (1975) 104,
P. Fayet, Phys. Lett. B64 (1976) 159,
P. Fayet, Phys. Lett. B69 (1977) 489,
P. Fayet, Phys. Lett. B84 (1979) 416
K. Inoue et al., Prog. Theor. Phys. 68 (1982) 927

[19] A. Pich, *The Standard Model of Electroweak Interactions* arXiv:hep-ph/9412274

[20] ALEPH, DELPHI, L3 and OPAL Collaborations, The LEP working group for Higgs boson seraches, *Searches for the Neutral Higgs bosons of the MSSM: Preliminary Combined Results Using LEP Data Collected at Energies up to 209 GeV*, LHWG Note 2001-2

[21] D0 Collaboration, *Search for charged Higgs bosons in top quark decays*, arXiv:0908.1811v2 [hep-ex]

[22] ALEPH, DELPHI, L3 and OPAL Collaborations, The LEP working group for Higgs boson seraches, *Search for Charged Higgs bosons: Preliminary Combined Results Using LEP data Collected at Energies up to 209 GeV* , LHWG note 2001-05

[23] M. Carena et al., *Suggestions for Improved Benchmark Scenarios for Higgs-Boson Searches at LEP2*, arXiv:hep-ph/9912223v1, December 1999
M. Carena et al., *Suggestions for Benchmark Scenarios for MSSM Higgs*

Boson Searches at Hadron Colliders, arXiv:hep-ph/0202167v1, February 2002

[24] The CMS Collaboration, *Search for the charged Higgs boson with* $H^+ \rightarrow \tau^+ \nu$ *decay mode in top quark decays*, CMS PAS HIG-11-008

[25] AC Team, *The four main LHC experiments*, June 1999, CERN-AC-9906026

[26] M. Ferro-Luzzio, CERN, *LHC 2010 Operation - As Viewed from the Experiments*, 2011

[27] J. Boyd (Ed.) et al., *Luminosity and Run Statistics Plots for 2010 Beam Data*, April 2011, https://twiki.cern.ch/twiki/bin/view/AtlasPublic/ RunStatsPublicResults2010, version r51, ATLAS twiki

[28] The ATLAS Collaboration, *The ATLAS Experiment at the CERN Large Hadron Collider*, 2008 JINST 3 S08003

[29] N. Andari et al., *Higgs Boson Production Cross Sections and Decay Branching Ratios*, ATL-PHYS-INT-2010-030

[30] T. Sjostrand et al., *PYTHIA 6.4 Physics and Manual*, JHEP 05 (2006) 026, arXiv:hep-ph/0603175

[31] E. Barberio et al., *PHOTOS: A universal Monte Carlo for QED radiative corrections in decays*, Comput. Phys. Commun. 66 (1991) 115-128

[32] Z. Was and P. Golonka, *TAUOLA as tau Monte Carlo for future applications*, nucl. Phys. Proc. Suppl. 144 (2005) 88-94, arXiv:hep-ph/0411377

[33] The ATLAS Collaboration, *Charged particle multiplicities in pp interactions at* $\sqrt{s} = 0.9$ *and 7 TeV in a diffractive limited phase-space measured with the ATLAS detector at the LHC and new PYTHIA6 tune*, ATLAS-CONF-2010-031

[34] U. Langenfeld et al., *New results for* $t\bar{t}$ *production at hadron colliders*, arXiv:0907.2527

[35] G. Corcella et al., *HERWIG 6: An Event generator for hadron emission reactions with interfering gluons (including supersymmetric processes)*, JHEP 0101 (2001) 010, arXiv:hep-ph/0011363

[36] J. Butterwort et al., *Multiparton interactions in photoproduction at HERA*, Z. Phys. C72 (1996) 637-646, arXiv:hep-ph/96701371

[37] The ATLAS Collaboration, *First tuning of HErWIG/JIMMY to ATLAS data*, ATL-PHYS-PUB-2010-014

[38] M. L. Mangano et al., *ALPGEN, a generator for hard multiparton processes in hadronic collisions*, JHEP 07 (2003) 001, arXiv:hep-ph/0206293

[39] J. Alwall et al., *Comparative study of various algorithms for the merging of parton showers and matrix elements in hadronic collisions*, Eur. Phys. J. C53 (2008) 473-500, arXiv:0706.2569

[40] The ATLAS Collaboration, *The ATLAS Simulation Infrastructure*, Eur. Phys. J. C70 (2010) 823-874, arXiv:1005:4568

[41] GEANT4 Collaboration, *GEANT4: A simulation toolkit*, Nucl. Instrum. Meth. A506 (2003) 250-303

[42] The ATLAS Collaboration, *Measurement of the top quark-pair production cross section with ATLAS in pp collisions at* $\sqrt{s} = 7\,TeV$, arXiv:1012.1792

[43] S. Frixiona, B. R. Webber, *Matching NLO QCD computations and parton shower simulations*, JHEP 06 (2002) 026, arXiv:hep-ph/0204244

[44] S. Frixione et al., *Single-top production in MC@NLO*, JHEP 03 (2006) 092, arXiv:hep-ph/0512250

[45] The ATLAS Collaboration, *Expected Performance of the ATLAS Experiment, Detector, Trigger and Physics*, CERN-OPEN-2008-020

[46] The ATLAS Collaboration, *Tau Reconstruction and Identification Performance in ATLAS*, ATLAS-CONF-2010-086

[47] E. Coniavitis, M.Flechl, *ATLAS Tau Identification in Early Data using a Robust Logarithmic Likelihood*, ATL-PHYS-INT-2010-123

[48] The ATLAS Collaboration, *Reconstruction, Energy Calibration and Identification of Hadronically Decaying Tau Leptons in the ATLAS Experiment*, ATLAS-CONF-2011-077

[49] M. Cacciary et al., *The anti-*k_T *clustering algorithm*, arXiv:0802.1189v2

[50] The ATLAS Collaboration, *Data-Quality Requirements and Event Cleaning for Jets and Missing Transverse Energy Reconstruction with the ATLAS Detector in Proton-Proton-Collisions at a Center-of-Mass Energy of* $\sqrt{s} = 7\,TeV$, ATLAS-CONF-2010-038

[51] L. Vacavant (Ed.) et al., *B Tagging for Early Data*, January 2011, https://twiki.cern.ch/twiki/bin/view/AtlasProtected/BTaggingForEarlyData, version r33, ATLAS twiki

[52] The ATLAS Collaboration, *Determination of the muon reconstruction efficiency in ATLAS at the Z resonance in proton-proton collisions at* $\sqrt{s} = 7\,TeV$, ATLAS-CONF-2011-008

[53] The ATLAS Collaboration, *Performance of the Missing Transverse Energy Reconstruction and Calibration in Proton-Proton Collisions at a Center-of-Mass Energy of $\sqrt{s} = 7$ TeV with the ATLAS Detector*, ATLAS-CONF-2010-057

[54] TMVA User's Guide, http://tmva.sourceforge.net

[55] The ATLAS Collaboration, *Data-driven estimation of the background to charged Higgs boson searches using hadronically-decaying τ final states in ATLAS*, ATLAS-CONF-2011-051

[56] S. Arghir et al., *Data-driven estimation of the background to ATLAS charged Higgs boson searches with hadronic-tau final states*, ATL-PHYS-INT-2011-028

[57] N. Möser et al., *Estimation of $Z \to \tau\tau$ Background in VBF $H \to \tau\tau$ Searches from $Z \to \mu\mu$ Data using an Embedding Technique*, ATL-PHYS-INT-2009-109

[58] C. Isaksson et al., *Embedding Technique for the ttbar Background Estimation in Charged Higgs Boson Searches*, ATL-PHYS-INT-2010-041

[59] Y. Rozen et al., *A Control Sample for $t\bar{t}$+jets Backgrounds with One or More τ Leptons in the Final State,*, ATL-PHYS-INT-2009-078

[60] N. Möser, private communication

[61] N. Möser (Ed.) et al., June 2011, *Embedding Tools*, https://twiki.cern.ch/twiki/bin/viewauth/Atlas/EmbeddingTools, version r46, ATLAS twiki

[62] G. Cowan et al., *Asymptotic formulae for likelihood-based tests of new physics*, arXiv:1007:1727v2

[63] K. Cranmer et al., *RooStats User's Guide*, Document version 0, 2010

[64] A. Wald, *Tests of Statistical Hypotheses Concerning Several Parameters When the Number of Observations is Large*, Transactions of the American Mathematical Society, Vol. 54, No. 3 (Nov. 1943)

[65] S. S. Wilks, *The large-sample distribution of the likelihood ratio for testing composite hypotheses*, The Annals of Mathematical Statistics, Vol. 9, No. 1 (March 1938)

[66] A. Read, *Modified Frequentist Analysis of Search Results (The CL_s Method)*, August 2000, CERN-OPEN-2000-205

[67] A. Martyniuk et al., *Searches for Light Charged Higgs Boson in $H^+ \to c\bar{s}$ with Early ATLAS Data*, ATL-COM-PHYS-2011-130

[68] https://twiki.cern.ch/twiki/bin/view/RooStats/WebHome

[69] http://roofit.sourceforge.net/

[70] ATLAS statistics forum, *Frequentist Limit Recommendation*, Draft 1.6, June 21, 2011

[71] A. Djouadi, Phys. Rep. 459 (2008) 1.

[72] http://feynhiggs.de

Danksagung

Es gab viele Menschen, die mich in den letzten Jahren unterstützt und mir insbesondere in den letzten Monaten zur Seite gestanden haben. Dass sie hier nicht erwähnt werden, liegt nicht daran, dass ich sie vergessen habe, sondern weil es hier konkret um die Leute gehen soll, die mir in der Uni und bei der Arbeit geholfen haben.

Ein großes Dankeschön geht an Markus ’the old one’. Vielen Dank für die Bereitstellung des Themas, die Aufnahme in die Gruppe und immer wieder konstruktive Vorschläge. Auch wenn es nicht immer so wirkte, waren sie doch meist hilfreich. Es war eine lehrreiche und interessante Zeit in deiner Gruppe; hoffen wir, dass das so weitergeht.

Ebenso vielen Dank an Martin. Ich habe in den letzten Monaten viel gelernt, auch wenn ich manchmal anfangs etwas überfordert war (und manchmal nach einer Weile immer noch...) oder vielleicht auch gerade deshalb. Du hast mich viel selber ausprobieren und irgendwann hinkriegen lassen, hast mir aber auch jederzeit geholfen, wenn ich Fragen und Probleme hatte.

Danke auch an die anderen Post-Docs und den Software-Doktoranden der Gruppe. Wann immer ich mit irgendwelchen Dingen ankam, hattet ihr ein offenes Ohr und habt geholfen.

Auch an meine Mit-Diplomanden vielen Dank. Ihr habt es mit mir im Büro ausgehalten oder für nette Unterhaltung beim Teetrinken gesorgt. Schade, dass das nicht so weiter geht.

Nun ist aber die Diplomarbeit geschafft und ich kann nur sagen:

> Make a break
> Just as soon as your able
> To run, hold on to your soul
> Before it takes you whole[1]

---

[1] aus: ’Logic of a Friend’ von Badly Drawn Boy

Erklärung

Hiermit erkläre ich, dass ich die vorliegende Diplomarbeit selbständig und nur unter Verwendung der angegebenen Quellen und Hilfsmittel verfasst sowie Ergebnisse und Zitate anderer kenntlich gemacht habe.

....
(Ort) (Datum) (Unterschrift)